Imaging core flow from geomagnetic secular variation: Consequences for core-mantle interactions and geomagnetic dipole moment changes

by

Hagay Amit

A dissertation submitted to The Johns Hopkins University in conformity with the requirements for the degree of Doctor of Philosophy.

Baltimore, Maryland

June, 2005

Abstract

Flow in the fluid outer core just below the core-mantle boundary is inferred from geomagnetic secular variation data, assuming frozen magnetic flux, tangential geostrophy, and a new physical assumption termed helical flow. Helical flow, in which tangential divergence correlates with radial vorticity, removes non-uniqueness in the inversion of the magnetic induction equation. My flow solutions using geomagnetic field models from the 2000 Oersted and 1980 Magsat satellites resemble previous flow models, but contain more flow along contours of radial magnetic field. I invert geomagnetic secular variation between 1895-1985 to isolate the time-average and time-dependent parts of the flow. The most prominent flow structure is a large anti-cyclonic vortex in the southern hemisphere. Time-average zonal flow outside the inner core tangent cylinder is generally westward in the southern hemisphere but nearly zero in the northern. Westward polar vortices occur inside the tangent cylinder. Mantle driving seems responsible for the mid-latitude asymmetry in the zonal core flow; core driving is responsible for the flow at high latitudes. Changes in the core's angular momentum calculated from my time-dependent core flow agree well with decade-scale length-of-day measurements. I fit the time-dependent flow to

a torsional oscillations model with periods 88 and 48 years. I test the quality of my core flow imaging method by inverting synthetic magnetic secular variation data from numerical dynamo models, and find that my method delineates most large-scale flow features. The correlation coefficient is large for a dynamo case with large-scale flow and magnetic field pattern, but degrades substantially in more complex cases. Including tangential magnetic diffusion improves flow recovery; however, unmodeled radial diffusion and data truncation effects cause severe artifacts. Finally, I combine geomagnetic secular variation data, time-dependent core flow, and dipole moment time-evolution equations to identify mechanisms of geomagnetic dipole moment change between 1895-1985. Meridional advection and radial magnetic diffusion are comparable and account for essentially all the observed moment decrease. Between 1895-1965, effects of tangential advection and radial diffusion on the equatorial moment cancel, allowing the geomagnetic tilt to remain nearly constant. Since 1970, the two mechanisms have both reduced the equatorial moment, causing the tilt decrease.

Advisor: Peter Olson

Reader: Thomas W. N. Haine

Acknowledgements

First and most of all I thank my advisor Professor Peter Olson. Peter spent endless hours guiding me through all aspects of scientific research, from physical concepts, through numerical methods, statistics, mathematical tools, to graphics and scientific writing. But above all, Peter has been incredibly inspirational to me in his enthusiasm and curiosity for acquiring knowledge and solving scientific problems. Learning from Peter has been extremely fruitful and very enjoyable.

I thank Professors Tom Haine and Darryn Waugh who taught most of my classes and participated in my committees. Tom and Darryn were always helpful whenever I asked. I am especially thankful to Tom for being a critical second reader of my thesis, and for convincing me to run a marathon.

I thank Professor Ulrich Christensen from the Max-Planck-Institut für Sonnensystem-forschung in Germany for generously inviting me to work with him. The collaboration with Uli was vital in the work on the inversion test chapter and more. Working with Uli was productive and insightful. I also thank Doctor Johannes Wicht for all his help and friendliness during my stay in Germany.

I thank Doctor Nitu Kitchloo for his help with the non-uniqueness problem.

I thank my group mates Steve Andreadis, Lijun Liu, and David Andrews for various collaborations and common travels. Studying with them has been very enjoyable.

I thank Eyal Shalev (previously Stanislavsky), my best friend in Baltimore. Eyal not only made the connection between Peter and I, but also convinced me to stop waitering in weddings and return to studying, and made the connection between my MA advisor in Israel Doctor Vladimir Liakhovsky and I.

I thank EPS people: staff, faculty, and students. Especially I thank those of you who joined me for backpacking, running, cycling, swimming, and other fun activities. You made me feel like at home in the department.

I thank my friends: Yoav Corcia and Inbal Dror, Ben and Michal Enosh, Eyal and Tamar Shalev, Dana Ashkenazi, Shay and Ravit Baytner, Yonni and Yeela Shaked, Josh and Sherry Rubin, Tamar Kohn, Rotem and Neta Segal, Zehava Khalfa, Justin and Amy Ries, Taber Hersum and Samantha Arnett, Lizet Christiansen, Sarah and Bill Penniston-Dorland, Sarah Carmichael, Shuliang Zhang, Jun Wu, Rodrigo Ferreira, Orly Tal, Ofra and Itai Klein Ben-David.

I thank my family: my father Michael, my mother Ora, my sister Sarit, and my brother Shay, for always believing in me (even though they know nothing about geomagnetism or the core).

Last but not least, I thank Beatriz Funatsu for being there for me and always supporting me, in better and worse days. I could not have done this without you.

Contents

List of Figures

List of Tables

Chapter 1

Geophysical background

1.1 The interior of the Earth

The internal structure of the Earth is known from seismology. Earthquakes generate compressional (*P*) and shear (*S*) waves which refract and reflect as they propagate through Earth's interior. Inversions of the observed seismic waves travel-times have been used to construct models of the interior of the Earth.

A good first approximation model for the interior of the Earth is radially-symmetric layers. The Earth is composed of three main regions: Solid mantle and crust, liquid outer core and solid inner core (Fig. 1.1a). The outer core is known to be liquid because shear waves do not propagate through that region. The core-mantle boundary is located 2891 km below the Earth's surface, and the inner-core boundary is located at a depth of 5150 km.

Fig. 1.1c shows the Earth's density profile according to the Preliminary Earth Model (PREM; Dziewonski and Anderson, 1981). The density discontinuities at 410 and 660 km depths are due to crystallographic changes. The density discontinuity across the core-mantle boundary is due to a change in composition there; the overlying mantle is mostly high-pressure silicate and oxide, whereas the outer core is mostly iron and iron alloys. The

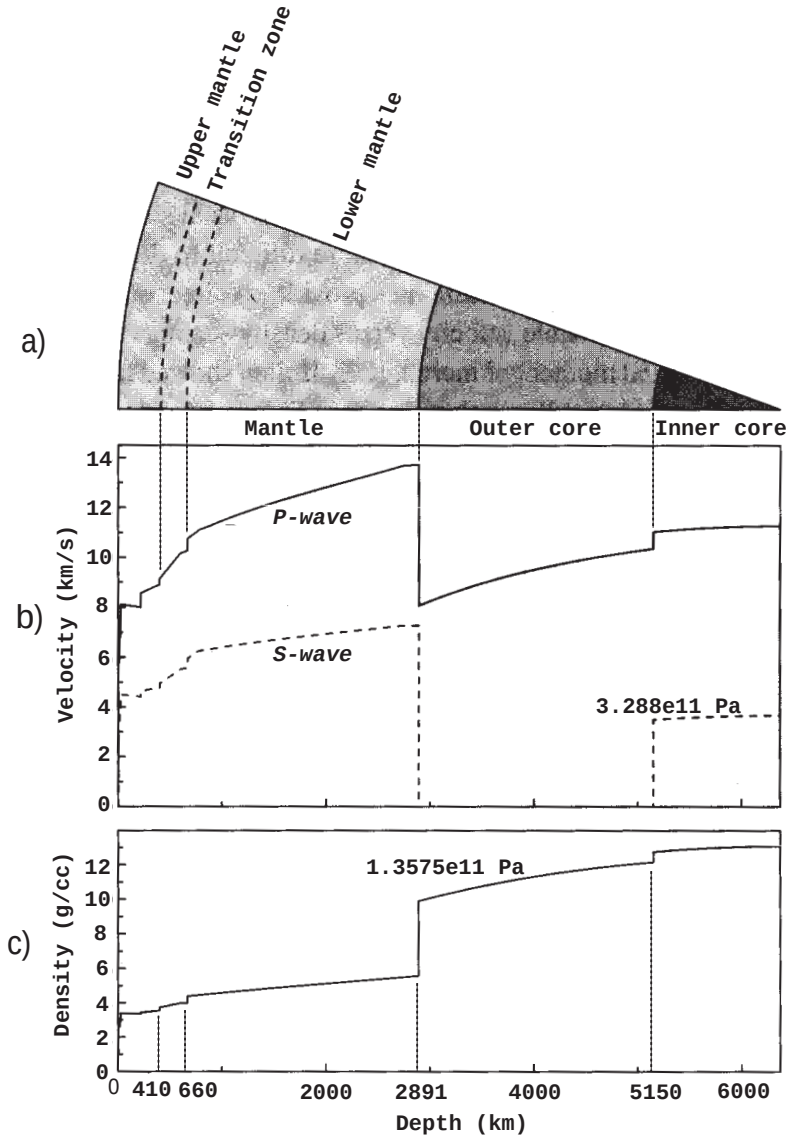

Figure 1.1: The radial structure of the Earth by main sections (a), seismic velocities (b), and density (c) based on PREM (Dziewonski and Anderson, 1981). In (b) the solid line is seismic *P-wave* velocity, and the dashed line is seismic *S-wave* velocity. The crust is evident by the immediate discontinuity below the surface in (b) and (c). Dotted lines denote discontinuities: The 410 km and 660 km mantle discontinuities define the transition zone between the above upper mantle and the lower mantle below; the core-mantle boundary separates the silicate-oxide solid mantle and the liquid metallic core; and the inner-core boundary separates the liquid outer core from the solid inner core. Pressure values at the core-mantle boundary and inner-core boundary are given in the figure (modified from Shearer, 2000).

density discontinuity across the inner-core boundary is due to a lower concentration of light elements in the inner core with respect to the outer core and the solid-liquid phase change. Melting temperature of iron at the core-mantle boundary pressure and freezing temperature of iron at the inner-core boundary pressure set constraints on core temperatures. Still, the temperatures at the core are not very well-known. Table 1.1 summarizes some of the main parameters of the core.

Region	r **(km)**	ρ **(kg/m^3)**	P **(Pa)**	g **(m/s^2)**	T **(k)**
above CMB	3480.0	5566.45	$1.3575e11$	10.68	3687 ± 113
below CMB	3480.0	9903.49	$1.3575e11$	10.68	3687 ± 113
above ICB	1221.5	12166.34	$3.288e11$	4.40	5638 ± 962
below ICB	1221.5	12763.6	$3.288e11$	4.40	5638 ± 962

Table 1.1: Density (ρ), pressure (P), and gravity (g) from PREM (Dziewonski and Anderson, 1981), and temperature (T) estimates including uncertainties (Poirier, 2000), for Earth's core. CMB is the core-mantle boundary, ICB is the inner-core boundary, and r is the distance from the center of the Earth.

1.2 Core properties

The composition of the core is known from the abundance of elements on Earth, which is inferred from chemical analysis of meteorites that were found on the surface of the Earth. The core is mostly composed of iron and about $4-5\%$ nickel (Poirier, 2000). However, the density of pure iron liquid at core pressure and temperature is about 10% higher than the density of the outer core. Therefore, lighter elements must be present in the core. Leading candidates for these elements include O, Si, S, H, C and K Merrill et al., 1998; Poirier, 2000). For example, Allegre et al. (1995) constructed a compositional model of the core with 7.3% Si, 2.3% S, and 4.0% O. The density of pure iron is about $3-6\%$ higher than the density of the inner core, suggesting that there are some light elements (though less) in the inner core as well. Light elements are differentiated from the inner core to the outer

core as the inner-core boundary freezes.

Estimates for the transport properties of the core are obtained from high-pressure mineral physics experiments and theory. Because the core is mostly metallic, its electrical conductivity is relatively high. The liquid core has a relatively low viscosity, i.e. the fluid flow at the outer core is very inviscid. The thermal diffusivity of the core is larger than the mantle's, but the Peclet number at the core is very large, i.e. convection is more dominant than conduction of heat. Estimates for the transport properties of the outer core are given in Table 1.2.

Parameter	**Symbol**	**Core value**
Kinematic viscosity	ν	$(0.6 - 1.5) \cdot 10^{-6}$
Thermal diffusivity	κ	$(0.4 - 0.5) \cdot 10^{-8}$
Magnetic diffusivity	λ	$0.8 - 4$

Table 1.2: Estimated range of values for the transport properties of the outer core in m^2/sec. The kinematic viscosity is inferred from the dynamic viscosity (Poirier, 2000) and the density at the top of the core (Dziewonski and Anderson, 1981); the thermal and magnetic diffusivities are taken from Poirier (2000).

1.3 Surface versus core geomagnetic field

The Earth's near surface can generally be approximated as an electromagnetic insulator, i.e. no electrical currents are present, and therefore the magnetic field $\vec{B}$ is a conservative vector field

$$\vec{B} = -\nabla V \ , \tag{1.1}$$

where V is some scalar potential. The geomagnetic field induced by internal sources can be represented by a sum of spherical harmonic coefficients (Merrill et al., 1998)

$$V = \frac{a}{\mu_0} \sum_{l=1}^{\infty} \sum_{m=0}^{l} (\frac{a}{r})^{l+1} P_l^m(\cos\theta)(g_l^m \cos m\phi + h_l^m \sin m\phi) \ , \tag{1.2}$$

where a is Earth's radius, μ_0 is free space permeability, (r, θ, ϕ) are spherical coordinates, $P_l^m(\cos\theta)$ are the associated Schmidt-normalized Legendre polynomials, and the Gauss coefficients are g_l^m and h_l^m. Equation (1.2) allows for downward continuation of a given geomagnetic field model at the Earth's surface ($r = a$) to the core-mantle boundary ($r = R$, where R is the core's radius).

Fig. 1.2 compares the radial component of the geomagnetic field on the Earth's surface and the field at the core-mantle boundary. The surface field is much smoother than the core field; the first is to a good approximation an inclined dipole with less than 20% non-dipole contributions, whereas the latter has significant non-dipole features. For example, areas with reversed magnetic polarity at the core-mantle boundary, appear with "normal" polarity and reduced strength at the Earth's surface.

1.4 Recent geomagnetic data - satellites

The 1980 Magsat and 2000 Ørsted magnetic satellite missions provided high-resolution global-coverage magnetic field data sets. These satellite missions were used to construct high-quality magnetic field models at the core-mantle boundary for 1980 and 2000. The geomagnetic secular variation inferred by the combination of these models was used to construct for the first time a small-scale satellite-data-derived core flow model (Hulot et al., 2002).

The 1980 US Magsat satellite was the first mission launched to map the geomagnetic field (Langel et al., 1980). The data was collected during two magnetically quiet days in 5-6 of November, 1979. The satellite was launched into a low-altitude, near-polar orbit. Initial orbital parameters were 651.2 km apogee, 352.4 km perigee, and 96.76° inclination. The magnetometers had accuracy of ± 1 nT. Magsat collected data with extensive global coverage; all except 16 of 648 $10^\circ \times 10^\circ$ blocks contained at least one data point. The

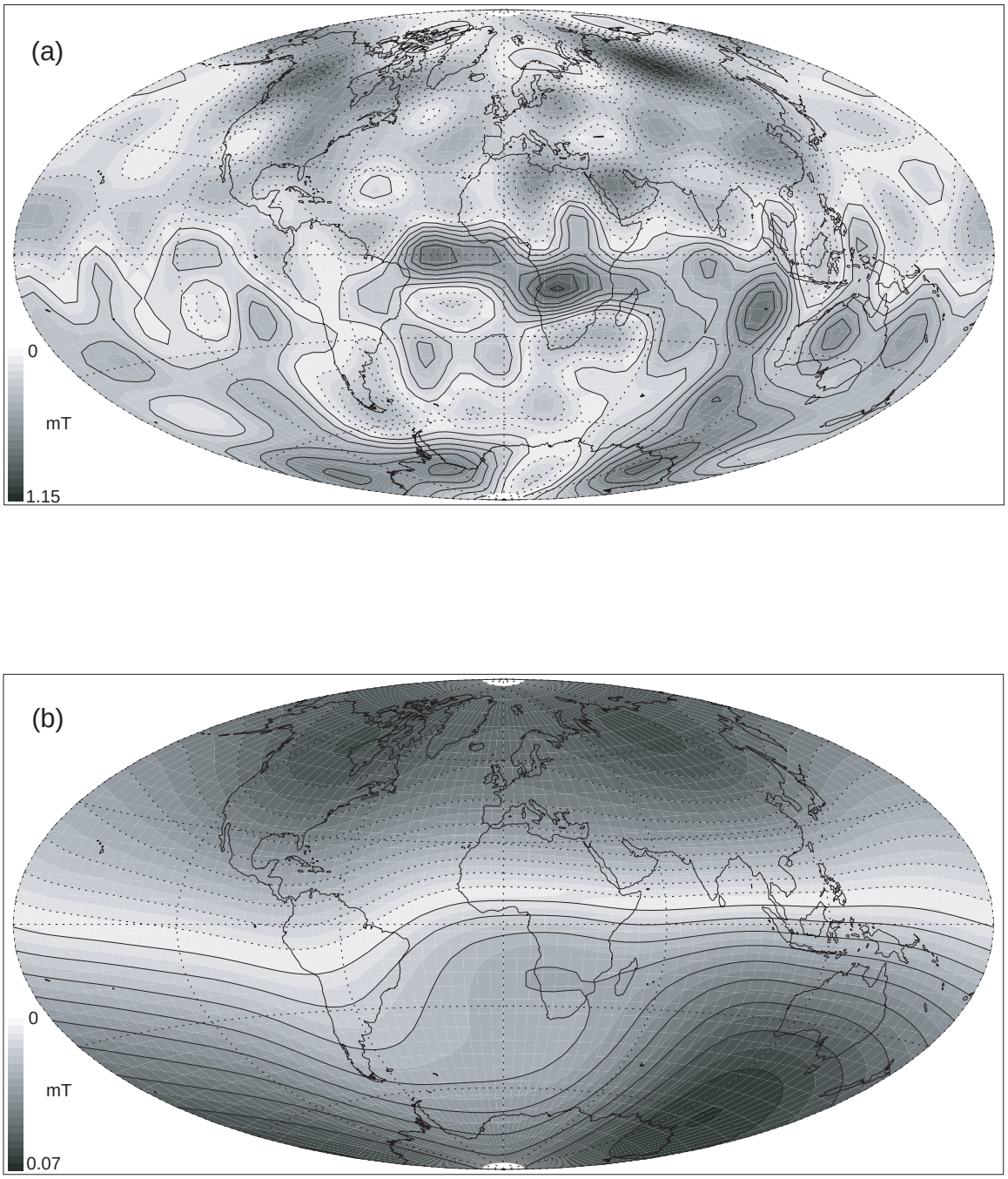

Figure 1.2: Radial component of the 2000 Ørsted magnetic field at the core-mantle boundary (a) and at the Earth's surface (b). Grey scale represents absolute values, solid lines are positive, dotted lines are negative. Note the difference in scales. Both fields are plotted out to spherical harmonic degree 14.

core magnetic field model has been truncated at spherical harmonic degree 13 to remove effects of crustal magnetization. Comparison of the Magsat geomagnetic field model with previous models obtained from surface observatories verified the ongoing decrease of the geomagnetic dipole moment at a rate of 26 nT/yr.

Twenty years later, the 2000 Danish Ørsted satellite provided the highest-quality geomagnetic data so far (Olsen et al., 2000). This data was obtained during quiet geomagnetic conditions around January 1, 2000. Ørsted was launched in a near polar orbit. Initial orbital parameters were 849 km apogee, 638 km perigee, and 96.5° inclination. The model used 2148 scalar data points and 3957 vector triplets. The internal source field is expanded to spherical harmonic degree 19, but only the expansion up to degree 14 is considered robust due to contamination by crustal magnetization at higher degrees. Largest residuals with respect to surface observations appeared in the southern polar cap due to summer ionospheric currents. The Ørsted model provided a firm basis for studies of the ionospheric, magnetospheric, lithospheric and core magnetic fields. According to this model, the strength of the geomagnetic dipole moment in 2000 is $7.79 \times 10^{22} Am^2$.

Fig. 1.3 shows the radial magnetic field (a) and secular variation (b) at the core-mantle boundary derived from the 1980 Magsat and 2000 Ørsted satellite models. These maps have much better resolution and global-coverage than previous maps obtained from surface observatories. The improvement in the resolution and reliability of these maps is especially pronounced at regions where less geomagnetic observatories are present, such as polar regions, southern hemisphere, and the oceans. Note that the typical length-scale in the radial magnetic field map is larger than the one in the secular variation map.

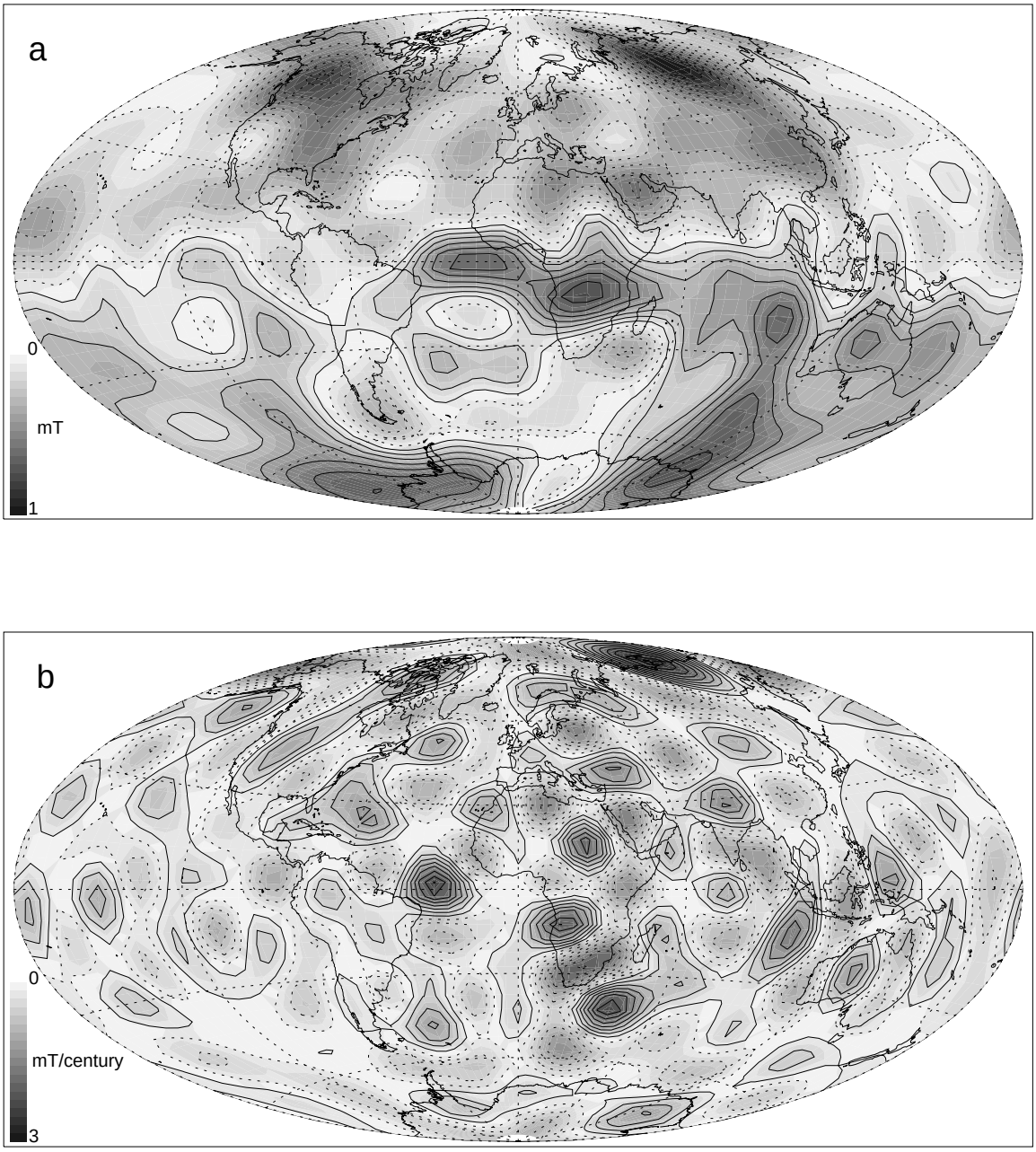

Figure 1.3: Radial magnetic field (a) and secular variation (b) in 1990 on the core-mantle boundary. Grey scale represents absolute values, solid lines are positive, dotted lines are negative. The 1990 magnetic field is the average of the 2000 Ørsted and 1980 Magsat field models, and the secular variation is their difference divided by 20 years. The geomagnetic field models were expanded until spherical harmonic degree 14.

1.5 Historical geomagnetic data - observatories

Prior to the satellite era, measurements of the Earth's magnetic field were collected by surface-based observatories. Since the advent of complete magnetic field vector measurements, including its intensity (by Gauss at about 1850), magnetic field observations from surface observatories worldwide have been combined to construct maps of the main geomagnetic field, which can be downward continued to the core-mantle boundary using (1.2). Increasing number of magnetic observatories with time have improved global-coverage and resolution of magnetic field models.

I use the time-dependent model of Bloxham and Jackson (1992) for the radial component of the magnetic field on the core-mantle boundary $B_r(\theta, \phi, t)$ truncated at spherical harmonic degree 14. The model extends from 1690 to 1990 with increasing uncertainty at older times; I concentrate on the time interval 1890-1990. This field model was constructed by fitting the magnetic observatory annual means and Magsat satellite data using spherical harmonics for spatial representation and cubic B-splines for the temporal representation.

1.6 Thesis statement

This thesis deals with the physical, numerical and technical problems in geomagnetic secular variation inversion, the geomagnetic imaging of fluid motion in the core. I use land-based plus satellite observations of geomagnetic secular variation and dynamo theory to construct models of fluid motion at the top of the core. I explore the geophysical implications of these core flow models in terms of magnetohydrodynamics at the outer core and core-mantle interactions. The issues addressed in this thesis include fluid dynamics at the top of the core, mantle control on core flow, core-mantle angular momentum exchange, and mechanisms of geomagnetic dipole moment changes.

The outline of the thesis is as follows. In chapter 2 I briefly review the governing

equations of dynamo theory and key concepts in numerical dynamos. In chapter 3 I introduce my method for imaging core flow from geomagnetic secular variation data (Amit and Olson, 2004). In chapter 4 I apply this method for the historical geomagnetic secular variation data, and I interpret the flow in terms of time-average and time-dependent parts; time-average core flow is modeled by thermal wind with mantle and core origins, whereas time-dependent core flow is interpreted in terms of angular momentum exchange between the core and the mantle (Amit and Olson, 2005). The inversion method is tested using synthetic data from self-consistent numerical dynamos in chapter 5. In chapter 6 I identify and quantify dynamo mechanisms for rapid geomagnetic dipole moment changes. I summarize my main findings in chapter 7, and I suggest directions for future work in chapter 8.

Chapter 2

Dynamo theory

2.1 Maxwell's equations of electromagnetism

The theory of electrodynamics is summarized by Maxwell's equations (e.g. Griffiths, 1999). Here I review these equations and the magnetohydrodynamic approximations, and briefly discuss their physical meaning. Maxwell's equations are combined to yield the magnetic induction equation.

Magnetic field is induced by electric currents and temporal changes in electric field according to the Ampere-Maxwell law

$$\nabla \times \vec{B} = \mu_0 \vec{J} + \mu_0 \epsilon_0 \frac{\partial \vec{E}}{\partial t} \ , \tag{2.1}$$

where $\vec{B}$ is magnetic field, $\mu_0 = 4\pi \cdot 10^{-7}$ N/A^2 is free-space permeability, $\vec{J}$ is electric current density, $\epsilon_0 = 8.85 \cdot 10^{-12}$ C^2/Nm^2 is free-space permittivity, $\vec{E}$ is electric field, and t is time. In the magnetohydrodynamic domain (as opposed to the plasma domain), the typical electric field frequency is much smaller than the mean collision frequency, i.e. the typical time-scale is larger the time for electromagnetic waves to cross a region, and the second term on the right hand side of (2.1) can be neglected (Hide and Roberts, 1961; Moffatt, 1978; Merrill et al., 1998; Davidson, 2001). Therefore, in core magnetohydrodynamics,

(2.1) is approximated by the pre-Maxwell Ampere's law

$$\nabla \times \vec{B} = \mu_0 \vec{J} \ . \tag{2.2}$$

The current density is related to the electromagnetic fields and the fluid velocity $\vec{u}$ by Ohm's law

$$\vec{J} = \sigma(\vec{E} + \vec{u} \times \vec{B}) \ , \tag{2.3}$$

where σ is electric conductivity. Electric field is induced by temporal changes in the magnetic field according to Faraday's law

$$\nabla \times \vec{E} = -\frac{\partial \vec{B}}{\partial t} \ . \tag{2.4}$$

Equations (2.2) - (2.4) contain four variable fields: $\vec{B}$, $\vec{E}$, $\vec{J}$, and $\vec{u}$. Elimination of $\vec{E}$ and $\vec{J}$ yields (Moffatt, 1978; Merrill et al., 1998; Roberts and Glatzmaier, 2000; Davidson, 2001; Kono and Roberts, 2002)

$$\frac{\partial \vec{B}}{\partial t} = \nabla \times (\vec{u} \times \vec{B}) + \lambda \nabla^2 \vec{B} \ , \tag{2.5}$$

where $\lambda \equiv 1/\mu_0 \sigma$ is the magnetic diffusivity.

Equation (2.5), the outcome of Maxwell's equations of electromagnetism with the magnetohydrodynamic assumption, is known as the **magnetic induction equation**. According to this equation, magnetic field is advected by the flow and diffused by Ohmic dissipation. The ratio of magnetic field advection to diffusion is estimated by the magnetic Reynolds number (Bondi and Gold, 1950)

$$Rm = \frac{|\nabla \times (\vec{v} \times \vec{B})|}{|\lambda \nabla^2 \vec{B}|} \sim \frac{UL}{\lambda} \ , \tag{2.6}$$

where U, L and λ are the typical velocity, length-scale and magnetic diffusivity, respectively. Hide and Roberts (1961) estimated based on the rate of the westward drift of the observed geomagnetic field that $R_m >> 1$ in the core. Large values of Rm indicate that magnetic field lines are *frozen* in the flow (Roberts and Scott, 1965).

2.2 Magnetohydrodynamics governing equations

Larmor (1919) was the first to suggest that the geomagnetic field is generated by dynamo action in Earth's liquid outer core. Since then dynamo theory has advanced significantly. Cowling (1934) proved that an axisymmetric magnetic field cannot be sustained by dynamo action. Elsasser (1946) estimated the geomagnetic field decay time and the magnitude of core flow based on theoretical considerations. Backus (1958) showed that there exist steady flows that maintain the magnetic field against Ohmic losses (the so-called kinematic dynamos), and he provided the conditions on such flows. In the early 1960s dynamo theory was well-established: Electric currents in the core induce magnetic field, and the interaction of fluid flow with the magnetic field produces electric currents (Hide and Roberts, 1961). Roberts (1972) found analytical and numerical kinematic dynamos with 2D periodicity. It is now generally accepted that rotating convection in the conducting outer core shell maintains the geomagnetic field against Ohmic losses (Moffatt, 1978; Merrill et al., 1998; Olson et al., 1999; Roberts and Glatzmaier, 2000; Davidson, 2001; Glatzmaier, 2002; Kono and Roberts, 2002).

Here I review the governing equations of dynamo theory. The magnetic induction equation derived in the previous section describes the evolution of magnetic field. Conservation of momentum, heat, and mass complete the set of governing equations for the evolution of the velocity field and temperature. I present the full dimensional set of magnetohydrodynamics equations and their assumptions. I introduce scales to obtain the corresponding non-dimensional equations and their control parameters.

Several key assumptions are commonly used to simplify the dynamo equations. First, the fluid is assumed incompressible, i.e. conservation of mass implies non-divergent flow. Second, the Boussinesq approximation is applied, i.e. density fluctuations from a mean state are neglected, except for the buoyancy term. The Boussinesq approximation intro-

duces an estimated inaccuracy of 20% to the output of numerical dynamos: Velocity, magnetic field and temperature (Roberts and Glatzmaier, 2000). Third, an equation of state is assumed to relate pressure, density and temperature. The incompressible Boussinesq magnetic (i.e. with Lorentz force) conservation of momentum (Navier-Stokes) equation in a rotating frame (i.e. with Coriolis force) is (Hide and Roberts, 1961; Braginsky, 1997; Merrill et al., 1998; Kono and Roberts, 2002)

$$\rho(\frac{\partial \vec{u}}{\partial t} + \vec{u} \cdot \nabla \vec{u} - \nu \nabla^2 \vec{u}) + 2\rho\vec{\Omega} \times \vec{u} + \nabla P' = -\alpha \vec{g} T' + \vec{J} \times \vec{B} \ , \tag{2.7}$$

where ρ is mean density, t is time, ν is kinematic viscosity, Ω is the rotation vector (pointing in the direction of the rotation axis), P' is pressure perturbation from its mean, α is thermal expansivity, $\vec{g}$ is gravitational acceleration vector (pointing radially outwards), and T' is temperature perturbation from its mean. The terms in (2.7) from second on left to right represent forces acting on the fluid: Inertial, viscous, Coriolis (due to the rotation of the Earth), pressure gradient, buoyancy, and magnetic Lorentz forces. In the core, two sources of buoyancy exist - thermal and compositional. The fluid is thermally-buoyant because the temperature increases with depth, and chemically-buoyant because light elements are being released at the inner-core boundary as it freezes (Braginsky, 1997). Loper (1978) argued that a gravitationally-powered dynamo, i.e. dominated by compositional convection, is more likely than a thermally-powered dynamo. Only thermal buoyancy is considered in (2.7); nevertheless the main effect of buoyancy is captured. The conservation of heat equation is

$$\frac{\partial T}{\partial t} + \vec{u} \cdot \nabla T = \kappa \nabla^2 T \ , \tag{2.8}$$

where κ is thermal diffusivity. According to (2.8), temporal changes in temperature are due to advection of heat by the flow and thermal diffusion. Note that no heat sources (e.g. radioactive) are included in (2.8). The conservation of mass (continuity) equation for an

incompressible fluid is

$$\nabla \cdot \vec{u} = 0 \ , \tag{2.9}$$

and the magnetic field is non-divergent

$$\nabla \cdot \vec{B} = 0 \ . \tag{2.10}$$

Equations (2.5) and (2.7) - (2.10) form the complete set of dimensional magnetohydrodynamics equations. These equations are scaled (Table 2.1) to obtain the non-dimensional governing equations (Olson et al., 1999)

Variable	**Symbol**	**Scaling**
Length	D	$R - R_i$
Time	t	D^2/ν
Temperature	T	ΔT
Pressure	P	$\rho\nu\Omega$
Velocity	U	ν^2/D
Magnetic field	B	$(\rho\lambda\mu_0\Omega)^{1/2}$
Current density	J	$(\rho\lambda\Omega/\mu_0 D^2)^{1/2}$

Table 2.1: Scaling laws for the dynamo equations (from Olson et al., 1999). Ω is Earth's rotation rate, R is core's radius and R_i is inner core radius.

$$Ek(\frac{\partial \vec{u}}{\partial t} + \vec{u} \cdot \nabla \vec{u} - \nabla^2 \vec{u}) + 2\hat{z} \times \vec{u} + \nabla P = Ra\frac{\vec{r}}{R}T + \frac{1}{Pm}(\nabla \times \vec{B}) \times \vec{B} \tag{2.11}$$

$$\frac{\partial \vec{B}}{\partial t} = \nabla \times (\vec{u} \times \vec{B}) + \frac{1}{Pm}\nabla^2 \vec{B} \tag{2.12}$$

$$\frac{\partial T}{\partial t} + \vec{u} \cdot \nabla T = \frac{1}{Pr}\nabla^2 T \tag{2.13}$$

$$\nabla \cdot \vec{u} = 0 \tag{2.14}$$

$$\nabla \cdot \vec{B} = 0 \ , \tag{2.15}$$

where $\hat{z}$ is a unit vector in the direction of the rotation axis and $\vec{r}$ is the position vector. Four non-dimensional parameters in (5.1) - (5.5) control the dynamo action. The (modified)

Rayleigh number represents the strength of convection

$$Ra = \frac{\alpha g_0 \Delta T D}{\nu \Omega} \ , \tag{2.16}$$

where g_0 is the gravitational acceleration on the core-mantle boundary, and ΔT is the temperature difference across the outer core. The Ekman number is the ratio of viscous to Coriolis forces

$$Ek = \frac{\nu}{\Omega D^2} \ , \tag{2.17}$$

the Prandtl number is the ratio of kinematic viscosity to thermal diffusivity

$$Pr = \frac{\nu}{\kappa} \ , \tag{2.18}$$

and the magnetic Prandtl number is the ratio of kinematic viscosity to magnetic diffusivity

$$Pm = \frac{\nu}{\lambda} \ . \tag{2.19}$$

2.3 Numerical dynamos

Glatzmaier and Roberts (1995) were the first to report a successful 3D numerical dynamo. Numerical dynamos model magnetic field generation by convection in a 3D rotating spherical shell (Olson et al., 1999; Roberts and Glatzmaier, 2000; Glatzmaier, 2002; Kono and Roberts, 2002). These models solve (5.1) - (5.5) for the magnetic field, velocity and temperature. How well do numerical dynamos simulate the geodynamo? To address this question, I compare the values of the control parameters as well as some output parameters from the numerical dynamos with the ones estimated for Earth's core.

Table 2.2 compares values of non-dimensional numbers from numerical dynamos with Earth-like values. The models' input parameters are the Rayleigh, Ekman, Prandtl, and magnetic Prandtl numbers. The output parameters are the magnetic Reynolds number (2.6),

Number	Symbol	Numerical dynamos	Core
Rayleigh	Ra	$(0.07 - 1.5) \times 10^7$	10^{30}
Ekman	Ek	$(6.3 - 63) \times 10^{-5}$	10^{-15}
Prandtl	Pr	1	0.2
Magnetic Prandtl	Pm	$1 - 5$	5×10^{-6}
Magnetic Reynolds	Rm	$11.6 - 281$	$O(10^2)$
Elsasser	Λ	$0.14 - 14$	≥ 1

Table 2.2: Comparison of parameters in numerical dynamos and estimated core values. Numerical dynamos values are from Christensen et al. (1998, 1999, 2001), Olson et al. (1999), and Kutzner and Christensen (2000); core values are from Kono and Roberts (2002), except for Elsasser number from Merrill et al. (1998).

and the Elsasser number, which is the ratio of Lorentz to Coriolis forces

$$\Lambda = \frac{\sigma B^2}{\rho \Omega} \ , \tag{2.20}$$

where B is typical magnetic field and ρ is density.

From Table 2.2 it is clear that numerical dynamos do not operate at core-like values. Core-like values have too small diffusivities (see Table 2.2). Therefore, technical computational limitations unable numerical dynamos to reach core-like parameter regime (Glatzmaier, 2002). More specifically, convection is too weak (small Ra number) and viscous effects are too strong (large Ek number) in numerical dynamos. However, the models' output seems to provide the correct order of magnitude for the Elsasser number and magnetic Reynolds number. This result is encouraging, because it means that despite using inadequate input parameters, numerical dynamos reproduce advective-dominant magnetic field evolution and the appropriate balance of Lorentz and Coriolis forces as expected in the core.

Chapter 3

Helical core flow from geomagnetic secular variation

3.1 Introduction

Mapping the flow in Earth's liquid outer core places constraints on the geodynamo, the thermal structure of the core, and the nature of core-mantle coupling. Geomagnetic data provided by the Danish Ørsted satellite in 2000, combined with the data from the US Magsat satellite in 1980, give a global model of the Earth's magnetic field and its secular variation on the core-mantle boundary up to spherical harmonic degree 14 for imaging of the fluid flow below the core-mantle boundary. Here I present a method that combines helical flow and tangential geostrophy to obtain the fluid motion below the core-mantle boundary consistent with the secular variation. We compare results from different types of physical assumptions, such as tangential geostrophy, strong helicity, weak helicity and columnar flow.

My solution method is novel in several respects. First, I formulate a general expression for the tangential divergence term that incorporates inertial effects such as tangen-

tial geostrophy with effects due to viscous and buoyancy forces that produce helical flow. Second, my method uses a grid-based finite difference representation, as opposed to the conventional spectral methods in which the flow potentials are represented in spherical harmonics.

Non-uniqueness is a major problem in the inversion of fluid flow at the top of the core from geomagnetic secular variation data. Backus (1968) showed that, without specifying the tangential divergence, the flow is non-unique. Backus and LeMouël (1986) showed that the tangential geostrophy assumption reduces the non-uniqueness, but does not eliminate it. My helical flow assumption removes this non-uniqueness.

The outline of the chapter is as follows. In section 2 I review the general theory and previous frozen flux inversions of geomagnetic secular variation. In section 3 I describe the theoretical background for my method, including my physical assumptions. In section 4 I describe my numerical technique and present results of a test case to verify its reliability. In section 5 I present my results, including a sensitivity test, a resolution test and comparison between results from different physical assumptions. My main findings are summarized in section 6.

3.2 Frozen flux theory

3.2.1 The radial magnetic induction equation at the top of the core

Properties of the flow in the liquid outer core are inferred from geomagnetic secular variation, assuming the magnetic field acts like a tracer. The radial component of the magnetic induction equation (2.5), assuming that the radial velocity vanishes just below the core-mantle boundary, is

$$\frac{\partial B_r}{\partial t} + \vec{u}_h \cdot \nabla B_r + B_r \nabla_h \cdot \vec{u}_h = \lambda(\frac{1}{r^2}\frac{\partial^2}{\partial r^2}(r^2 B_r) + \nabla_h^2 B_r) \tag{3.1}$$

where B_r is the radial component of the magnetic field, t is time, $\vec{u}_h$ is the fluid velocity tangent to the core-mantle boundary, λ is the magnetic diffusivity and $\nabla_h^2 = \nabla^2 - \frac{1}{r^2}\frac{\partial}{\partial r}(r^2\frac{\partial}{\partial r})$. Throughout the chapter, the subscript h refers to tangential (θ, ϕ) coordinates. To infer core flow using (5.10), the "tracer" B_r and its time derivative $\partial B_r/\partial t$ are assumed known, and the fluid velocity $\vec{u}_h$ is unknown.

Previous studies generally assumed frozen flux, in which the diffusion of magnetic field is neglected in comparison with the advection of magnetic field by the flow. The frozen flux hypothesis is assumed valid because the magnetic diffusion time scale, $\tau_\lambda = L^2/\lambda$, is much longer than the advection time, $\tau_v = L/U$, where L, U and λ are the typical length scale, velocity and magnetic diffusivity for the Earth's core. The ratio of these time scales in (5.10) yields

$$\frac{\tau_\lambda}{\tau_v} = \frac{|\vec{u}_h \cdot \nabla B_r|}{|\lambda \nabla_h^2 B_r|} \sim \frac{UL}{\lambda} = R_m \tag{3.2}$$

where R_m is the magnetic Reynolds number. Using $L = 10^6$ m, $U = 5 \times 10^{-4}$ m/s and $\lambda = 1$ m^2/s gives $\tau_\lambda \sim 30,000$ yr and $\tau_v \sim 60$ yr, i.e. $R_m \sim 500$, large enough so that the effects of magnetic diffusion can be neglected to a first approximation (e.g. Bloxham, 1989).

According to the Helmholtz representation, the tangential velocity can be written as the sum of a tangentially non-divergent toroidal velocity and a tangentially divergent poloidal velocity,

$$\vec{u}_h = \vec{u}_{tor} + \vec{u}_{pol} \tag{3.3}$$

In a spherical coordinate system (r, θ, ϕ), the toroidal velocity can be expressed by a streamfunction Ψ and the tangential poloidal velocity can be expressed by a scalar potential Φ in the following way:

$$\vec{u}_{tor} = \nabla \times \Psi \hat{r} \tag{3.4}$$

$$\vec{u}_{pol} = \nabla_h \Phi \tag{3.5}$$

where $\hat{r}$ is a unit radial vector. In terms of their components, the toroidal and poloidal tangential velocities are

$$(u_\theta, u_\phi)_{tor} = (\frac{1}{r sin\theta}\frac{\partial \Psi}{\partial \phi}, -\frac{1}{r}\frac{\partial \Psi}{\partial \theta}) \tag{3.6}$$

$$(u_\theta, u_\phi)_{pol} = (\frac{1}{r}\frac{\partial \Phi}{\partial \theta}, \frac{1}{r sin\theta}\frac{\partial \Phi}{\partial \phi}) \tag{3.7}$$

Using these expressions for the velocities, the radial vorticity in the fluid ζ is given in terms of the streamfunction Ψ as

$$\zeta = \hat{r} \cdot \nabla \times \vec{u}_h = \nabla_h^2 \Psi \tag{3.8}$$

and the surface divergence of the fluid velocity $\nabla_h \cdot \vec{u}_h$ is given in terms of the scalar potential Φ as

$$\nabla_h \cdot \vec{u}_h = \nabla_h^2 \Phi \tag{3.9}$$

Substitution of (3.6) - (3.7) and (3.9) into (5.10) and neglecting magnetic diffusion gives the radial component of the frozen flux magnetic induction equation in terms of the two potentials Ψ and Φ. On the core-mantle boundary ($r = R$, the radius of the core), (5.10) becomes

$$\frac{\partial B_r}{\partial t} + \frac{1}{R^2 sin\theta}(\frac{\partial \Psi}{\partial \phi}\frac{\partial B_r}{\partial \theta} - \frac{\partial \Psi}{\partial \theta}\frac{\partial B_r}{\partial \phi}) + \frac{1}{R^2}(\frac{\partial \Phi}{\partial \theta}\frac{\partial B_r}{\partial \theta} + \frac{1}{sin^2\theta}\frac{\partial \Phi}{\partial \phi}\frac{\partial B_r}{\partial \phi}) + B_r \nabla_h^2 \Phi = 0 \tag{3.10}$$

The physical interpretation of the terms in (5.12) are as follows. The first term is the secular variation of the magnetic field. The second and third terms are advection of B_r by toroidal and poloidal velocities, respectively. The fourth term represents the effect of upwelling motions from the interior of the outer core on B_r.

The core-mantle boundary is usually modeled as a rigid impermeable boundary, in which case the velocity there is identically zero. However, since B_r is continuous there, and the Ekman boundary layer thickness is much smaller than the magnetic boundary layer, it is assumed that B_r and $\partial B_r/\partial t$ vary little through the Ekman boundary layer, and (5.12)

applies to the flow of the free stream at the top of the core just below the core-mantle boundary (Bloxham and Jackson, 1991).

3.2.2 Previous studies

Different core flows were obtained in the past due to different regularization methods, physical assumptions, and data (see Bloxham and Jackson, 1991 for a review of these). Previously-used spectral methods minimized simultaneously the data residual and a quadratic function of the parameter vector using a trade-off damping coefficient. Some previous studies have minimized the kinetic energy to regularize their solutions (Whaler, 1986; Gubbins, 1982). Others minimized the norm of the second derivatives of the flow (Bloxham, 1989), or the deviation from a decreasing velocity spectra (Gire and LeMouël, 1990). Pais and Hulot (2000) used a regularized method with one covariance matrix for the data uncertainty and another for the a-priori kinetic energy. They found a small range of damping coefficients which lead to a misfit in the data residual in agreement with the data uncertainty, and complies with the energetic requirement.

Previous authors truncated their flow solutions at some spherical harmonic degree. Gire et al. (1986) derived a low spherical harmonic degree spectrum of motion. Whaler (1986) pointed out that the disadvantage of previous methods is strong dependency on the velocity truncation level. Rau et al. (2000) tested their inversion method with synthetic data from dynamo simulations. For their low-pass filter case, they resolved the flow up to spherical harmonic degree 5. They concluded that limited resolution due to crustal magnetization, uncertainties in the physical assumptions, and uncertainties in the methodical constraints lead to poorly constrained flows.

Different methods and physical assumptions have been used to reduce the non-uniqueness. Gubbins (1982) assumed a combination of steady flow without upwelling. He argued that the non-uniqueness is reduced if two separate inversions yield two sufficiently different di-

rections of velocity. Voorhies (1986) used the steady flow assumption and pointed out that the non-uniqueness is reduced if B_r at three different epochs is known. Rau et al. (2000) argued that the steady flow assumption yields poor fits even in decadal timescales. Another common way to reduce the non-uniqueness is by specifying the tangential divergence term in (5.10). The simplest upwelling assumption is, of course, pure toroidal flow: $\nabla_h \cdot \vec{u}_h = 0$. Without upwelling the non-unique flow component is along B_r-contours. Whaler (1980) interpreted relatively small secular variation values at local extrema of B_r as statistical evidence for pure toroidal flow. Other authors have also concluded that the flow at the top of the core is purely toroidal. Gubbins (1982) interpreted the apparent upwellings in core flow models as data uncertainties, while Bloxham (1989) interpreted them as contamination by radial magnetic diffusion. LeMouël (1984) assumed tangential geostrophy from the balance between Coriolis and pressure gradient forces below the core-mantle boundary: $\nabla_h \cdot (\vec{u}_h cos\theta) = 0$. For this assumption the non-unique flow component is along $B_r / \cos\theta$-contours that do not cross the equator. These ambiguous patches compose 40% of the core-mantle boundary at 1980 (Bloxham and Jackson, 1991; Chulliat and Hulot, 2000). Rau et al. (2000) concluded that the flow is mostly toroidal and geostrophic. Recent studies by Pais and Hulot (2000) and Hulot et al. (2002) preferred the tangential geostrophy assumption.

Some of the main inferences about core flow from previous studies are as follows. Voorhies (1986) found in pure toroidal flow solutions evidence for Taylor columns in asymmetric vortices with respect to the equator. Some studies found that pure toroidal flows had better fits than geostrophic flows (Bloxham, 1989; Bloxham and Jackson, 1991). Bloxham (1989) observed persistent trans-equatorial flow below Indonesia, in contradiction to the geostrophic assumption. Whaler (1986) stated that any solution without upwelling yields a statistically inadequate fit. She remarked that upwelling indicates local convection strength. A poloidal-toroidal flow solution contains twice as many free parameters as a toroidal flow,

and thus allows smaller data residuals. Authors that preferred poloidal-toroidal flow over pure toroidal flow argued that the first is less energetic (Gire et al., 1986), or its data residuals are significantly smaller (Voorhies, 1986). However, the poloidal flow component is less well determined (Whaler, 1986; Voorhies, 1986). Gire and LeMouël (1990) found an equatorially-aligned flow compatible with their geostrophic assumption. Rau et al. (2000) found both toroidal and geostrophic assumptions reasonable, with a preference for the latter. Gire and LeMouël (1990) concluded that the secular variation reflects the temporal behavior of the poloidal flow, and the toroidal flow is responsible for exchanging angular momentum between the core and the mantle. Jault et al. (1988) and Jackson et al. (1993) found good correlation between changes in the angular momentum of the core (inferred from core flow inversions) to those inferred from variations in the length of the day. Zatman and Bloxham (1997) interpreted time-dependent zonal flows as torsional oscillations. Rau et al. (2000) stressed that the limitation on the data resolution due to crustal magnetization might cause flow patterns with artifacts. They found that large scale zonal flow and mid-latitude gyres are the most reliable flow structures, and that they may represent an image of columnar convection outside the tangent cylinder, which is the imaginary cylinder parallel to the spin axis and circumscribing the equator of the inner core (Aurnou et al., 2003). Hulot et al. (2002) used the 2000 Ørsted and 1980 Magsat satellite geomagnetic data sets and found higher velocities in the Atlantic hemisphere than in the Pacific one. They commented that the large secular variations at high latitudes (especially in the northern hemisphere) and below Africa could not be predicted before the Ørsted data. Their non-axisymmetric flow displays vortices around the tangent cylinder.

Different authors' core flows contain different zonal flows. Gire et al. (1984) found that a $0.2\ ^\circ$/yr westward drift is the dominant flow motion. Bloxham (1989) found a westward drift less than $0.1\ ^\circ$/yr. The solution of Voorhies (1986) contains a bulk westward drift with superimposed jets and gyres. Pais and Hulot (2000) found large zonal angular velocities at

high latitudes (though not reliable) and an equatorially-antisymmetric zonal flow outside the tangent cylinder. Hulot et al. (2002) found a westward equatorially-symmetric flow of $\sim 0.1\ ^\circ$/yr outside the tangent cylinder, and westward polar vortices of $\sim 0.9\ ^\circ$/yr. A similar polar vortex was found by Olson and Aurnou (1999).

3.3 Physical assumptions for coupling toroidal and poloidal motions

Equation (5.12) contains two scalar variables, the potentials Ψ and Φ. In order to invert this equation for the tangential velocity at the top of the free stream below the core-mantle boundary given B_r and $\partial B_r/\partial t$, I make one additional assumption to relate the two potentials. I will show that this assumption removes the non-uniqueness from the inversion problem.

3.3.1 Pure toroidal flow

A trivial way to couple toroidal and poloidal flows is to assume that the flow is purely toroidal, so that

$$\nabla_h \cdot \vec{u}_h = 0 \tag{3.11}$$

According to this assumption, the surface flow is non-divergent and can be expressed in terms of the streamfunction only, i.e. all terms with Φ in (5.12) vanish.

3.3.2 Tangential geostrophy

Another standard way to couple toroidal and poloidal flows is to assume a geostrophic balance for the tangential components of the fluid momentum below the core-mantle boundary, i.e. Coriolis and pressure gradient forces dominate the flow (LeMouël, 1984). This is

the tangential geostrophy assumption, and leads to the following constraint:

$$\nabla_h \cdot (\vec{u}_h cos\theta) = 0 \tag{3.12}$$

which can be rewritten as

$$cos\theta \nabla_h \cdot \vec{u}_h + \vec{u}_h \cdot \nabla cos\theta = 0 \tag{3.13}$$

The expression for the radial upwelling becomes, according to the tangential geostrophy assumption

$$\nabla_h \cdot \vec{u}_h = \frac{\tan\theta}{R} u_\theta \tag{3.14}$$

which can be expressed in terms of the two potentials Ψ and Φ using (3.6) - (3.7) and (3.9) as

$$\nabla_h^2 \Phi = \frac{tan\theta}{R^2}(\frac{1}{sin\theta}\frac{\partial \Psi}{\partial \phi} + \frac{\partial \Phi}{\partial \theta}) \tag{3.15}$$

3.3.3 Helical flow

Here I introduce a third way to couple toroidal and poloidal motions, by assuming a correlation between tangential divergence and radial vorticity at the top of the free stream below the core-mantle boundary. I assume

$$\nabla_h \cdot \vec{u}_h = \mp k_0 \zeta \tag{3.16}$$

where ζ is the radial vorticity and k_0 is a positive constant. Equation (3.16) can be rewritten in terms of the potentials Ψ and Φ using (3.8) - (3.9) as

$$\nabla_h^2 \Phi = \mp k_0 \nabla_h^2 \Psi \tag{3.17}$$

The negative signs in (3.16) - (3.17) apply to the northern hemisphere, and the positive signs apply to the southern hemisphere. The sign difference in those two expressions is

attributed to the Coriolis force which deflects motions to the right in the northern hemisphere and to the left in the southern hemisphere. Therefore, upwelling is associated with clockwise motion (negative vorticity) in the northern hemisphere and with anticlockwise motion (positive vorticity) in the southern hemisphere.

The type of correlation in (3.16) - (3.17) can be viewed as the surface expression of a three-dimensional flow which has the kinematic property of helicity, defined as

$$H = \vec{\zeta} \cdot \vec{u} \tag{3.18}$$

where H is the helicity, $\vec{\zeta}$ is the vorticity vector and $\vec{u}$ is the three-dimensional velocity. According to (3.18), helicity appears in flows where there is a correlation between vorticity and velocity vectors. Often (but not always) the toroidal (or rotational) component of the motion is responsible for the radial vorticity and the poloidal (or convective) component of the motion is responsible for the radial velocity. I call this type of motion the *helical flow assumption* (3.16). I note that although the helicity vanishes on approach to the core-mantle boundary, the existence of upwelling motion correlated with vorticity implies non-zero helicity at greater depths. The helical flow assumption is illustrated in Fig. 3.1.

3.3.4 Columnar flow

A fourth way to couple toroidal and poloidal motions is to assume a columnar-type flow. According to the Taylor-Proudman theorem, in a purely columnar flow the velocity does not vary in the direction parallel to the rotation, i.e.

$$(\vec{\Omega} \cdot \nabla)\vec{u} = 0 \tag{3.19}$$

where $\vec{u}$ is again the full velocity vector and $\vec{\Omega}$ is the rotation vector. In a sphere, the curved boundaries do not allow the flow to be entirely independent of the $\vec{\Omega}$-direction. Still, the columnar nature of motions remains a characteristic feature in convection in rapidly

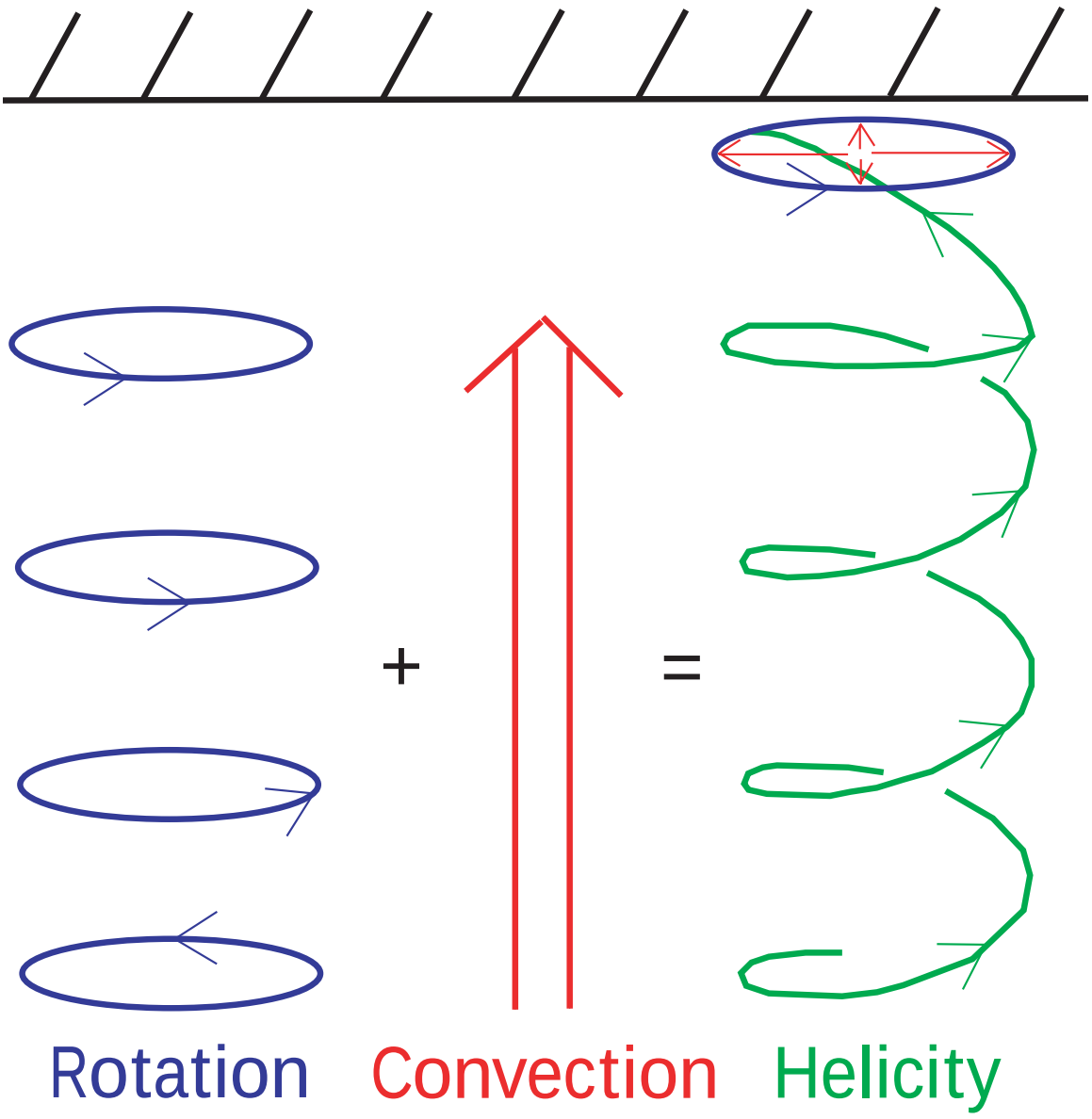

Figure 3.1: Schematic illustration of helical flow.

rotating fluid spheres (Busse, 1975), where these types of flow structures are known as "Busse columns".

Columnar flow is defined in (3.19) as a horizontal translation of a column of fluid as a whole; i.e. the velocity does not vary in the direction parallel to the rotation. In a sphere, the curved boundaries do not allow for such a flow. An approximation to columnar flow in a sphere is a fluid column which is stretched/shrunk as it moves along the cylindrical s-direction. Assuming uniform stretching and no-flux boundary conditions, the relationship between the velocity components in cylindrical coordinates u_s and u_z should be linear, so that everywhere along the fluid column

$$u_z = -\frac{\eta z}{L} u_s \tag{3.20}$$

where $\eta = s/\sqrt{R^2 - s^2}$ is the slope of the spherical shell, $L = \sqrt{R^2 - s^2}$ is half the height of the column and R is the sphere's radius. This assumption implies that the relative position of a particle in the fluid column is conserved. The ratio u_z/u_s on the boundary equals the slope of the spherical shell to satisfy the boundary conditions, and $u_z = 0$ at the equator (symmetry). Equation (3.20), together with the incompressible continuity equation, describe incompressible columnar flow in a sphere in cylindrical coordinates. My goal is to express the radial upwelling term $(\partial u_r/\partial r)$ on the boundary in spherical coordinates. Using conversions between spherical and cylindrical coordinate systems

$$u_z = u_r cos\theta - u_\theta sin\theta \tag{3.21}$$

$$u_s = u_\theta cos\theta + u_r sin\theta \tag{3.22}$$

and some algebraic manipulation, (3.20) becomes,

$$u_r(cos\theta + x sin\theta) = u_\theta(sin\theta - x cos\theta) \tag{3.23}$$

where

$$x = \frac{\eta z}{L} = \frac{r^2 sin\theta cos\theta}{R^2 - r^2 sin^2\theta} \tag{3.24}$$

Differentiation of (3.23) by r and evaluation at $r = R$ yields the upwelling term in spherical coordinates for a columnar flow in a sphere:

$$\frac{\partial u_r}{\partial r}(r = R) = -\frac{2tan\theta}{R}u_\theta \tag{3.25}$$

Using the incompressible continuity equation, the tangential divergence due to a columnar flow is

$$\nabla_h \cdot \vec{u}_h = \frac{2tan\theta}{R}u_\theta \tag{3.26}$$

Note that this expression differs from the tangential geostrophy upwelling expression (3.14) only by the factor 2. Equation (3.26) can be rewritten in terms of the two potentials Ψ and Φ using (3.6) - (3.7) and (3.9) as

$$\nabla_h^2 \Phi = \frac{2tan\theta}{R^2}(\frac{1}{sin\theta}\frac{\partial \Psi}{\partial \phi} + \frac{\partial \Phi}{\partial \theta}) \tag{3.27}$$

3.3.5 Upwelling relationships in geophysical fluids

Because there is no way to directly determine the relationship between Ψ and Φ at the top of the Earth's core, I look to other geophysical fluid systems for insight. Here I discuss several examples of upwelling flows commonly found in rotating fluids.

Examples of tangential geostrophy

Examples of tangential geostrophy are found in both the ocean and the atmosphere. In the subtropical ocean, the interior flow is governed by the Sverdrup relation (Sverdrup, 1947; Salmon, 1998)

$$\nabla_h \cdot \vec{u}_h = -\frac{\beta}{f}u_\theta \tag{3.28}$$

where θ is co-latitude. The Coriolis parameter f and its rate of change with co-latitude β are defined as

$$f = 2\Omega cos\theta \tag{3.29}$$

$$\beta = \frac{\partial f}{\partial y} = \frac{\partial f}{\partial \theta}\frac{\partial \theta}{\partial y} = -\frac{2\Omega sin\theta}{R} \tag{3.30}$$

where y is the local Cartesian northward coordinate, Ω is the Earth's rotation rate and R is the radius. Substitution of (3.29) - (3.30) into (3.28) yields

$$\nabla_h \cdot \vec{u}_h = \frac{2\Omega sin\theta}{2R\Omega cos\theta} u_\theta = \frac{tan\theta}{R} u_\theta \tag{3.31}$$

Equation (3.31) is identical to (3.14), i.e. the Sverdrup relation is equivalent to the tangential geostrophy assumption. Similar correlation between tangential divergence and meridional velocity was also reported by Sardeshmukh and Hoskins (1987, 1988) for solutions to the vorticity equation in the tropical atmosphere.

Examples of helical flow

There are numerous examples of helical flow in rotating fluids. In the atmosphere for example, a high/low pressure (in the northern hemisphere) is associated with a clockwise/anticlockwise circulation, according to the geostrophic balance. Deviation from this balance due to friction at the ground yields downwelling/upwelling. Therefore, the divergence of the tangential motion is correlated with the vorticity in the vertical direction. Velocity/vorticity correlation appears in observations and in numerical simulations of atmospheric tropical cyclones. Lilly (1986) found that long-lived stable rotating storms in the atmosphere are characterized by large values of helicity in both the storms and their surrounding environment.

Helicity and the type of correlation in (3.16) are also found in rotating convection. For example, at the onset of thermal convection in a plane layer of high Prandtl number fluid heated from below with rotation in the presence of a uniform vertical magnetic field, the instability sets in as stationary convection. For the case of convection between two free horizontal boundaries, the depth-dependent vertical velocity, tangential divergence and

vertical vorticity are given by (Chandrasekhar, 1961)

$$w = \pm w_0 sin(\frac{\pi z}{d}) \tag{3.32}$$

$$\nabla_h \cdot \vec{u}_h = \mp w_0 \frac{\pi}{d} cos(\frac{\pi z}{d}) \tag{3.33}$$

$$\zeta = (\frac{1}{dE}) \frac{\pi(\pi^2 + a^2)}{(\pi^2 + a^2)^2 + Q\pi^2} w_0 cos(\frac{\pi z}{d}) \tag{3.34}$$

where z is the vertical Cartesian coordinate (anti-parallel to gravity), d is the depth of the fluid layer, w_0 is the vertical velocity at $z = d/2$, a is the non-dimensional convection cell width ($a = kd$ where k is the wave number), E is the Ekman number (the ratio between viscous to rotation forces) and Q is the Chandrasekhar number (the ratio between magnetic to viscous forces). The upper sign in (3.32) - (3.33) applies to a northern hemisphere geometry (anticlockwise rotation of the fluid layer) and the lower sign applies to a southern hemisphere geometry (clockwise rotation of the fluid layer). The helicity for this flow is found by substituting (3.32) and (3.34) into (3.18),

$$H = \pm(\frac{1}{dE}) \frac{\pi(\pi^2 + a^2)}{(\pi^2 + a^2)^2 + Q\pi^2} w_0^2 cos(\frac{\pi z}{d}) sin(\frac{\pi z}{d}) \tag{3.35}$$

In this example the helicity depends on depth. At the boundaries $(z = 0, d)$ and at midway $(z = d/2)$ the helicity vanishes. In the northern hemisphere the helicity is negative/positive in the upper/lower half of the fluid layer, respectively. The ratio of the tangential divergence to the vertical vorticity is, from (3.33) - (3.34),

$$\frac{\nabla_h \cdot \vec{u}_h}{\zeta} = \mp k_0 = \mp E[\frac{(\pi^2 + a^2)^2 + Q\pi^2}{(\pi^2 + a^2)}] \tag{3.36}$$

Note that the divergence/vorticity ratio in (3.36) is independent of depth. In the northern hemisphere, at the lower/upper half of the fluid layer, convergence/divergence are associated with positive/negative vorticity, respectively.

Two special cases of (3.36) deserve special note in this context. First, in the case of no magnetic field ($Q = 0$, i.e. purely rotating convection), $a \rightarrow (\frac{1}{2}\pi^2)^{1/6} E^{-1/3}$ in the

limit of small Ekman number (Chandrasekhar, 1961). According to the Prandtl turbulence hypothesis all the effective diffusivities are equal, i.e., $\nu = \lambda = 1\ m^2/s$, therefore $E \simeq 10^{-9}$, and (3.36) gives $k_0 \simeq 10^{-3}$. Second, in the more general case where both rotation and magnetic field are present, k_0 is larger. For typical core values of $E \simeq 10^{-9}$ and $Q \simeq 10^9$, Chandrasekhar (1961) shows that $a \simeq \sqrt{1.5}\pi$ at the onset of convection. Substituting these values into (3.36) gives $k_0 \simeq 0.4$, within the range of values that I use in this chapter.

Based on results from numerical dynamos, it has been proposed that helicity is present in convection in the outer core. Olson et al. (1999) found in dynamo simulations columnar convection with large amounts of helicity with opposite signs in the two hemispheres. Results of convective dynamo simulations display a constant of proportionality (~ 0.07) between the tangential divergence and the vertical vorticity of the fluid flow at the outer core just below the core-mantle boundary (Olson et al., 2002).

Another example of helical flow in rotating fluids is an Ekman boundary layer. The horizontal velocity components in a laminar Ekman layer with a top rigid boundary are, in a local Cartesian coordinate system (e.g. Kundu, 1990; Cushman-Roisin, 1994; Andrews, 2000)

$$u = U[1 - e^{z/\delta} cos(z/\delta)] \tag{3.37}$$

$$v = \mp U e^{z/\delta} sin(z/\delta) \tag{3.38}$$

where u and v are the x (eastward) and y (northward) velocity components respectively, U is the y-dependent zonal velocity far from the boundary layer, and z is the vertical coordinate directed out of the boundary, so that $z = 0$ at the boundary and $z < 0$ at the interior in (3.37) - (3.38). The negative sign in (3.38) applies in the northern hemisphere and the positive sign applies in the southern hemisphere. The thickness δ of the Ekman boundary layer is given by

$$\delta = \sqrt{\frac{2\nu}{|f_0|}} \tag{3.39}$$

where ν is the kinematic viscosity and $f_0 = 2\Omega cos\theta_0$ is the f-plane approximation to the Coriolis parameter, where Ω is the Earth's rotation rate and θ_0 is the local co-latitude. The depth-dependent horizontal divergence and vertical vorticity derived from (3.37) - (3.38) are

$$\nabla_h \cdot \vec{u}_h = \frac{\partial u}{\partial x} + \frac{\partial v}{\partial y} = \mp \frac{\partial U}{\partial y} e^{z/\delta} sin(z/\delta) \tag{3.40}$$

$$\zeta = \frac{\partial u}{\partial y} - \frac{\partial v}{\partial x} = \frac{\partial U}{\partial y}[1 - e^{z/\delta} cos(z/\delta)] \tag{3.41}$$

The depth-dependent vertical velocity associated with (3.40) is

$$w = -\int_z^0 \nabla_h \cdot \vec{u}_h(z')dz' = \mp \frac{\delta}{2} \frac{\partial U}{\partial y}[e^{z/\delta}(sin(z/\delta) - cos(z/\delta)) + 1] \tag{3.42}$$

Substituting (3.41) - (3.42) into (3.18) gives the depth-dependent helicity of the flow through an Ekman boundary layer,

$$H = \zeta w = \mp \frac{\delta}{2} (\frac{\partial U}{\partial y})^2 [1 - e^{z/\delta} cos(z/\delta)][e^{z/\delta}(sin(z/\delta) - cos(z/\delta)) + 1] \tag{3.43}$$

From (3.40) - (3.41), the ratio between horizontal divergence and vertical vorticity in this case is

$$\frac{\nabla_h \cdot \vec{u}_h}{\zeta} = \mp k_0 = \mp \frac{e^{z/\delta} sin(z/\delta)}{1 - e^{z/\delta} cos(z/\delta)} \tag{3.44}$$

As in the previous example of rotating convection, the ratio between horizontal divergence and vertical vorticity (3.44) is independent of the tangential coordinates. In a rotating, convecting layer this ratio was also independent of depth, whereas in an Ekman boundary layer this ratio varies with depth. Fig. 3.2 shows the normalized helicity and the depth-dependent divergence/vorticity ratio for an Ekman boundary layer in the northern hemisphere geometry, according to (3.43) - (3.44). H in (3.43) is negative/positive and the ratio in (3.44) is positive/negative throughout the northern/southern hemisphere, respectively. k_0 goes asymptotically to zero far from the boundary layer (practically vanishes at $z \simeq 3\delta$), and $k_0(z = \delta) = 0.39$. From Fig. 3.17 it is evident that H and k_0 are anti-correlated. The

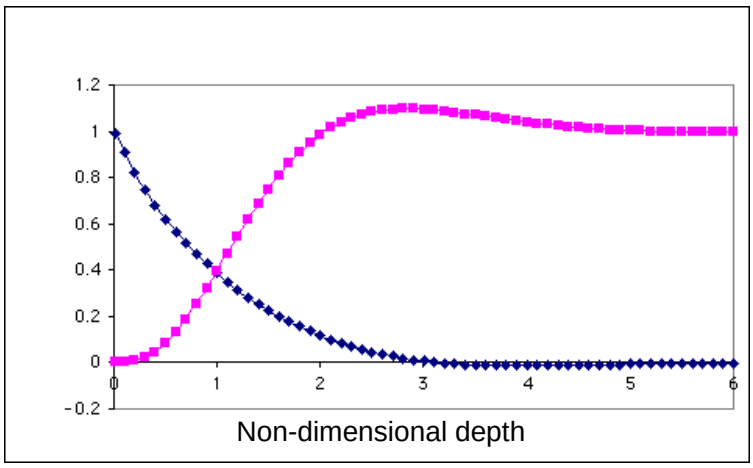

Figure 3.2: Divergence/vorticity ratio and normalized helicity as a function of depth in an Ekman boundary layer in the southern hemisphere. Squares denote the ratio between tangential divergence to radial vorticity k_0 in (3.44), and diamonds denote the normalized helicity $-H/[(\delta/2)(\partial U/\partial y)^2]$ in (3.43).

helicity is large far from the boundary layer where velocity and vorticity correlate, and k_0 vanishes far from the boundary layer due to the lack of horizontal divergence there. The surface expression of such flow is large k_0 values due to the divergence/vorticity correlation, and the helicity vanishes at the surface where the flow becomes two dimensional. Thus, I use the term "helical" to describe a flow which has large helicity in the interior, and its surface expression is the correlation between tangential divergence and radial vorticity.

To summarize, the ratio between tangential divergence and radial vorticity in helical flow changes sign across the equator and is independent of the tangential coordinates in both an Ekman boundary layer and rotating, convecting layer. However, the depth dependence is different in the two situations. From these results, I infer that the parameter k_0 may be tangentially uniform in the core, but its depth-variation in the outer core is uncertain. Therefore I test different values of k_0. For upwelling models such as strong helicity, tangential geostrophy, and columnar flow, I use a small value of $k_0 = 0.1$. In my test case, this value yields an advective limit solution. I use $k_0 = 0.5$ for the weak helicity case to

examine the effect of different k_0 values on my solution.

3.3.6 General upwelling relationship

The helical flow and tangential geostrophy upwelling terms can be superimposed, due to the linear relationship between geostrophic and boundary layer effects, similar to the superposition of pressure-driven and stress-driven horizontal velocities in an Ekman boundary layer. A general expression for the tangential divergence that incorporates the helical flow (3.17), tangential geostrophy (3.15), columnar flow (3.27) and pure toroidal flow (3.11) assumptions is

$$\nabla \cdot \vec{u}_h = \nabla_h^2 \Phi = \mp k_0 \nabla_h^2 \Psi + c \frac{tan\theta}{R^2} (\frac{1}{sin\theta} \frac{\partial \Psi}{\partial \phi} + \frac{\partial \Phi}{\partial \theta}) \tag{3.45}$$

where the negative sign in the first term on the right hand side applies in the northern hemisphere and the positive sign in the same term applies in the southern hemisphere. Different values of k_0 and c in (3.45) define all the physical assumptions discussed above: $k_0 = c = 0$ for pure toroidal flow, $k_0 = 0$ and $c = 1$ for tangential geostrophy, $k_0 \neq 0$ and $c = 0$ for helical flow, $k_0 = 0$ and $c = 2$ for columnar flow. Together, (3.45) and (5.12) constitute a set of two equations for the two unknowns, the potentials Ψ and Φ.

Two limits of (3.45) are worth noting. For large values of k_0 (and away from the equator), the first term on the right hand side in (3.45) is dominant, yielding a proportionality between surface divergence and radial vorticity. In this limit, poloidal velocity sources coincide with toroidal vortex centers. The other limit is for small values of k_0 (and at low latitudes). In this limit, the second term on the right hand side in (3.45), is dominant. This correlation produces centers of divergence where the meridional velocity is large.

3.3.7 Non-uniqueness and "invisible" flow

Non-uniqueness in the inversion of the magnetic induction equation occurs in situations where some component of the flow (often termed the "null space") is "invisible", i.e. does not generate secular variation of its own (Backus and LeMouël, 1986). For pure toroidal flow, motions parallel to contours of B_r are "invisible". For tangential geostrophy, the flow is "invisible" along contours of $B_r/cos\theta$ which do not cross the equator (Chulliat and Hulot, 2000). Therefore, both assumptions have "invisible" flows, but the non-uniqueness in tangential geostrophy is confined to ambiguous patches and is more restricted than in pure toroidal flow.

Here I derive an equation governing the "invisible" motion with the helical flow assumption included. According to (5.10), the "invisible" flow consistent with the frozen flux magnetic induction equation obeys

$$\nabla_h \cdot (B_r \vec{u}_h^i) = 0 \tag{3.46}$$

where $\vec{u}_h^i$ denotes the "invisible" flow. The tangentially non-divergent vector $B_r \vec{u}_h^i$ can be expressed in terms of a scalar potential Γ as follows (Backus, 1968; Backus and LeMouël, 1986):

$$B_r \vec{u}_h^i = \nabla \times \Gamma \hat{r} \tag{3.47}$$

According to (3.47), the tangential divergence of the "invisible" flow is given by

$$\nabla_h \cdot \vec{u}_h^i = \frac{1}{{B_r}^2 R^2 sin\theta}\left(\frac{\partial B_r}{\partial \phi}\frac{\partial \Gamma}{\partial \theta} - \frac{\partial B_r}{\partial \theta}\frac{\partial \Gamma}{\partial \phi}\right) \tag{3.48}$$

Equation (3.45) can be written using the "invisible" flow components:

$$\nabla_h \cdot \vec{u}_h^i = \mp k_0 \hat{r} \cdot \nabla \times \vec{u}^i + c\frac{tan\theta}{R} u_\theta^i \tag{3.49}$$

Substitution of the "invisible" velocity components defined in (3.47) into the right hand

side of (3.49), equating with the right hand side of (3.48), and rearranging, yields

$$(\frac{\partial B_r}{\partial \phi} \pm k_0 sin\theta \frac{\partial B_r}{\partial \theta})\frac{\partial \Gamma}{\partial \theta} - (\frac{\partial B_r}{\partial \theta} + cB_r tan\theta \mp k_0 \frac{1}{sin\theta}\frac{\partial B_r}{\partial \phi})\frac{\partial \Gamma}{\partial \phi} = \pm k_0 B_r R^2 sin\theta {\nabla_h}^2 \Gamma \tag{3.50}$$

an equation for the scalar Γ with spatially-variable coefficients. For pure toroidal flow (i.e. $k_0 = c = 0$), the solution to (3.50) is $\Gamma = B_r$, and for tangential geostrophy (i.e. $k_0 = 0$, $c = 1$), the solution is $\Gamma = B_r/cos\theta$, as expected. For combined helical flow and tangential geostrophy (i.e. $k_0 \neq 0$, $c = 1$), (3.50) is an elliptic partial differential equation. According to the maximum principle of E. Hopf, a non-constant solution of equations of this type can attain neither a maximum nor a minimum at an interior point (Protter and Weinberger, 1967). All points are interior on a surface of a sphere, so that only the trivial solution, $\Gamma = constant$, exists. Therefore, the "invisible" flow defined by (3.47) is identically zero, i.e. the non-uniqueness associated with "invisible" flow is removed when helical flow is included. This is a reason why solutions with the helical flow assumption may contain more flow along B_r-contours than do previous solutions.

3.4 Numerical method

For numerical solution, I rewrite (5.12) and (3.45) as advection-diffusion equations for Ψ and Φ of the form

$$\frac{\partial \Psi}{\partial \tau} = \frac{\partial B_r}{\partial t} + \frac{1}{R^2 sin\theta}(\frac{\partial \Psi}{\partial \phi}\frac{\partial B_r}{\partial \theta} - \frac{\partial \Psi}{\partial \theta}\frac{\partial B_r}{\partial \phi}) + \frac{1}{R^2}(\frac{\partial \Phi}{\partial \theta}\frac{\partial B_r}{\partial \theta} + \frac{1}{sin^2\theta}\frac{\partial \Phi}{\partial \phi}\frac{\partial B_r}{\partial \phi}) + B_r \nabla_h^2 \Phi \tag{3.51}$$

$$\frac{\partial \Phi}{\partial \tau} = \nabla_h^2 \Phi - (\mp k_0 \nabla_h^2 \Psi + c\frac{tan\theta}{R^2}(\frac{1}{sin\theta}\frac{\partial \Psi}{\partial \phi} + \frac{\partial \Phi}{\partial \theta})) \tag{3.52}$$

where τ is a relaxation variable and $\partial B_r/\partial t$ is the source term. In (3.52), the coefficient $-k_0$ applies in the northern hemisphere, and $+k_0$ applies in the southern hemisphere. I use B_r and $\partial B_r/\partial t$ on the core-mantle boundary in (3.51) - (3.52), but like previous authors,

I interpret Ψ and Φ at the top of the free stream below the core-mantle boundary. I solve (3.51) - (3.52) simultaneously for the two potentials Ψ and Φ using an iterative technique, starting from initial conditions $\Psi = \Phi = 0$. The Laplacian operators act to diffuse the residuals in (3.51) - (3.52) and allow the spatial variations of the time-like derivatives $\partial\Psi/\partial\tau$ and $\partial\Phi/\partial\tau$ to converge after a certain number of iterations. I use a second order, central finite difference method on regular $5^\circ \times 5^\circ$ and in one case $2.5^\circ \times 2.5^\circ$ grids that avoid the two poles and the equator. To verify that non-uniqueness is practically removed, I solved (3.51) - (3.52) using different initial conditions and obtained the same final solutions.

It is well known that finite difference methods in spherical coordinates often have problems at the poles. I treat the polar points as follows. I calculate the derivatives of the potentials Ψ and Φ at the latitude points closest to the poles, using the value of Ψ and Φ at the polar point itself in the finite difference formulas. The values at the poles are then re-calculated as the average of the values of the potentials over the closest latitude grid line. With this method, streamlines are free to cross (or not to cross) the poles.

The equator requires special treatment for the last term in (3.52), which is singular there. For $c \neq 0$, (5.12) and (3.45) at the equator reduce to

$$\frac{\partial\Psi}{\partial\phi}|_{eq} = -\frac{\partial\Phi}{\partial\theta}|_{eq} \tag{3.53}$$

I add an hypothetical equatorial grid line to enforce (3.53). Cross-equator values are used to calculate $\partial\Phi/\partial\theta$, and then (3.53) is integrated to obtain Ψ on the equator. The equatorial Ψ-values found this way are then used to calculate $\partial\Psi/\partial\theta$ and $\partial^2\Psi/\partial\theta^2$ at latitudes nearest to the equator. I further approximate the last term in (3.52) on the nearest latitudes to the equator using (3.53), which becomes

$$\frac{\partial\Phi}{\partial\tau}|_{eq} = \nabla_h^2\Phi|_{eq} - (\mp k_0\nabla_h^2\Psi + c\frac{tan\theta}{R^2}(\frac{1}{sin\theta} - 1)\frac{\partial\Psi}{\partial\phi})|_{eq} \tag{3.54}$$

My finite difference relaxation solution method has some limitations. The coefficient $\mp k_0 B_r$, which acts like a spatially-variable streamfunction diffusivity, has to exceed some

minimum value that depends on the grid size in order to reach numerical convergence. Furthermore, $\mp k_0 B_r$ must maintain the same sign over the entire grid, otherwise locally negative diffusivity will produce numerical instability in those regions. To overcome these limitations, I use a smoothed version for B_r only for the last term on the right hand side of (3.51), to guarantee numerical stability in the vicinity of null flux areas where $B_r = 0$ and inside reversed flux patches where B_r changes sign.

3.4.1 Test case

In order to verify the reliability of my method, I examine solutions of a synthetic test case. I choose the simple case of a dipole magnetic field with its pole located at latitude θ_0 and longitude $\phi_0 = 0$, rotating along the longitude $\phi_0 = 0$ at constant angular velocity ω. The instantaneous radial magnetic field for this case is given by

$$B_r = cos(\theta_0 + \omega t)cos\theta + sin(\theta_0 + \omega t)sin\theta cos\phi \tag{3.55}$$

and the secular variation induced by the rotation is

$$\frac{\partial B_r}{\partial t} = -\omega sin(\theta_0 + \omega t)cos\theta + \omega cos(\theta_0 + \omega t)sin\theta cos\phi \tag{3.56}$$

The streamfunction found by substituting (3.55) - (3.56) into (3.51) - (3.52) using $k_0 = 0.1$, $c = 0$, $\omega = 1\ ^\circ$/yr and $\theta_0 = 45N$ is shown in Fig. 3.3. This map conforms to the expected pattern of uniform rotation perpendicular to the equatorial plane and parallel to the $\phi_0 = 0$ longitude. The magnitude of the flow is also nearly correct; the average angular velocity has an error of 3.2%, compatible to the discretization error on the $5^\circ \times 5^\circ$ grid. Various values of ω and θ_0 were tested and produced similar results to those shown in Fig. 3.3 in terms of accuracy of pattern and magnitude. This test case verifies the convergence of (3.51) for Ψ in its advective limit, i.e., small amounts of streamfunction diffusion ($k_0 = 0.1$) stabilize the solution and only slightly modify the pure toroidal character of the flow. To verify the

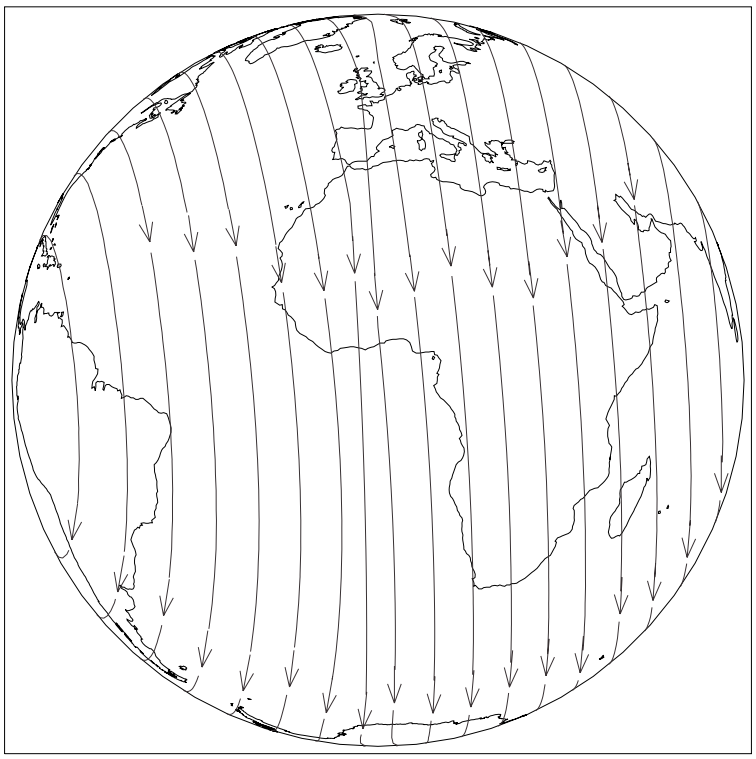

Figure 3.3: Streamfunction for the test case of a dipole magnetic field with instantaneous pole at $[\phi_0, \theta_0] = [0, 45N]$ and rotating perpendicular to the equatorial plane and parallel to the $\phi_0 = 0$ longitude line at a constant angular velocity $\omega = 1\ ^\circ$/yr, with $k_0 = 0.1$.

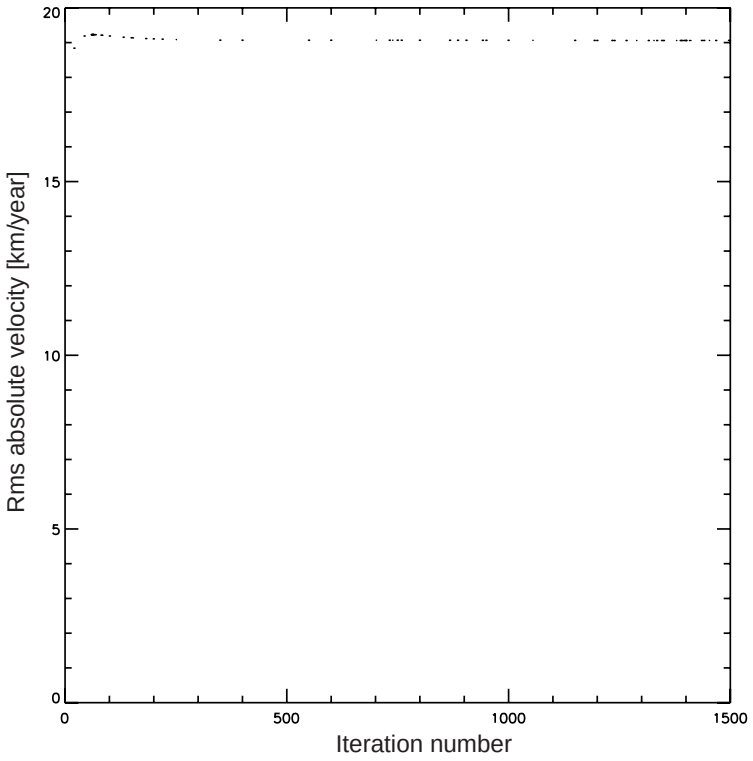

Figure 3.4: Rms absolute velocity as a function of iteration number for the tangential geostrophy case 1. The asymptotic curve verifies numerical convergence.

convergence of (3.52), I check that Ψ satisfies the tangential divergence expression (3.45). I have also verified this convergence in each of my real data cases.

Fig. 3.4 demonstrates the convergence of the solution for my main flow case (which will be defined and discussed below). I plot the rms absolute velocity over the entire grid as a function of iteration number, which shows the convergence to an asymptotic value.

3.5 Core flow cases

Fig. 1.3 shows the radial geomagnetic field and secular variation models on the core-mantle boundary from the 2000 Ørsted and 1980 Magsat satellites, truncated at spherical harmonic degree 14. The magnetic field model for 1990 in Fig. 1.3 is the average of the

Øersted and the Magsat field models, and the secular variation at 1990 is their difference divided by 20 years. These field models were used in (3.51) - (3.52) to obtain flow maps that correspond to the cases described above: Tangential geostrophy, strong and weak helicity, and columnar flow.

case	**characterization**	k_0	c	Δ	**max values**			**rms values**		
					u_{tor}	u_{pol}	u_{abs}	u_{tor}	u_{pol}	u_{abs}
1	Tangential geostrophy	0.1	1	5	84.6	33.5	79.9	19.0	3.9	19.4
2	Sensitivity test	0.1	1	5	41.5	10.2	49.6	11.8	2.9	12.1
3	Resolution test	0.1	1	2.5	134.0	33.9	141.4	26.3	6.0	26.9
4	Strong helicity	0.1	0	5	83.0	36.3	84.2	21.0	2.2	21.1
5	Weak helicity	0.5	0	5	22.8	11.7	25.6	6.2	3.1	6.9
6	Columnar flow	0.1	2	5	130.3	46.8	173.4	21.7	8.5	22.2

Table 3.1: Maximum and mean velocities for different cases. k_0 and c values refer to equation (3.45), Δ is grid size in degrees. All values are in km/yr.

Table 3.1 defines the different flow cases and summarizes the core-mantle boundary surface rms and maximum values for the various solutions. The values of k_0 and c define the various upwelling models used in each case, according to (3.45). The characterization in Table 3.1 identifies the most important among the different terms in the upwelling expression for each case. In case 1, a small value of k_0 and $c = 1$ indicates that tangential geostrophy is dominant. In case 2, the sensitivity of the method is investigated by using a filtered model for the secular variation with the same upwelling model as in case 1. In case 3, I examine the effects of grid resolution using the same upwelling model as in case 1 but on a finer grid. In case 4, a small value of k_0 and $c = 0$ simulates flow with strong helicity. In case 5, a relatively large k_0 value is used in order to provide the effect of weak helicity. In case 6, a small value of k_0 and $c = 2$ means that columnar flow is the dominant source of upwelling. Surface rms values are the surface average of the absolute pointwise values, and maximum values are the maximum absolute values. The quantities u_{tor}, u_{pol} and u_{abs} denote the toroidal, poloidal and absolute velocities, respectively.

case	data misfit (%)	divergence misfit (%)
1	0.00	0.14
2	0.00	1.29
3	1.08	1.21
4	0.38	0.63
5	1.53	0.81
6	0.04	0.34

Table 3.2: Misfit values for different cases.

The quality of convergence is defined by two misfits. The first is the data misfit, defined as the ratio of the rms data residual $< \partial\Psi/\partial\tau >$ to the rms secular variation $< \partial B_r/\partial t >$ over the entire grid. The second is the divergence misfit, the ratio of the rms tangential divergence residual $< \partial\Phi/\partial\tau >$ to the rms tangential divergence $< \nabla_h^2\Phi >$ over the entire grid. Table 3.2 summarizes the quality of the different solutions in terms of their misfits.

I begin by describing my tangential geostrophy solution (case 1) and I compare it to tangential geostrophy solutions previously obtained by others. I then use a sensitivity test to demonstrate the robustness of my solution method with respect to small-scale variations in the data (case 2). I then show a resolution test in which I re-solve case 1 on a finer grid. I compare the flows from cases 1, 4, 5 and 6 to investigate the effect of different upwelling models. Finally, I focus on some areas in case 1 that illustrate different kinematic scenarios which lead to the observed secular variation at the core-mantle boundary.

3.5.1 Tangential geostrophy case

Fig. 3.5a shows the flow map for the tangential geostrophy case. I name this case "tangential geostrophy" due to the dominance of the tangential geostrophy assumption in (3.16), even though the upwelling model in this case also includes the helical flow term. The dominant features in the solution are a large anticlockwise circulation in the southern

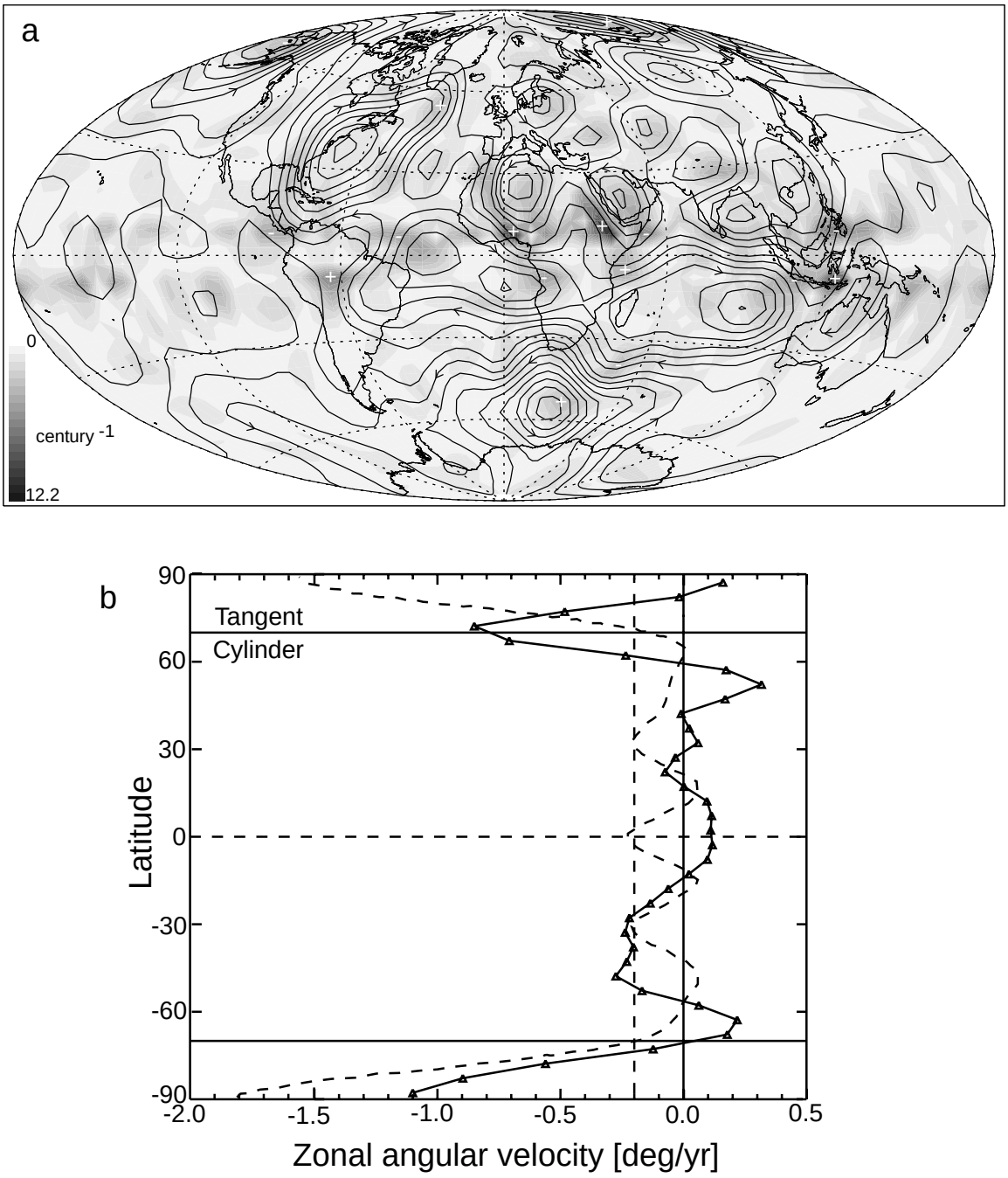

Figure 3.5: Flow map (a) and zonal velocity profile (b) beneath the core-mantle boundary for the tangential geostrophy case 1 from table 3.1. Contours in (a) are streamlines of the flow, grey scale represents absolute upwelling value, with + and - signs indicate upwelling and downwelling, respectively. In (b) the traditional $0.2\ ^\circ$/yr westward drift value is marked by a solid line and the zonal flow of Hulot et al. (2002) is shown by a dashed line for comparison.

hemisphere centered beneath southern Africa and Antarctica, a strong clockwise vortex centered below Bermuda, and a westward drift sweeping most of the Atlantic southern hemisphere. The Atlantic hemisphere has overall higher velocities than the Pacific, and the secular variation is also higher there (see Fig. 1.3b). Note that the flow has a much larger length scale than does the secular variation. The solution contains a significant amount of flow along B_r-contours. The average ratio of the velocity component parallel to B_r-contours to the velocity component perpendicular to the same contours is about 1.2 (see Table 3.3).

case	$< \vec{v}_{\|} > / < \vec{v}_{\perp} >$	$v_\theta^{eq}/v_\phi^{eq}$	**sym/skew**
1	1.18	1.07	1.02
2	1.23	0.48	1.94
3	1.27	0.48	1.86
4	1.19	1.06	1.01
5	1.17	1.20	0.22
6	1.20	0.73	0.83

Table 3.3: Velocity ratios for different cases. $<>$ denotes the rms value over the entire grid. $\vec{v}_{\|}$ and $\vec{v}_{\perp}$ denote the parallel and perpendicular velocity components, respectively, with respect to the local direction of a B_r contour. v_θ^{eq} and v_ϕ^{eq} denote the meridional and azimuthal flow components, respectively, averaged along the two closest latitudes to the equator. Sym/skew denotes the ratio of equatorially symmetric to antisymmetric zonal flow.

The solution in Fig. 3.5a shows some cross-equator flow. This flow is present in this solution for two reasons. First, the tangential divergence includes the helical flow assumption as well as tangential geostrophy. Second, my grid skips the equator itself. The mean equatorial meridional/azimuthal ratio is given in Table 3.3.

The solution contains intense vortices and jets. A clockwise vortex below Siberia coincides with an intense secular variation structure there (compare Figs. 1.3b and 3.5a). A localized jet begins beneath the Indian ocean, continues north-west beneath southern Africa and can be traced westward into the South Atlantic. This structure overlaps an intense sec-

ular variation bipolar structure aligned with the flow (again see Figs. 1.3b and 3.5a). The strongest upwellings occur near the equator, a consequence of the latitudinal dependence in the tangential geostrophy term in (3.45). Away from the equator, the upwellings are weaker and located at vortex centers, a consequence of the helical flow term in (3.45).

The zonal velocity profile for the tangential geostrophy case shown in Fig. 3.5b displays equal amounts of symmetry and antisymmetry with respect to the equator (see Table 3.3). Equatorial symmetry in the zonal velocity is consistent with a geostrophic force balance and may indicate the existence of axisymmetric columnar flow (Jault et al., 1988; Jackson et al., 1993). The zonal angular velocity in mid-latitudes of the southern hemisphere is in agreement with the traditional $0.2\ ^\circ$/yr westward drift value, but the zonal angular velocity at other latitudes is smaller and, in places, eastward. Fig. 3.5b includes the zonal velocity profile obtained by Hulot et al. (2002) for the same data sets. Note that my solution is less symmetric than theirs with respect to the equator. My zonal velocity profile suggests relatively strong westward polar vortices. However, due to the small surface area of the polar cap with respect to the data resolution, these structures are very uncertain. The existence of polar vortices was argued on the basis of numerical models (Olson and Aurnou, 1999), flow inversions (Hulot et al., 2002) and lab experiments (Aurnou et al., 2003). I find that westward polar vortices are suggested, though not well resolved in my solution. A local solution for the polar regions may shed more light on this question.

3.5.2 Sensitivity test

The geomagnetic field and the secular variation models I use are based on the Ørsted and Magsat data up to spherical harmonic degree 14. In order to check the robustness of my solution with respect to small changes in the geomagnetic field model, I perform the following sensitivity test. I smooth each geomagnetic field model with a quarter cosine filter from $l_{min} = 1$ to $l_{max} = 13$, meaning that the $l = 1$ spherical harmonic is not filtered

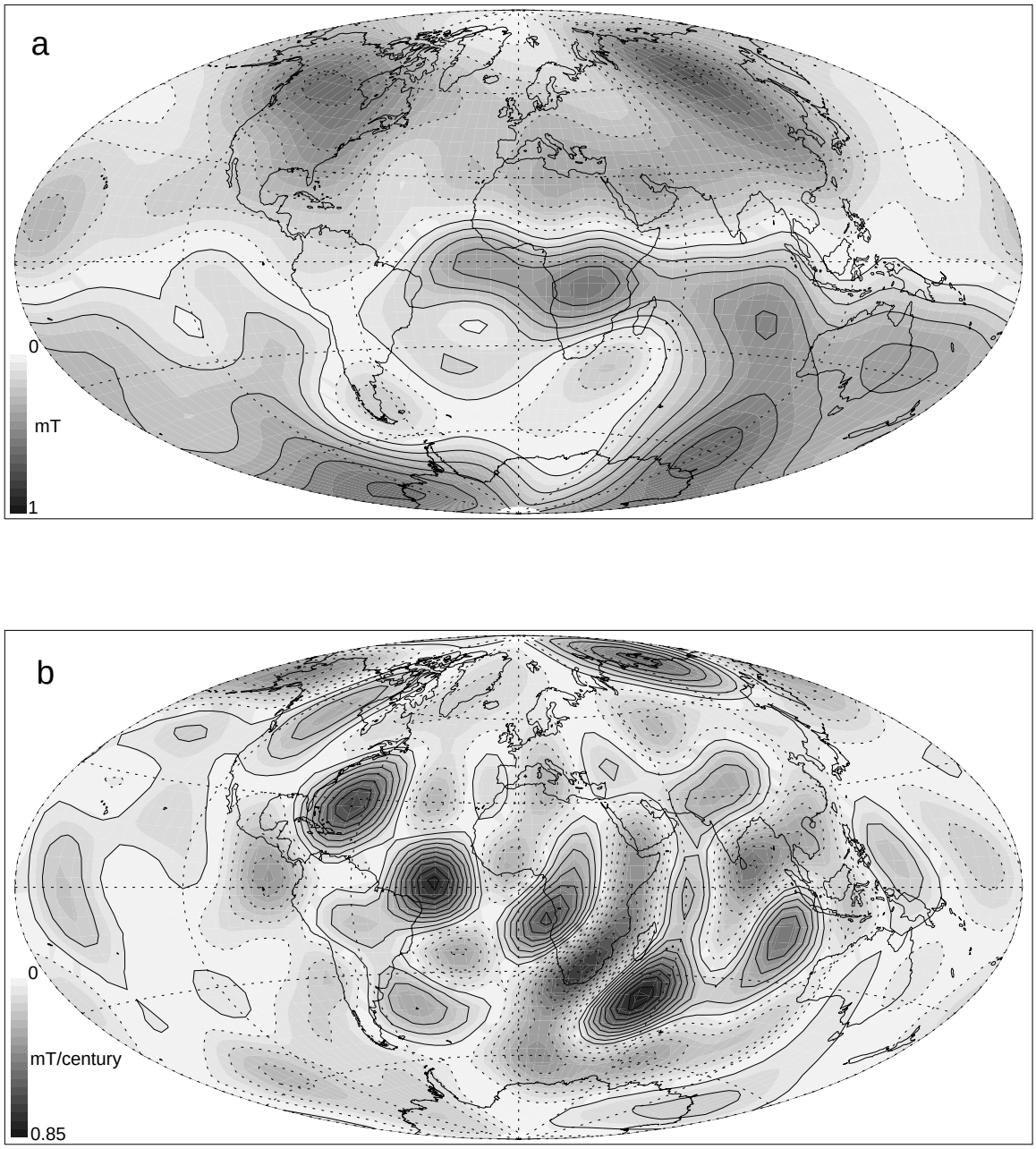

Figure 3.6: Sensitivity test. Radial magnetic field (a), secular variation (b) on the core-mantle boundary, flow map (c) and zonal velocity profile (d) beneath the core-mantle boundary for low-pass filter (quarter cosine from $l_{min} = 1$ to $l_{max} = 13$) case 2 from table 3.1. In (a) and (b) grey scale represents absolute values, solid lines are positive, dotted lines are negative. Note that the scale in (b) is magnified to depict the reduced secular variation with respect to the unfiltered secular variation in Fig. 1.3b. Contours in (c) are streamlines, grey scale represents absolute upwelling value, + and - signs indicate upwelling and downwelling, respectively. The contour interval in (c) is the same as in Fig. 3.5a.

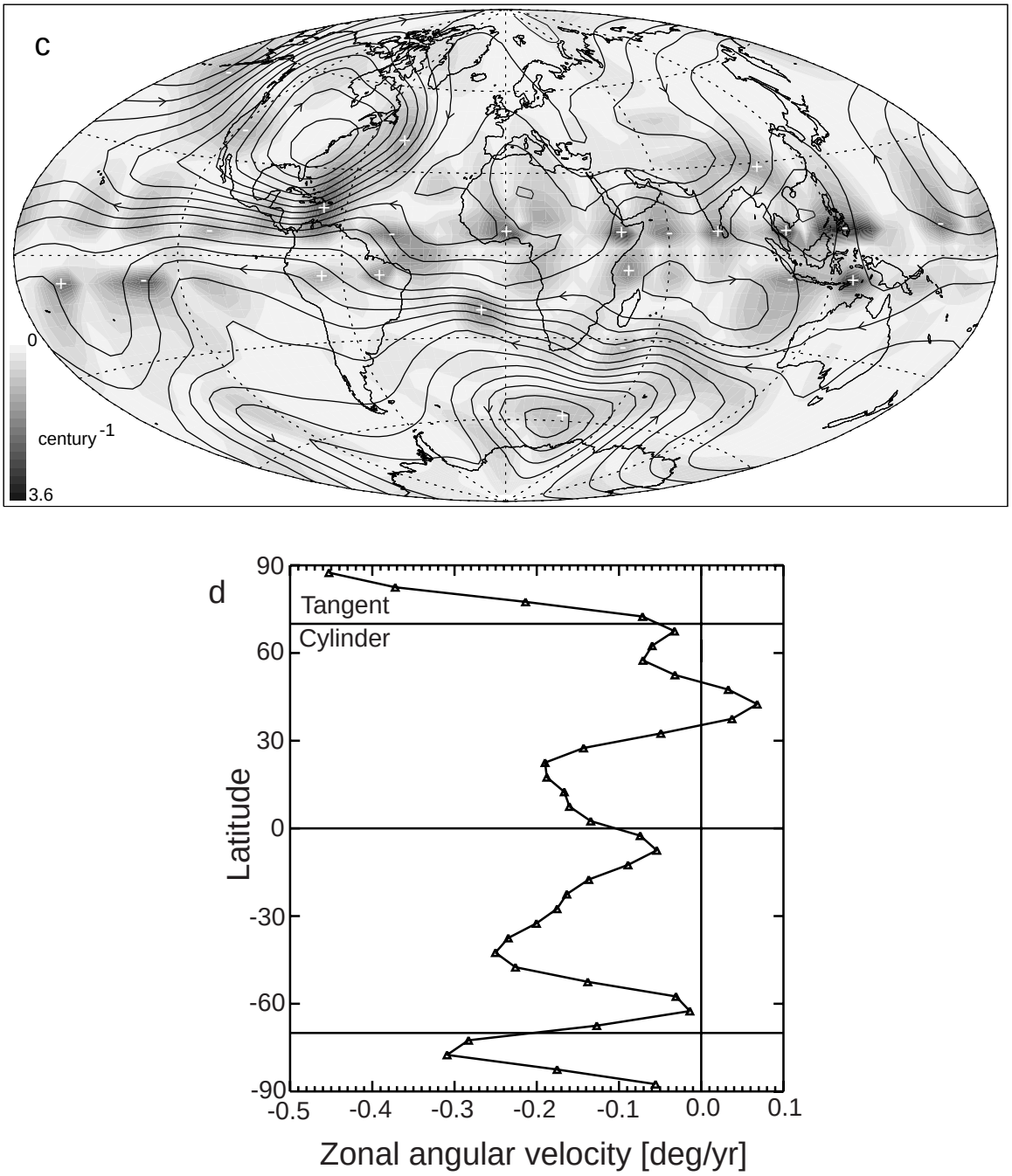

Figure 3.6: Continued.

at all, the harmonics $l = 13$ and $l = 14$ are completely removed, and the intermediate ones are progressively filtered (see Figs. 3.6a and 3.6b). This type of filtering is intended to mitigate the increasing uncertainty in the secular variation power spectrum at high spherical harmonic degrees (Hulot et al., 2002). The streamfunction and zonal velocity profile of the sensitivity test using the same upwelling as in case 1 are shown in Figs. 3.6c and 3.6d. The solution is a smoother version of the non-truncated solution (compare Figs. 3.5a and 3.6c), with the main features present in both cases. I conclude on the basis of this test that my solution technique is robust for large flow structures, and these large structures are relatively insensitive to short wavelength errors in the secular variation model. However, using smoothed data substantially reduces smaller structures such as the polar vortices and therefore those should not be considered as very robust. The sensitivity test case contains a more equatorially-aligned flow and a more symmetric zonal flow with respect to the equator than the tangential geostrophy case 1 (see Table 3.3 for comparison).

3.5.3 Resolution test

I have examined the effects of grid size on my flow solutions using calculations made on a refined $2.5^\circ \times 2.5^\circ$ grid, again avoiding the equator and poles. The streamfunction and zonal velocity profile of this resolution test using the same upwelling as in case 1 are shown in Figs. 3.7a and 3.7b. Note that the contour interval is different than the one in Fig. 3.5a (see details in caption of Fig. 3.7). The solution is much more energetic (see larger velocity values in Table 3.1) and contains much more small scale flow than the solution on the coarser grid (compare Figs. 3.5a and 3.7a), but the large scale circulation is similar in both cases. Two significant differences between cases 1 and 3 are worth noting. First, the flow in the resolution test case is much more aligned with equator (compare Figs. 3.5a and 3.7a, and also see Table 3.3). Second, the resolution test case displays more symmetry in the zonal flow with respect to the equator than the tangential geostrophy case (compare Figs.

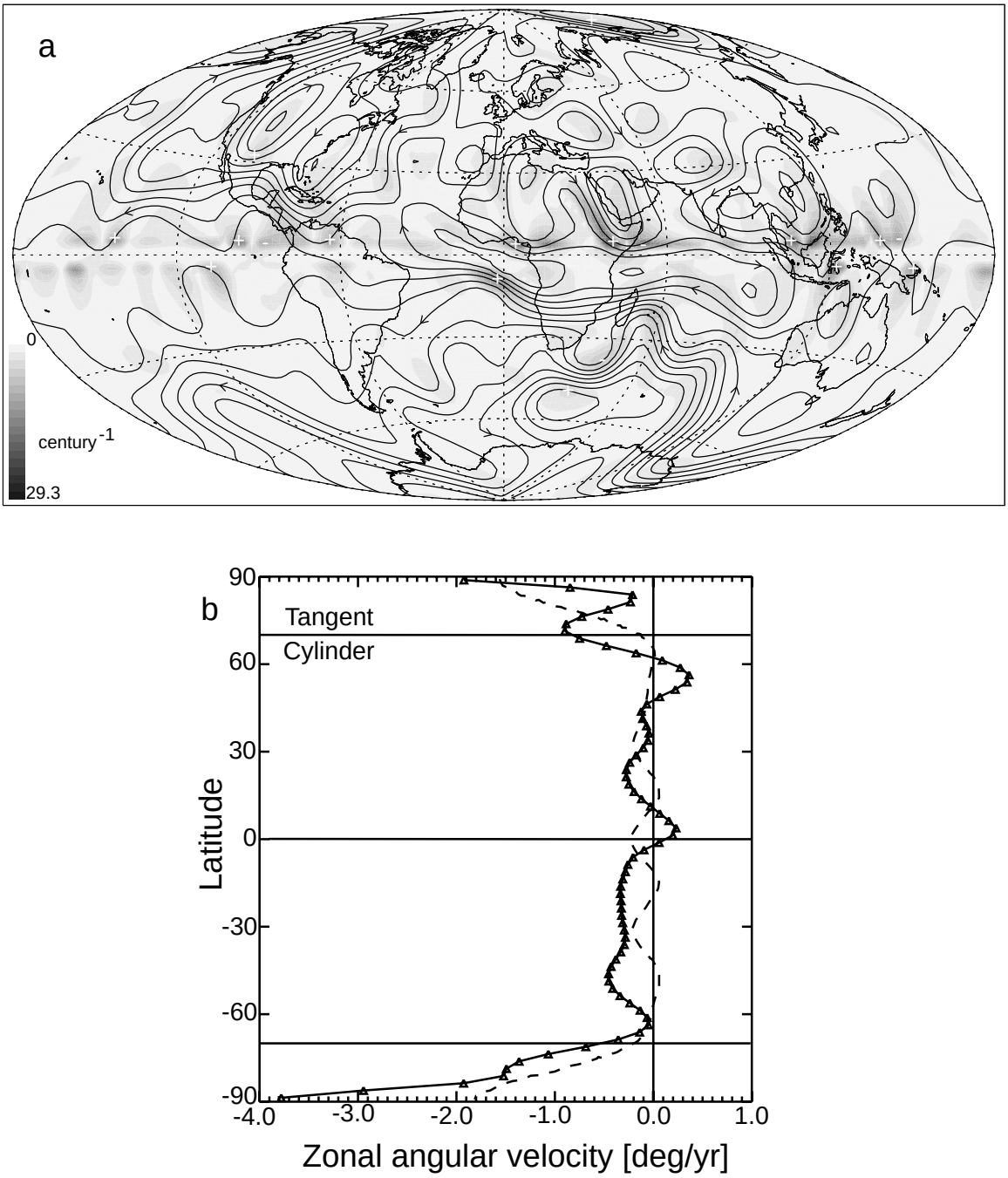

Figure 3.7: Resolution test. Flow map (a) and zonal velocity profile (b) beneath the core-mantle boundary for a finer grid case 3 from table 3.1. Contours in (a) are streamlines of the flow, grey scale represents absolute upwelling value, with + and - signs indicate upwelling and downwelling, respectively. The contour interval in (a) is larger by a factor of 2 than in Fig. 3.5a. In (b) the zonal flow of Hulot et al. (2002) is shown by a dashed line for comparison.

3.5b and 3.7b, and also see Table 3.3); the symmetric part of the flow in the resolution test case is about 2 times larger than the anti-symmetric part. Equatorial symmetry in the zonal flow is critical in the interpretation of length of day variations in terms of time dependent core flows (Jault et al., 1988; Jackson et al., 1993), and is also found in numerical dynamo simulations (Christensen et al., 1999). Fig. 3.7b includes the zonal velocity profile obtained by Hulot et al. (2002) for the same data sets.

3.5.4 Comparison between different physical assumptions

Fig. 3.8 shows the solutions for the strong helicity (case 4), weak helicity (case 5) and columnar flow (case 6) cases. Note that the contour intervals vary from one figure to another (see details in caption of Fig. 3.8). Most of the major features are found in the solutions for the different physical assumptions, but there are some case-to-case differences.

The toroidal flow patterns in the tangential geostrophy (case 1, Fig. 3.5a) and the strong helicity (case 4, Fig. 3.8a) are very similar. The main difference between the two cases is in the upwelling pattern. The global upwelling pattern in the strong helicity case is evenly distributed over the core-mantle boundary, whereas in the tangential geostrophy case the largest upwellings appear in the equatorial region, a consequence of the singularity of the tangential geostrophy term at the equator. To illustrate this difference, consider the positive B_r structure below central Africa (see Fig. 1.3a). This structure is stretched to the west, and as a result, a positive secular variation structure appears to its west (below the west coast of central Africa, see Fig. 1.3b), but no significant secular variation structure appears to its east, as would be expected from plain advection. My solutions recover this secular variation monopole by stretching, caused by downwelling centered below the west coast of central Africa. This downwelling is produced by a weak southward flow in the tangential geostrophy case (see Fig. 3.5a), or by a strong clockwise vortex in the strong helicity case (see Fig. 3.8a). In both cases the motion is connected to the global circulation by eastward

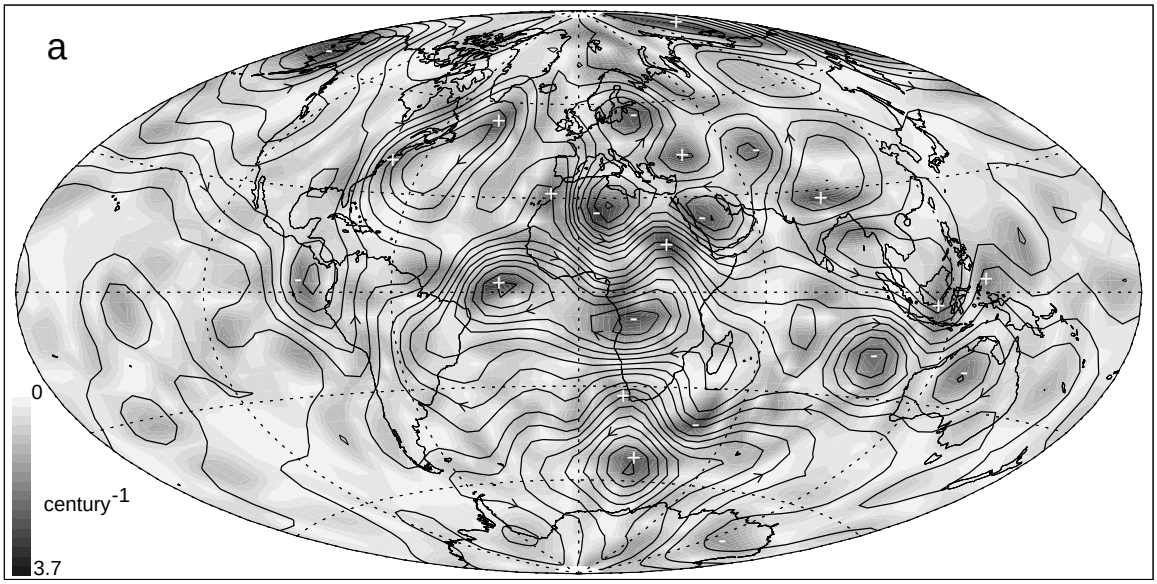

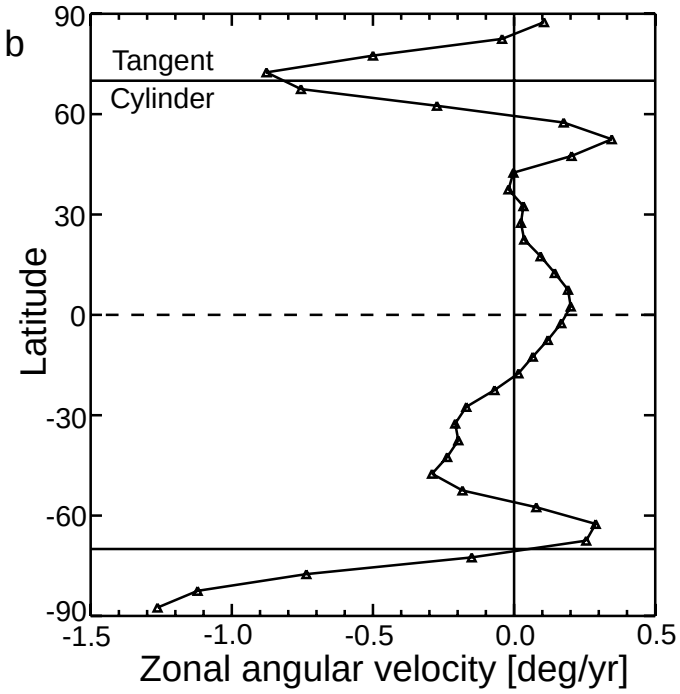

Figure 3.8: Flow maps beneath the core-mantle boundary for the strong helicity (a) case 4, weak helicity (c) case 5 and columnar flow (e) case 6 (all cases from table 3.1). Zonal velocity profiles for the three cases are presented at (b), (d) and (f), respectively. Contours in (a), (c) and (e) are streamlines, grey scale represents absolute upwelling value, + and - signs indicate upwelling and downwelling, respectively. The contour interval in (a) is the same as in Fig. 3.5a, in (c) is smaller by a factor of 1.6 than in Fig. 3.5a, and in (e) is larger by a factor of 1.2 than in Fig. 3.5a.

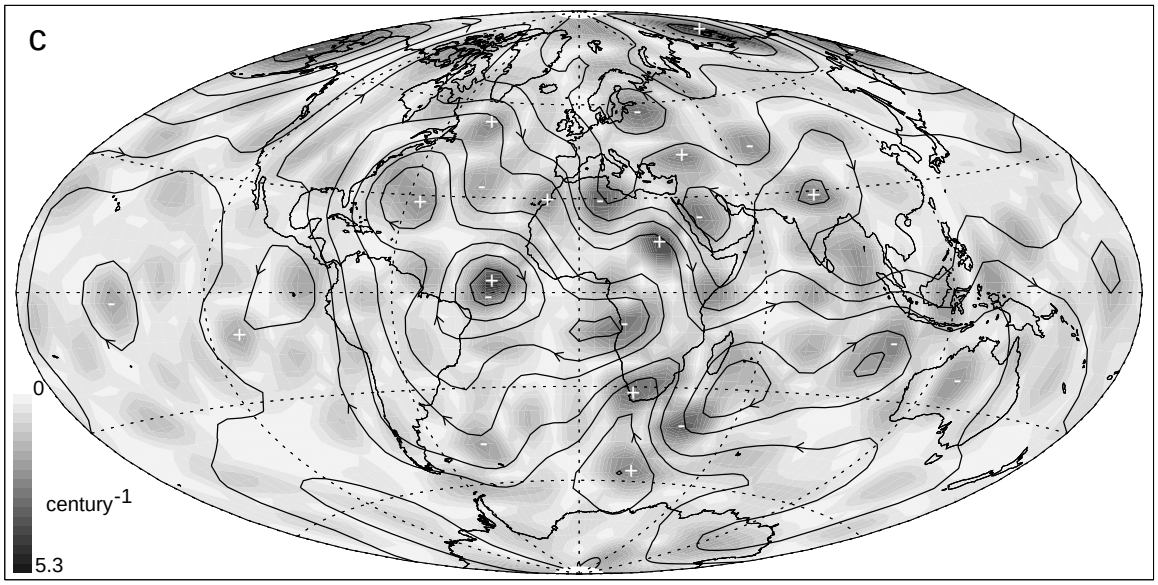

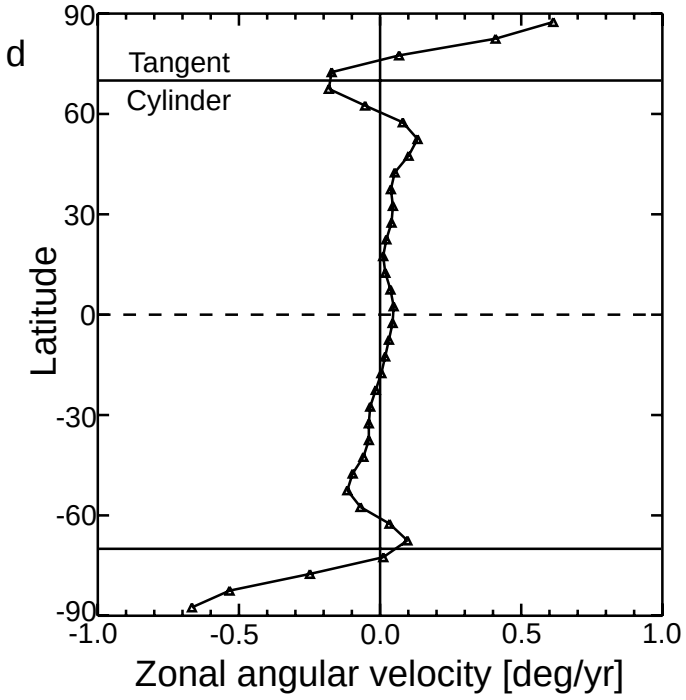

Figure 3.8: Continued

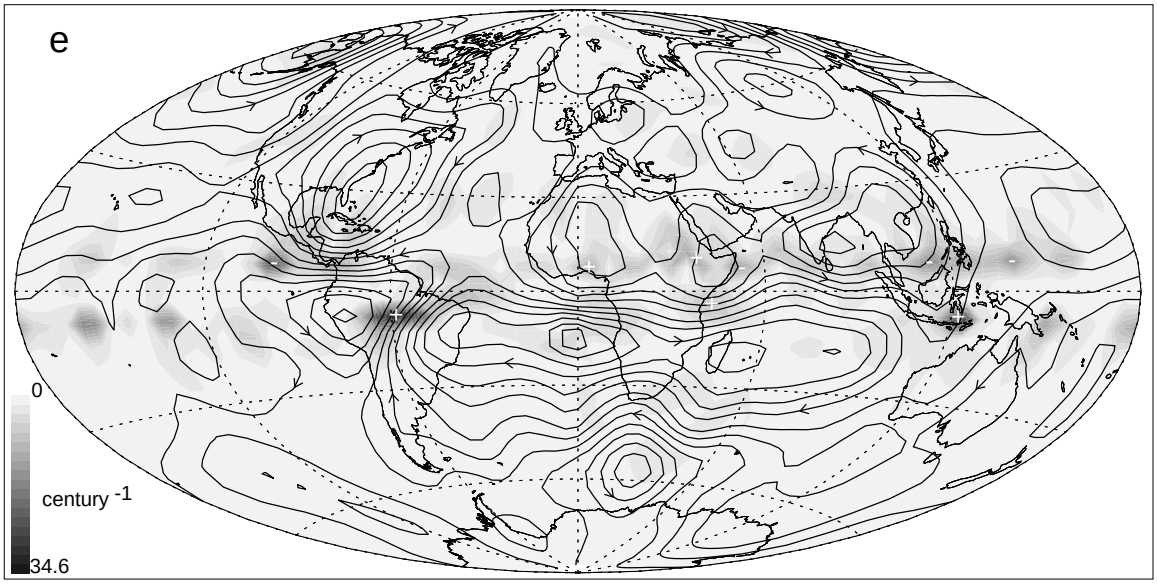

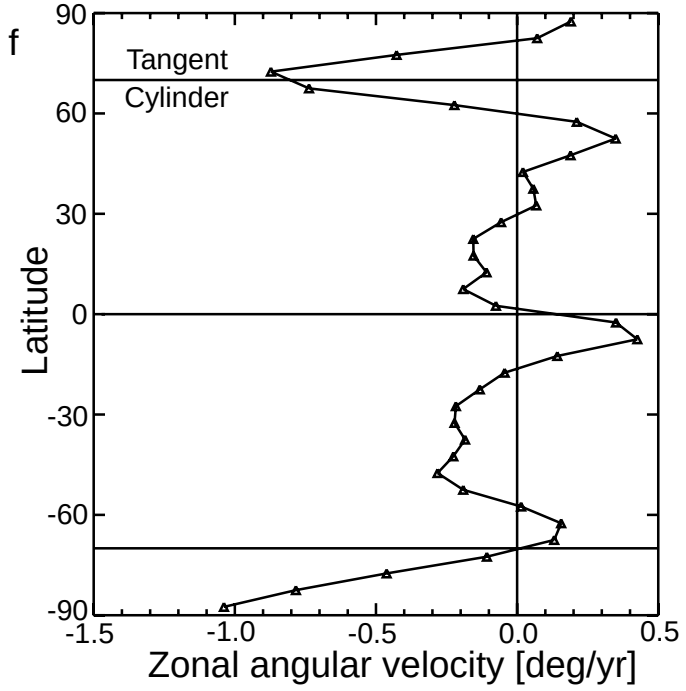

Figure 3.8: Continued

jet along B_r-contours. This eastward flow produces some stretching of the magnetic field without effects of advection.

The flow pattern of the weak helicity (case 5, Fig. 3.8c) has elements in common with the strong helicity case, although the velocity field of the weak helicity case is more strongly damped and has smaller velocities overall (see Table 3.1 for maximum and rms values).

The columnar flow solution (case 6, Fig. 3.8e) is also similar to the tangential geostrophy solution (case 1), with the main difference being that the columnar flow solution is more aligned with the equator. As a result, the zonal velocity in the columnar flow case has larger equatorial amplitudes (eastward at southern hemisphere, westward at northern hemisphere) than the tangential geostrophy case (compare Figs. 3.8f and 3.5b).

The ratio of poloidal to toroidal velocities scales with the coefficient k_0 in the strong and weak helicity cases, and with the coefficient c in the tangential geostrophy and columnar flow cases. In the strong helicity case, the secular variation can be explained by toroidal advection and stretching, whereas in other cases there is also a contribution to the secular variation from poloidal advection.

The ratio of average flow component along B_r-contours to the average flow component perpendicular to the same contours is about 1.2 for all cases (Table 3.3), indicating a significant amount of such flow. Cross equatorial flow occurs least in the columnar flow case and most in the weak helicity case (again, Table 3.3).

Figs. 3.5a, 3.8a, 3.8c and 3.8e show little evidence of non-axisymmetric Taylor columns, i.e. vortices of opposite sign symmetric about the equator. These may be obscured by the axisymmetric flow, or, the scale of such non-axisymmetric Taylor columns of fluid might be very small and "unseen" in the resolution of the data. Another possibility is that the Taylor columns are axisymmetric and can only be seen in the zonal angular velocity profiles (Figs. 3.5b, 3.8b, 3.8d and 3.8f), which do display some equatorial symmetry. The ratio of

the symmetric zonal flow with respect to the equator to the antisymmetric one is given in Table 3.3. Note that the tangential geostrophy and strong helicity cases both contain about equal amounts of zonal symmetric and antisymmetric flow components with respect to the equator, whereas the zonal flow of the weak helicity case is very antisymmetric.

3.5.5 Comparison with previous results

Here I compare the results of my tangential geostrophy case with the results obtained by Hulot et al. (2002) using the same Ørsted and Magsat geomagnetic data. I further discuss some general conceptual differences between my solutions and previous ones, in terms of the differences between my method and previous spectral methods.

My global circulation has some features in common with that obtained by Hulot et al. (2002): The Atlantic hemisphere is more active than the Pacific one, some symmetry in the zonal velocity profile with respect to the equator and similar westward drift in mid-latitudes of the southern hemisphere. However, my solution differs from the solution obtained by Hulot et al. (2002) in several features. My average westward drift is somewhat less than theirs and my zonal flow is actually eastward in places where theirs is westward. Also my solution contains significantly more flow along B_r-contours than Hulot et al. (2002).

Most previous solutions restricted the scale of their flow solution by setting some a-priori constraint on the energy spectrum. My method does not rely on a-priori constraints; instead a solution is provided by diffusion of the streamfunction through the helical flow term. Previous spectral methods minimized "invisible flow", whereas ours allows for such flow where it is required by the helical flow assumption. In my method, the amount of flow along B_r-contours is specified by the amount of helicity assumed, through the value of the parameter k_0. Previous studies found maximal upwelling values of $\sim 2-4$ century^{-1} (e.g. Gire et al., 1986; Gire and LeMouël, 1990; Bloxham and Jackson, 1991). I obtain similar upwelling magnitudes in the strong and weak helicity cases, as well as in the sensitivity

test case (see scales at Figs. 3.6c, 3.8a and 3.8c). However, the singularity in the tangential geostrophy term at the equator yields local stronger upwellings in the equatorial region for the tangential geostrophy case (see scale at Fig. 3.5a).

3.5.6 Specific areas of interest

Here I examine some specific areas of interest from the tangential geostrophy case, which show how the kinematics in my flow solution creates particular structures in the secular variation.

Fig. 3.9a shows the radial magnetic field on the core-mantle boundary at 1980 and 2000 and the full velocity vectors in the region below Madagascar, obtained from the tangential geostrophy case 1. Note the general consistency between the translation of the $B_r = 0$ curve and the velocity vectors. The secular variation in this area can be accounted for by simple advection of B_r by toroidal velocity. The center of negative magnetic field structure shifts from $(43^\circ E, 35^\circ S)$ at 1980 to $(37^\circ E, 28^\circ S)$ at 2000, approximately a 9° translation to the north west in 20 yr. The velocity field at this region includes a jet to the north west with maximum velocity of 68.6 km/yr, which corresponds to translation of about 10° in 20 yr.

Fig. 3.9b shows the radial magnetic field on the core-mantle boundary from the same epoch as Fig. 3.9a, along with the poloidal velocity vectors in the region below Ethiopia, again from case 1. In this region the contours of B_r show a broad ridge structure in 1980 centered at $34^\circ E$. By 2000, this ridge structure has been translated to $28^\circ E$, and also has been sharpened. The secular variation in this area can be accounted for by stretching of magnetic field due to an upwelling. The poloidal velocity indicates the direction in which the stretching operates. Two centers of meridional velocity, which are sources of upwelling and surface divergence due to the tangential geostrophic effect, appear in the solution at $(35^\circ E, 12^\circ N)$ and $(0^\circ E, 5^\circ N)$. Those sources are located on both sides of the

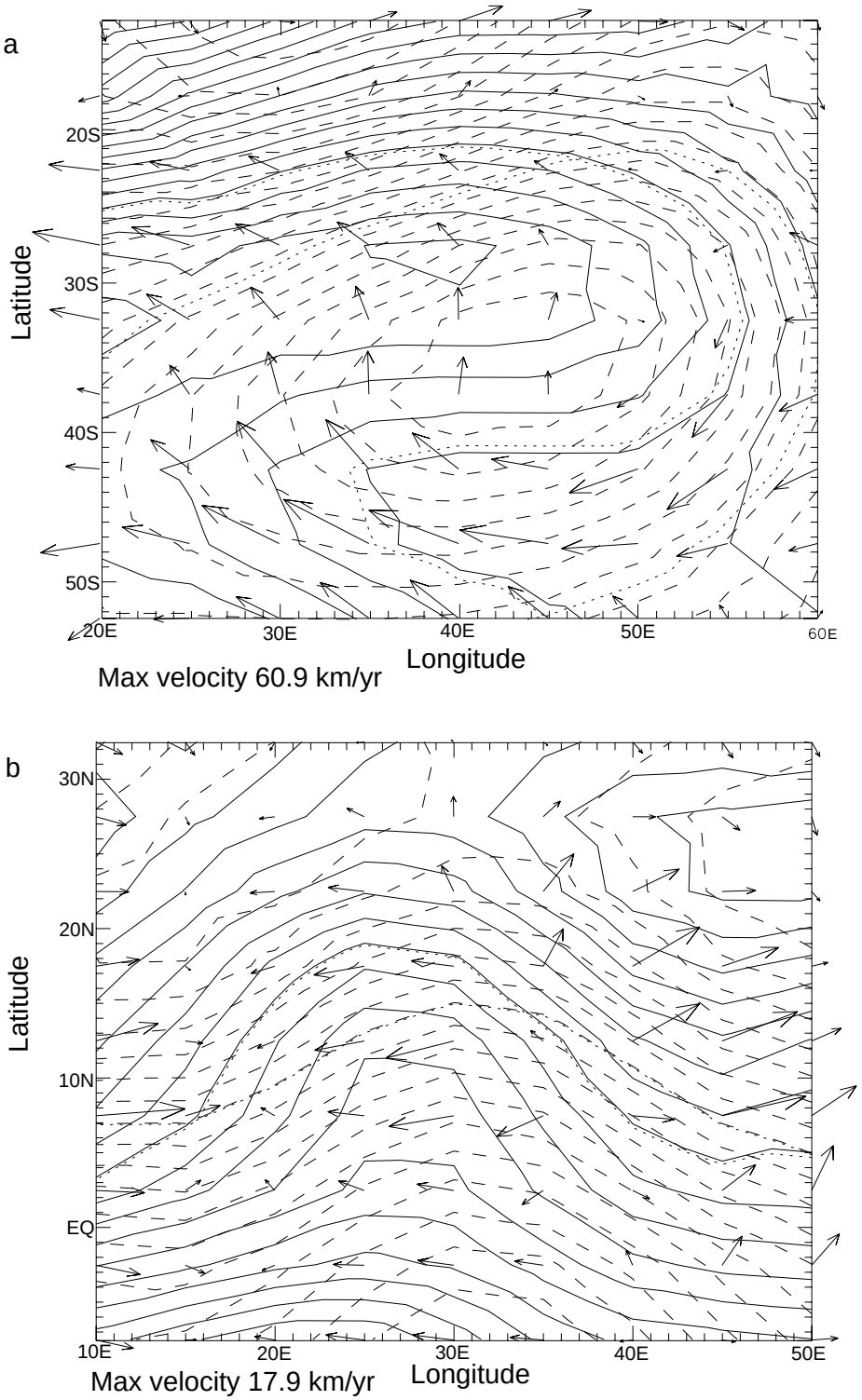

Figure 3.9: Magnetic field at 1980 (dashed lines) and 2000 (solid lines), and velocity vectors (arrows) for specific areas. $B_r = 0$ curves are shown as dotted curves in the two cases. (a) below Madagascar, showing full velocity, and (b) below Ethiopia, showing poloidal velocity.

ridge structure and produce the poloidal velocities and the stretching responsible for the contraction of B_r contours at this region.

3.6 Summary

I have used geomagnetic secular variation data to image the fluid flow below the core-mantle boundary by combining a previously-used assumption for the upwelling, tangential geostrophy, with a new helical flow assumption. The latter introduces streamfunction diffusion in the magnetic induction equation, and allows us to compute the fluid velocity at the top of the core using finite difference methods on a regular grid. My method does not require any a-priori assumption about the energy or lengthscale of the flow. My method simultaneously minimizes the secular variation data residual and guarantees that the resulted flow satisfies the physical assumption everywhere on the grid. I have used the 2000 Ørsted and 1980 Magsat core geomagnetic fields. For this 20 years interval, my main findings are:

- The main flow structures common to all my upwelling models include a large anticlockwise circulation in the southern hemisphere, a clockwise vortex below Bermuda, and a westward flow over most of the southern hemisphere.

- My solutions contain a significant amount of flow along B_r-contours. The ratio of the average velocity component parallel to B_r-contours to the average velocity component perpendicular to the same contours is about 1.2.

- The zonal average westward drift rate in mid-latitudes of the southern hemisphere is in agreement with the traditional $0.2\ ^\circ$/yr value, but the drift is smaller and even eastward at other latitudes.

- The signature of the inner core tangent cylinder is apparent in the zonal velocity profile. Polar vortices are suggested, though not well resolved in my models.

- The large scale flow in the high resolution test is qualitatively similar to the large scale flow seen with coarser resolution, but also shows some substantial differences. For example, in the higher resolution case the ratio of equatorial symmetric to anti-symmetric zonal flow is about 2, whereas this ratio is about 1 with coarser resolution. This difference indicates a need for core flow models with higher spatial resolution.

- In all cases I investigated, the Atlantic hemisphere displays higher flow velocities than the Pacific.

Some of the main features of my results are similar to previous core flows obtained with the same data by Hulot et al. (2002). The results of my tangential geostrophy case contain strong mid-latitude vortices, westward drift sweeping most of the southern hemisphere, flow in the Atlantic hemisphere is more intense than in the Pacific and suggested (though not reliable) strong polar westward vortices. The flows I calculate are characterized by relatively large length scales, despite the dominance of high wavenumber structure in the secular variation. However, my solution differs from previous ones in some important aspects. My solutions contain a significant component of flow along B_r-contours; this component of flow is constrained by the helical flow assumption. Hulot et al. (2002) obtained westward drift in both hemispheres, whereas my solution contains smaller and in some latitudes eastward drift.

Due to the helical flow assumption, the structure of the poloidal flow in my solutions is different from than in previous studies. Near the equator, the tangential geostrophy assumption is dominant, and poloidal flow sources are located in regions of meridional flow. However, far from the equator, the helical flow dominates, and poloidal flow sources coincide with centers of vortices.

Chapter 4

Time-average and time-dependent parts of core flow

4.1 Introduction

The Earth's magnetic field is generated by fluid flow in the Earth's metallic liquid outer core. This process, the geodynamo, has been studied using various approaches, including inversions of the geomagnetic secular variation, self-consistent numerical dynamos, lab experiments, paleomagnetic observations, and core thermal history. In this chapter I use the historical geomagnetic secular variation to image the core flow over a century of time. I separate the time-average and time-dependent parts of the core flow derived this way. I compare the time-average flow with models of core flow driven by lateral density gradients originating in the core and in the mantle. Then I compare the time-dependent part of the flow with observed length-of-day variations, and fit these fluctuations to a model of torsional oscillations in the outer core.

The outline of the chapter is as follows. In section 2 I describe my method of finding core flow just below the core-mantle boundary from geomagnetic secular variation data. In

section 3 I present the results of my inversions using historical secular variation data. In section 4 I apply a thermal wind interpretation to the time-average core flow using mantle tomography and numerical dynamos. In section 5 I use observations of length-of-day variations to test the time-dependent part of my solutions, and I fit a torsional oscillations model to this time-dependency. My main findings are summarized in section 6.

4.2 Core flow inversion

The geomagnetic secular variation has been used to map fluid motion in the outer core, providing images of the geodynamo just below its outer surface. Early analysis of the secular variation inferred that the main core flow is uniform $0.2\,^{\circ}$/yr westward zonal drift (Bullard et al., 1950). More recent analysis of secular variation using the magnetic induction equation in the perfect conducting, frozen-flux limit (Roberts and Scott, 1965) have shown that this simple model is inadequate. It is now known that the zonal core flow varies with latitude and is time-dependent. In addition, core flow includes significant north-south toroidal and poloidal components (Gire et al., 1986; Voorhies, 1986; Jault et al., 1988; Bloxham, 1989; Gire and LeMouël, 1990; Bloxham and Jackson, 1991; Jackson and Bloxham, 1991; Jackson et al., 1993; Jackson, 1997; Pais and Hulot, 2000; Hulot et al., 2002; Amit and Olson, 2004).

Separate interpretations have been applied to the time-average and the time-dependent parts of the flow. The time-average part of the core flow has been proposed to be a result of mantle heterogeneity (thermal, compositional or topographic) affecting core dynamics (Glatzmaier et al., 1999; Olson and Christensen, 2002; Christensen and Olson, 2003). The time-dependent part has been linked to angular momentum exchange between the core and the mantle and length-of-day variations (Jault et al., 1988; Jackson et al., 1993). The time-dependent core flow has been modeled as torsional oscillations in the outer core (Zatman

and Bloxham, 1997; Bloxham et al., 2002).

I wish to stress the conceptual difference between time-average core flow as derived in this chapter and previous steady core flow models. I invert for the core flow at each separate epoch, and then calculate the time-average of the resulting flows. This procedure differs from often-used inversion methods which incorporate steady flow (Gubbins, 1982; Voorhies, 1986; Bloxham, 1992) or a steady flow in an azimuthally drifting reference frame (Voorhies and Backus, 1985; Holme and Whaler, 2001) as *a-priori* constraints.

4.2.1 Inversion method

Fluid motion just below the core-mantle boundary can be inferred from geomagnetic secular variation by assuming the magnetic field acts like a tracer in the fluid. Like previous studies of core flow, I assume frozen magnetic flux, in which the diffusion of magnetic field is neglected in comparison with the advection of magnetic field by the flow (Roberts and Scott, 1965). The frozen flux hypothesis is assumed valid because the magnetic diffusion time-scale, $\tau_\lambda = L^2/\lambda \sim 30,000$ yr, is much longer than the advection time-scale, $\tau_u = L/U \sim 60$ yr, where L, U and λ are the typical length-scale, velocity and magnetic diffusivity for the Earth's core (Amit and Olson, 2004).

The radial component of the frozen flux magnetic induction equation just below the core-mantle boundary is

$$\frac{\partial B_r}{\partial t} + \vec{u}_h \cdot \nabla B_r + B_r \nabla_h \cdot \vec{u}_h = 0 \tag{4.1}$$

where B_r is the radial component of the magnetic field, t is time and $\vec{u}_h$ is the fluid velocity tangent to the spherical core-mantle boundary. Maps of B_r and its time derivative $\partial B_r/\partial t$ at the core-mantle boundary, together with some assumption for the tangential divergence of the flow, allow for inversion of the tangential fluid velocity $\vec{u}_h$ using (4.1).

The tangential velocity can be decomposed into a toroidal (non-divergent) component

expressed in terms of a streamfunction Ψ and a poloidal (divergent) component expressed in terms of a scalar potential Φ as follows:

$$\vec{u}_h = \vec{u}_{tor} + \vec{u}_{pol} = \nabla \times \Psi \hat{r} + \nabla_h \Phi \tag{4.2}$$

where $\hat{r}$ is a unit radial vector and $\nabla_h = \nabla - \partial/\partial r$ and (r, θ, ϕ) are the radial, co-latitudinal and longitudinal spherical coordinates. Substitution of (4.2) into (4.1) gives

$$\frac{\partial B_r}{\partial t} + \frac{1}{R^2 sin\theta}\left(\frac{\partial \Psi}{\partial \phi}\frac{\partial B_r}{\partial \theta} - \frac{\partial \Psi}{\partial \theta}\frac{\partial B_r}{\partial \phi}\right) + \frac{1}{R^2}\left(\frac{\partial \Phi}{\partial \theta}\frac{\partial B_r}{\partial \theta} + \frac{1}{sin^2\theta}\frac{\partial \Phi}{\partial \phi}\frac{\partial B_r}{\partial \phi}\right) + B_r \nabla_h^2 \Phi = 0 \tag{4.3}$$

where $\nabla_h^2 = \nabla^2 - \frac{1}{r^2}\frac{\partial}{\partial r}(r^2 \frac{\partial}{\partial r})$ and R is the core radius.

Amit and Olson (2004) proposed an expression for the tangential divergence of velocity that incorporates the previously-used tangential geostrophy assumption (LeMouël, 1984; Gire and LeMouël, 1990; Jackson, 1997; Hulot et al., 2002) and a helical flow assumption,

$$\nabla_h \cdot \vec{u}_h = \mp k\zeta + \frac{\tan\theta}{R} u_\theta \tag{4.4}$$

The first term on the right hand side of (5.13) is helical flow. It assumes that the tangential divergence is correlated with the radial vorticity ζ, the minus sign for the northern hemisphere and the plus sign for the southern hemisphere. The second term on the right hand side of (5.13) is tangential geostrophy. Substitution of (4.2) into (5.13) yields

$$\nabla_h^2 \Phi = \mp k \nabla_h^2 \Psi + \frac{tan\theta}{R^2}\left(\frac{1}{sin\theta}\frac{\partial \Psi}{\partial \phi} + \frac{\partial \Phi}{\partial \theta}\right) \tag{4.5}$$

The non-dimensional parameter k is unknown in the core. Simple analytical models of rotational flows and results from numerical dynamos suggest that $0.5 > k > 0.05$ (Amit and Olson, 2004). Here I use $k = 0.1$, as in the main case of Amit and Olson (2004).

I solve (4.3) and (5.14) simultaneously in an iterative way to obtain the potentials Ψ and Φ over the core-mantle boundary. I use a second order, central finite difference method on a regular $2.5^\circ \times 2.5^\circ$ spherical grid with radius R. Equation (5.14) is singular at the equator, and special treatment is required there. First, I calculate the θ-derivatives of Ψ at

the equator by assuming that the equator is a streamline, and the θ-derivatives of Φ at the equator by assuming that the equator is a mirror for Φ. Second, I replace the $\tan\theta$ term in (5.14) by $-2\sin(2(\theta-\pi/2))\cdot\exp(-(\theta-\pi/2)^2)$, which is finite at the equator. These approximations minimize flow across the equator and result in a globally balanced upwelling distribution, as opposed to concentrated upwelling features at the equatorial region found in many previous core flow solutions. This treatment corresponds to a non-geostrophic belt near the equator which is plausible because the Coriolis force vanishes there. Previous studies have postulated the existence of such a belt and discussed its possible width and geometry (Backus and LeMouël, 1986; Chulliat and Hulot, 2000; Pais et al., 2004).

4.2.2 Limitations of core flow inversions

Core flow inversions from geomagnetic secular variation data suffer from several limitations, leading to uncertainties in inferred core flows. First, the secular variation data is truncated at spherical harmonic degree $12-14$ to remove the effect of crustal magnetization. This truncation might remove a significant core signal, and its influence on the inverted flows is unknown. Second, most studies assume frozen flux, so the unmodeled effects of magnetic diffusion are sources of errors in inverted flows. Third, the physical assumption for the tangential divergence of the core flow is rather ad-hoc. A variety of physical assumptions have been used in the past, such as pure toroidal flow (Whaler, 1980), steady flow (Voorhies, 1986) and tangential geostrophy (LeMouël, 1984). Those assumptions reduce but do not remove non-uniqueness from the inverse problem. This non-uniqueness is of great concern; there is some "invisible" component to the flow which does not generate secular variation of its own (Backus, 1968; Backus and LeMouël, 1986). In tangential geostrophy the non-uniqueness is confined to ambiguous patches and is therefore more restricted than in pure toroidal flow (Chulliat and Hulot, 2000), but still the problem remains. Core flow models which assumed steady flow are advantageous for their

simplicity and were found compatible with the gross secular variation, but could not resolve adequately the fine scale or abrupt secular variation (Bloxham, 1992; Holme and Whaler, 2001). Finally, different numerical techniques and regularization conditions may affect the resulted core flows as well. Cautious interpretation of the results is necessary in view of these uncertainties. Even so, the remaining uncertainties raise the question whether the inverted core flows give an accurate picture of the actual core flow, in terms of pattern and magnitude. The present study is subject to all of the above limitations, except one. In my method non-uniqueness is removed from the inverse problem by adding helical flow (Amit and Olson, 2004).

4.3 Core flows between 1895-1985

I solve (4.3) and (5.14) for the core flow using the time-dependent model of Bloxham and Jackson (1992) for the radial component of the magnetic field on the core-mantle boundary $B_r(\theta, \phi, t)$ truncated at spherical harmonic degree 14. This field model was constructed by fitting the magnetic observatory annual means and Magsat satellite data using spherical harmonics for spatial representation and cubic B-splines for the temporal representation. I concentrate on the time interval 1890-1990. I compute the secular variation as the central time difference between two epochs 10 years apart. Accordingly, my core flows correspond to 5-years intervals between 1895-1985. Fig. 4.1 shows examples of the geomagnetic data used in this study.

Fig. 4.2 shows core flows for epochs 1900, 1925, 1950, and 1975. Three flow structures are common to all of these snapshots. First, a large anti-cyclonic vortex at mid and high latitudes of the southern hemisphere is centered beneath the southern Atlantic Ocean. This structure drifts slowly westward with time. In 1900 it was centered near $[50E, 45S]$ (Fig. 4.2a) whereas in 1975 its center moved to near $[15E, 55S]$ (Fig. 4.2d). In 1925, 1950,

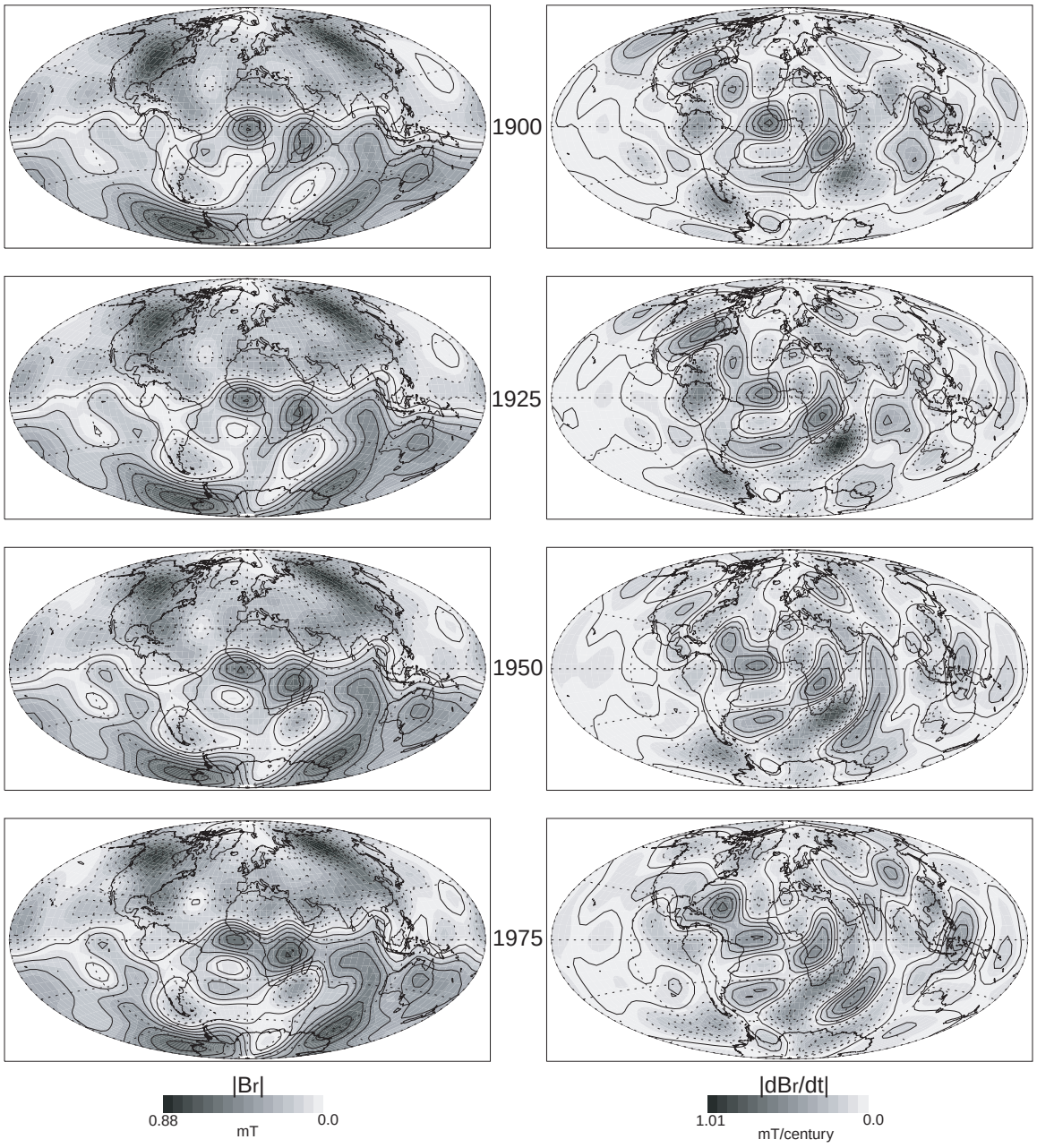

Figure 4.1: Radial magnetic field and secular variation on the core-mantle boundary at 1900, 1925, 1950 and 1975 from core field model of Bloxham and Jackson (1992). Grey scale represents absolute values, solid lines are positive, dotted lines are negative. The secular variation is the central difference between magnetic field snapshots 10 years apart.

and 1975 this structure covers most of the southern hemisphere, extending between $170W$ and $130E$ and from near $20S$ to the South Pole. Second, an intense jet is located beneath the Atlantic southern hemisphere, and forms the northern limb of the vortex. During most epochs its peak intensity is found beneath Southern Africa and beneath mid-latitudes of the Indian and Atlantic Oceans (Fig. 4.2). Third, an anti-cyclonic vortex is centered beneath the east coast of North America (Fig. 4.2). Its position, shape and intensity vary with time. A cyclonic vortex beneath Euro-Asia is also evident in Figs. 4.2a, 4.2b, and 4.2c, but it appears even more time-dependent than the vortex beneath North America.

Table 4.1 summarizes the magnitudes of the core flows in the snapshot images. Rms core velocities range between $11.4 - 14.8$ km/yr, with peak velocities ranging between $82.6 - 153.9$ km/yr. For typical length-scale of $L = 1000$ km and magnetic diffusivity of $\lambda = 1$ m^2/s, these rms velocities correspond to a magnetic Reynolds number range of $Rm = 360 - 470$. Toroidal motions dominate over poloidal motions. For example, the ratio of rms zonal azimuthal transport (due to toroidal motions only) to rms zonal meridional transport (due to poloidal motions only) varies between 5.4 and 13.4 over the study period.

Some of the core flow structures in Fig. 4.2 have been seen in previous studies. The westward jet below southern Africa is present in several previous core flow maps (Bloxham, 1989; Gire and LeMouël, 1990). The large southern hemisphere vortex was found by Jackson et al. (1993). Some important differences between my core flows and previous studies are worth noting. First, my core flows contain a significant amount of field-aligned motion, i.e. motion parallel to B_r-contours. This flow component does not generate secular variation by toroidal advection, but it is coupled to upwelling and downwelling which disperse and concentrate the magnetic field respectively. The rms ratio between the field-aligned component of the flow to the component of the flow perpendicular to B_r contours is ~ 1.2. Field-aligned flow was previously suggested from numerical dynamos and magnetic

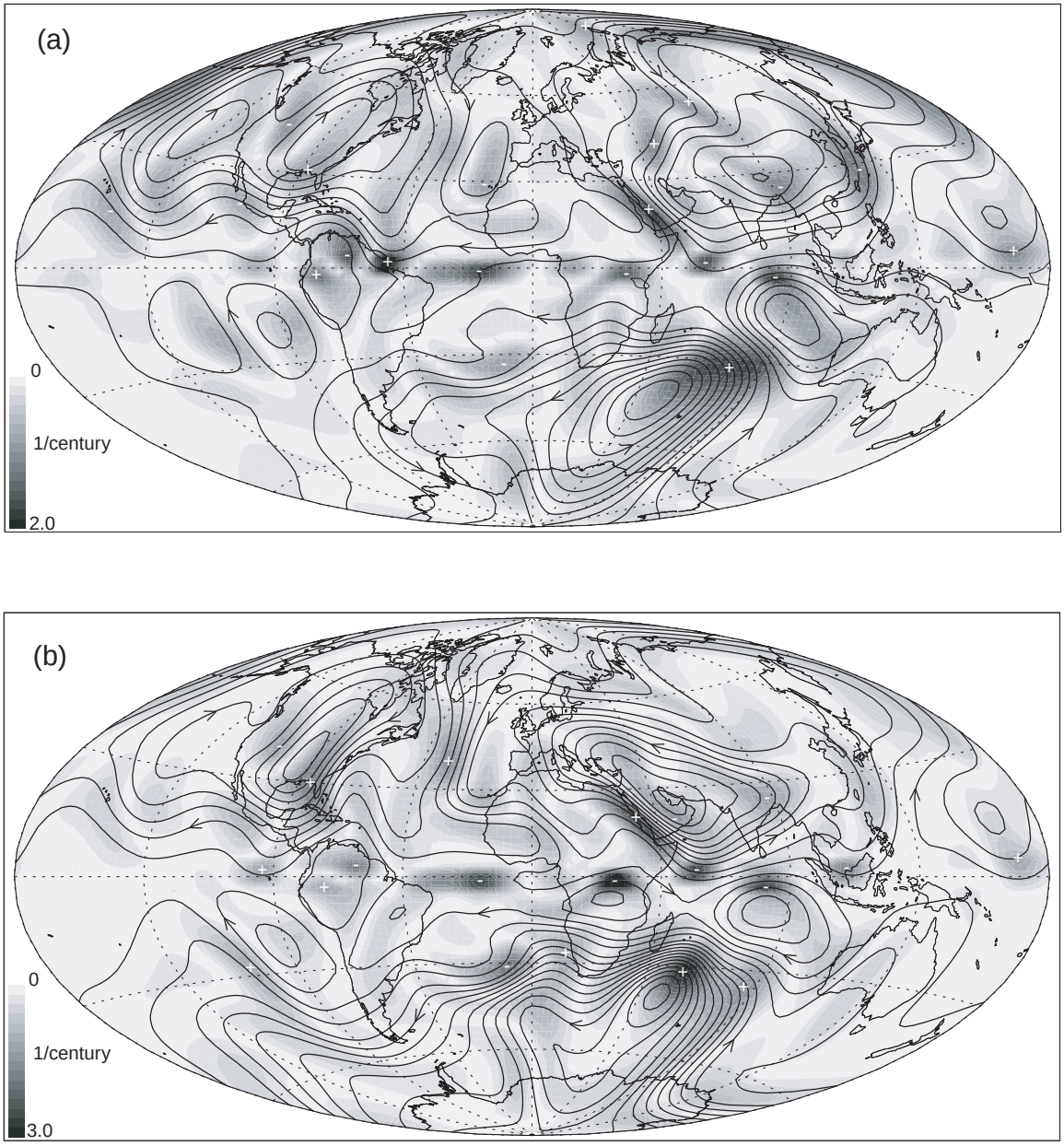

Figure 4.2: Core flow below the core-mantle boundary for the years 1900 (a), 1925 (b), 1950 (c) and 1975 (d). Contours are streamlines of the toroidal flow; grey scale represents absolute upwelling value with + and - signs indicating upwelling and downwelling, respectively.

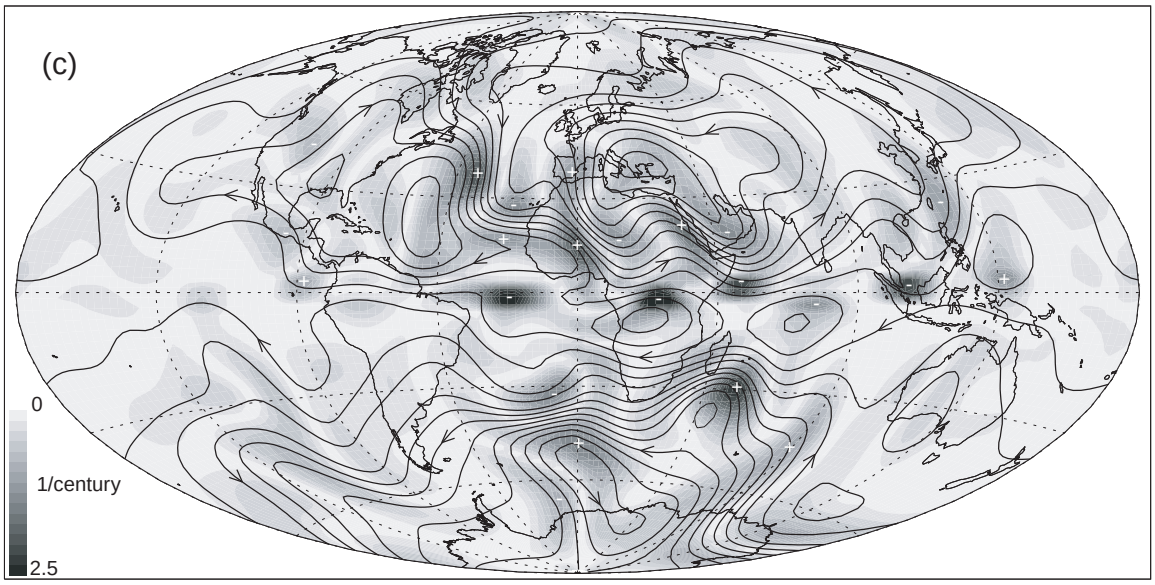

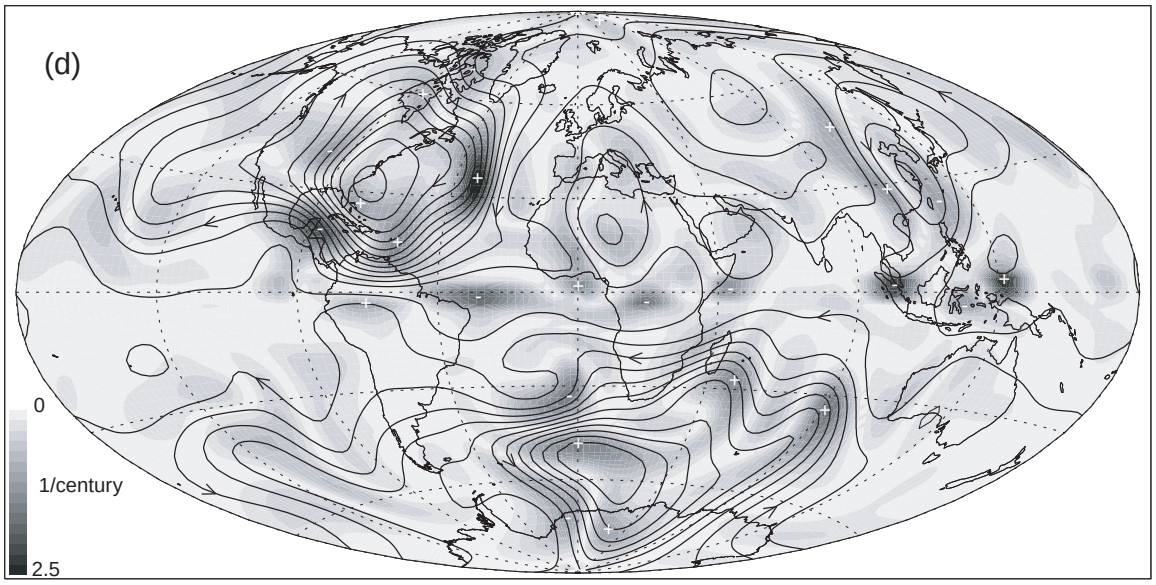

Figure 4.2: Continued

field observations. Olson et al. (1999) found that vortices coincide with intense magnetic flux bundles in 3D self-consistent numerical dynamos, i.e. the flow there is field-aligned. Jackson (2003) noticed the existence of matching pairs of intense magnetic flux with opposite signs on different sides of the equator in magnetic field models obtained from Magsat (1980) and Ørsted (2000) satellites. He postulated that those pairs are evidence for columnar flow. According to this interpretation, that flow at the regions of those flux bundles is parallel to B_r-contours. Second, the relationship between toroidal and poloidal motions is different in my solutions compared to previous solutions. In places where tangential geostrophy dominates, upwelling coincides with equatorward motion and downwelling coincides with poleward motion. However, in places where helical flow dominates, upwelling coincides with anticyclonic motion and downwelling coincides with cyclonic motion.

4.4 Time-average core flow

Fig. 4.3a shows the time-average core flow map for the period 1895-1985 constructed by averaging the potentials Ψ and Φ over the 19 epochs. The main features in the time-average core flow include the same structures noted in the snapshots: A large anti-cyclonic vortex centered near $[20E, 60S]$ in the southern hemisphere, an anti-cyclonic vortex below North America centered near $[90W, 40N]$, and a westward jet below the mid-latitudes of the southern hemisphere with peak intensity below Madagascar. Note that the Atlantic hemisphere is more active overall than the Pacific hemisphere. The rms and maximum absolute velocities of the time-average core flow are smaller than the velocities at individual snapshots (Table 1), indicating that the time-average core flow has larger-scale and lower kinetic energy than individual snapshots.

Fig. 4.3b shows the time-average zonal angular velocity profile for the time interval 1895-1985. Fig. 4.4 shows the zonal azimuthal velocity (a), meridional velocity (b),

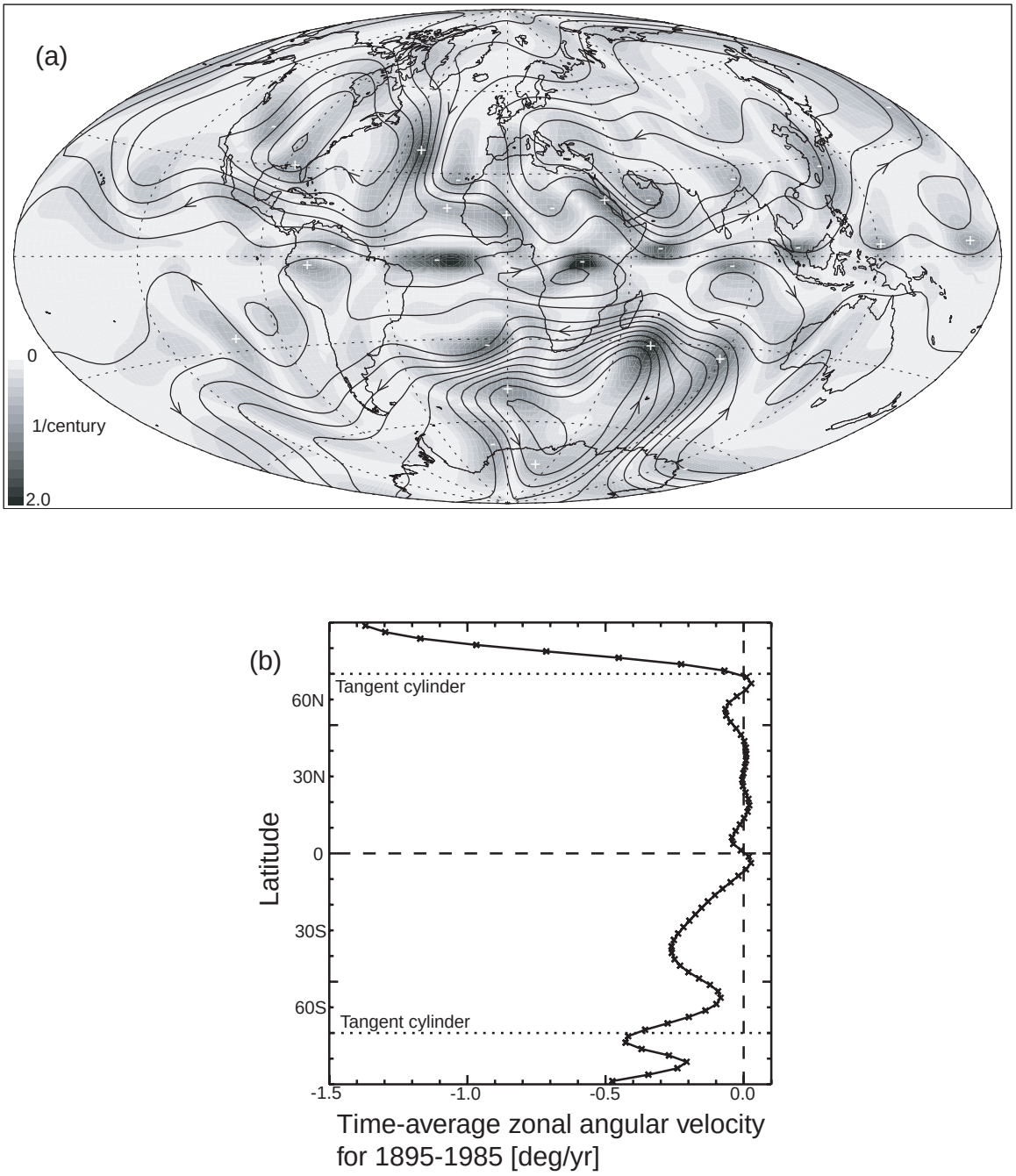

Figure 4.3: Time-average core flow for 1895-1985, and time-average zonal angular velocity for the same time period. Contours in (a) are streamlines of the toroidal flow; grey scale represents absolute upwelling value with + and - signs indicating upwelling and downwelling, respectively.

and tangential divergence (c) for the same time, and the non-dipolar magnetic flux intensity of the time-average magnetic field between 1895-1985 (d). The net divergence in the time-average flow as well as in the individual snapshot flows is practically zero within the discretization error. As seen in Fig. 4.3b, the zonal time-average angular velocity is noticeably asymmetric with respect to the equator. At some latitudes it exceeds the traditional $0.2\ ^\circ$/yr westward drift estimate, particularly in the southern hemisphere, although its rms value is only $0.1\ ^\circ$/yr. In the northern hemisphere the time-average zonal core flow is nearly zero. The largest zonal angular velocities in Fig. 4.3b are in westward polar vortices. The northern polar vortex reaches an angular velocity of $1.4\ ^\circ$/yr, more than 10 times than the maximal zonal angular velocity at low and mid-latitudes of the northern hemisphere. The southern polar vortex reaches only $0.5\ ^\circ$/yr, but it still contains larger angular velocities than elsewhere in the southern hemisphere. I note that equatorially-asymmetric zonal flow outside the tangent cylinder and large symmetric westward polar vortices were found previously by Pais and Hulot (2000) in their time-average zonal core flow.

Zonal azimuthal velocities are correlated/anticorrelated with zonal meridional velocities in the southern/northern hemispheres, respectively, as expected for helical flow. For example, in the northern hemisphere an upwelling is associated with a clockwise vortex in accord with the helical flow assumption, yielding northward (negative) poloidal flow and eastward (positive) toroidal flow on the northern part of the vortex. Zonal meridional velocities inside the tangent cylinder are equatorward (Fig. 4.4b), as expected from upwelling (Fig. 4.4c) below westward polar vortices (Figs. 4.3b and 4.4a) in helical flow.

The time-average zonal divergence (Fig. 4.4c) is anticorrelated with time-average zonal intensity of the non-dipolar normal magnetic flux (Fig. 4.4d). More specifically, the equatorial intense normal polarity flux patches discussed by Jackson (2003) in Fig. 4.4d correlate with convergence at the equator (Figs. 4.3a and 4.4c), and the Southern Atlantic magnetic field anomaly correlates with mid-latitude divergence in the southern hemisphere. These

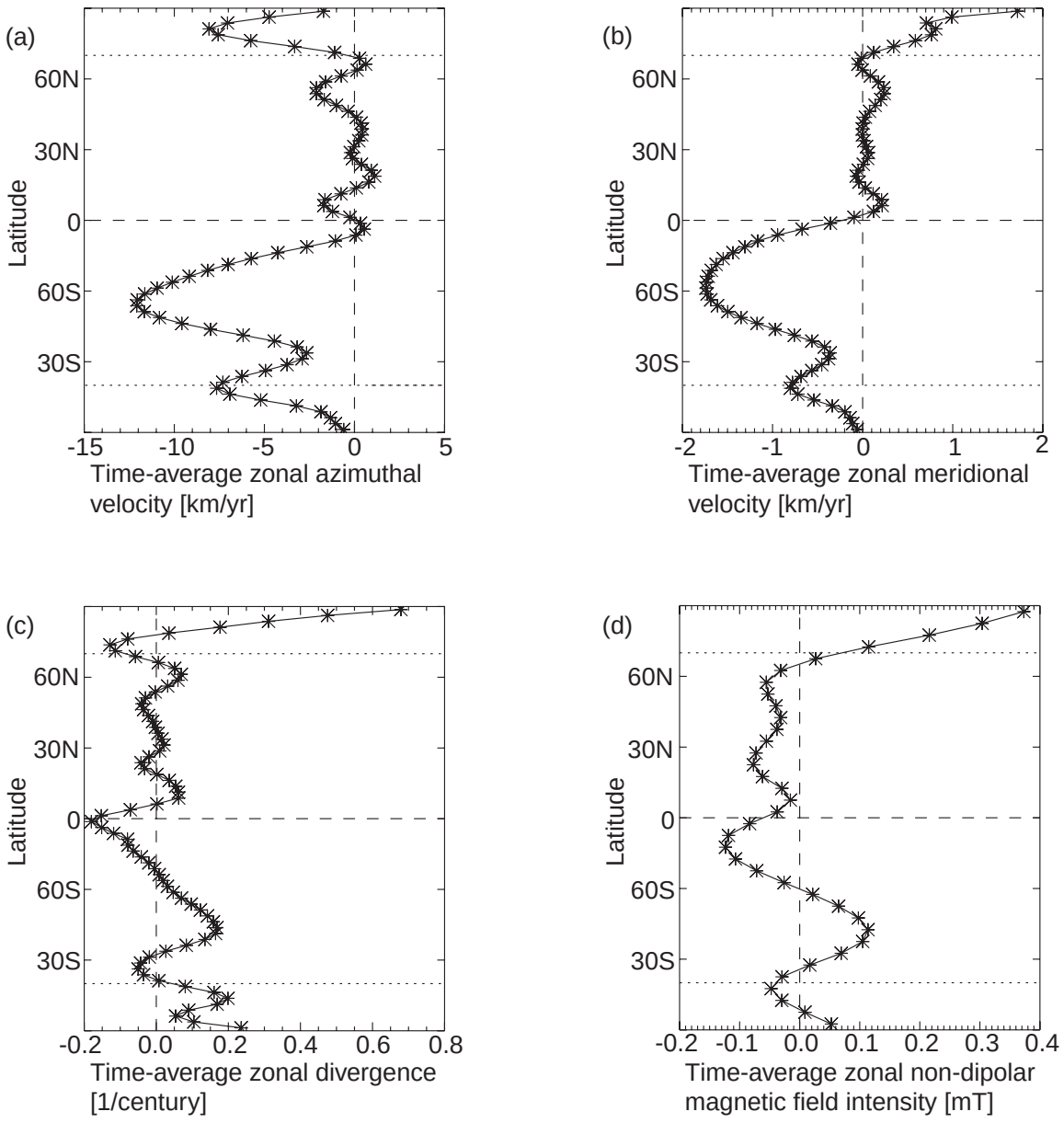

Figure 4.4: Time-average zonal azimuthal velocity (a), meridional velocity (b), and divergence (c) of the core flow and non-dipolar magnetic flux intensity (d), all for 1895-1985.

correlations are consistent with frozen-flux behavior, where magnetic field is concentrated by downwelling and dispersed by upwelling, and suggest that the meridional circulation perturbs the time-average magnetic field from an axisymmetric dipole pattern.

4.4.1 Thermal wind in the core

Many authors have proposed that lower mantle heterogeneity may control some of the fluid motion in the outer core (Gubbins and Richards, 1986; Bloxham and Jackson, 1990; Zhang and Gubbins, 1992; Glatzmaier et al., 1999; Olson and Christensen, 2002; Christensen and Olson, 2003). One specific proposal is that large-scale core flow, especially the zonal azimuthal part of core flow, is a thermal wind driven by lateral density gradients induced by thermal coupling to the lower mantle (Bloxham and Jackson, 1990; Zhang and Gubbins, 1992; Christensen and Olson, 2003). To test this hypothesis, I analyze the thermal wind equation in spherical coordinates for a thick rotating fluid shell using my core flow and models of mantle- and core-produced density heterogeneity. For simplicity, I ignore the magnetic Lorentz force.

The vorticity equation for an incompressible, steady, inviscid, rotating, non-magnetic fluid is given by Pedlosky (1987),

$$(2\vec{\Omega} \cdot \nabla)\vec{u} = -\frac{\nabla\rho \times \nabla p}{\rho^2} \tag{4.6}$$

where $\vec{\Omega}$ is the rotation vector, $\vec{u}$ is fluid velocity, ρ is density and p is pressure. Assuming hydrostatic pressure,

$$\nabla p = -\rho g \hat{r} \tag{4.7}$$

where g is the gravitational acceleration, (4.6) becomes

$$(2\vec{\Omega} \cdot \nabla)\vec{u} = \frac{g}{\rho}(\nabla\rho \times \hat{r}) \tag{4.8}$$

The azimuthal component of (4.8) just below the core-mantle boundary $(r = R)$ is

$$\frac{\partial u_\phi}{\partial \theta} - R\cot\theta\frac{\partial u_\phi}{\partial r} = \frac{g_0}{2\Omega\rho_0}\frac{1}{\sin\theta}\frac{\partial \rho}{\partial \theta} \tag{4.9}$$

where ρ_0 and g_0 are the density and gravitational acceleration at the core-mantle boundary, respectively.

In a thin spherical shell the first term on the left hand side of (4.9) is negligible with respect to the second term, yielding the form of the thermal wind equation commonly used for the atmosphere and the ocean (e.g. Holton, 1992; Andrews, 2000). In this approximation the meridional density gradient balances radial velocity shear. In the outer core, however, I expect that tangential and radial length-scales are comparable, and both terms on the left hand side of (4.9) should be considered. The meridional shear $\partial u_\phi/\partial\theta$ can be calculated from my inverted core flow, but I need an independent way to estimate the radial shear $\partial u_\phi/\partial r$ in the core.

Inversions of the horizontal component of the magnetic induction equation using measurements of changes in the horizontal component of the magnetic field on the core-mantle boundary suggest that the vertical shear in the tangential velocity at the top of the core is proportional to the tangential velocity there (Lloyd and Gubbins, 1990; Jackson and Bloxham, 1991). This argument is equivalent to assuming that the surface core flow correlates with deep core flow. Jackson and Bloxham (1991) have proposed that the length-scale of the vertical shear is one half the radius of the core, i.e.

$$\frac{\partial \vec{u}_h}{\partial r} \simeq 2\frac{\vec{u}_h}{R} \tag{4.10}$$

Adopting this assumption, (4.9) becomes

$$\frac{\partial}{\partial \theta}\left(\frac{u_\phi}{\sin^2\theta}\right) \simeq \frac{g_0}{2\Omega\rho_0}\frac{1}{\sin^3\theta}\frac{\partial \rho}{\partial \theta} \tag{4.11}$$

4.4.2 Thermal coupling with the mantle

Possible mechanisms for core-mantle coupling include thermal, compositional and topographic (Hide, 1967; Gubbins and Richards, 1986; Bloxham and Gubbins, 1987; Loper and Lay, 1995; Schubert et al., 2001). Simple thermal core-mantle coupling assumes that the temperature anomalies at the lower mantle are anticorrelated with the density anomalies at the top of the core (Bloxham and Gubbins, 1987; Bloxham and Jackson, 1990). A second assumption that is often made is that temperature anomalies are anti-correlated to seismic shear velocity anomalies in the lower mantle (Forte and Mitrovica, 2001).

To model thermal coupling with the mantle, I assume density anomalies at the top of the core are proportional to seismic shear velocity anomalies in the lower mantle as follows:

$$\frac{1}{\rho}\frac{\partial \rho}{\partial \theta}|_{core} = \frac{C}{v_s}\frac{\partial v_s}{\partial \theta}|_{mantle} \tag{4.12}$$

Equation (4.12) involves several assumptions. First, the sign of C depends on the type of core-mantle coupling (Olson and Christensen, 2002). If thermal core-mantle coupling prevails, I expect $C > 0$, i.e., a positive mantle seismic velocity anomaly produces a positive core density anomaly. If compositional coupling is dominant, I expect $C < 0$, i.e., a positive velocity anomaly produces a negative density anomaly. Second, the relationship between seismic shear velocity to temperature in the lower mantle is currently under debate. For example, a recent study which separated mantle seismic velocity heterogeneity into thermal and chemical contributions argues that most of the buoyancy in the lower mantle is dominated by chemical variations, and the temperature heterogeneity is very different from the seismic velocity heterogeneity there (Trampert et al., 2004).

Figs. 4.5a and 4.5b show maps of the lower mantle seismic tomography of Li and Romanowicz (1996) and Masters et al. (1996), hereafter referred to as LR and MJLB, respectively. Both Figs. 4.5a and 4.5b were obtained by depth-averaging seismic shear velocity anomalies in the lower mantle from a depth of 2500 km to the core-mantle boundary.

The large-scale features common to both models include (1) mid-latitudes of the northern hemisphere are dominated by positive anomalies, whereas low and mid-latitudes of the southern hemisphere are dominated by negative anomalies; (2) large negative anomalies below Africa and the Pacific; and (3) large positive anomalies below north America, central Asia and Antarctica. The two tomography models differ in some smaller-scale features, which are not important here. Fig. 4.5c shows the zonal profiles of the seismic shear velocity anomalies. Note that the typical wavelength is larger in the MJLB model, and the magnitude is larger at the LR model. I use these models to calculate $\partial v_s/\partial\theta$ and its zonal average. Equation (4.12) is then used to connect $\partial\rho/\partial\theta$ at the top of the core with $\partial v_s/\partial\theta$ at the bottom of the mantle. Using $\partial\rho/\partial\theta$ at the top of the core derived this way, I then solve (4.11) for the core azimuthal flow u_ϕ driven by the mantle.

4.4.3 Time-average core flow from numerical dynamos

In addition to a mantle origin, the time-average flow shown in Fig. 4.3 may also have an origin in the core's own dynamics. Convection in the core results in large-scale lateral density gradients, a consequence of the spherical shell geometry and the constraints of Earth's rotation (Olson et al., 1999). A recent study of numerical dynamos with homogeneous core-mantle boundary conditions shows that thermal convection results in a large-scale thermal wind flow, with a predictable pattern and an amplitude that depends only on the buoyancy flux and the rotation rate (Aubert, 2005). Aubert (2005) verified that a scaling law for the amplitude of this zonal flow previously proposed by Aurnou et al. (2003) remains valid in the presence of a magnetic field.

I use a 3D, self-consistent numerical dynamo which solves simultaneously the full magnetohydrodynamics equations in a rotating, convecting sphere (Olson et al., 1999). I used the following parameter values: $Ra = 4E5$, $Ek = 7E-4$, $Pr = 1$ and $Pm = 5$, where Ra is the Rayleigh number, Ek is the Ekman number, Pr is the Prandtl number and Pm is the

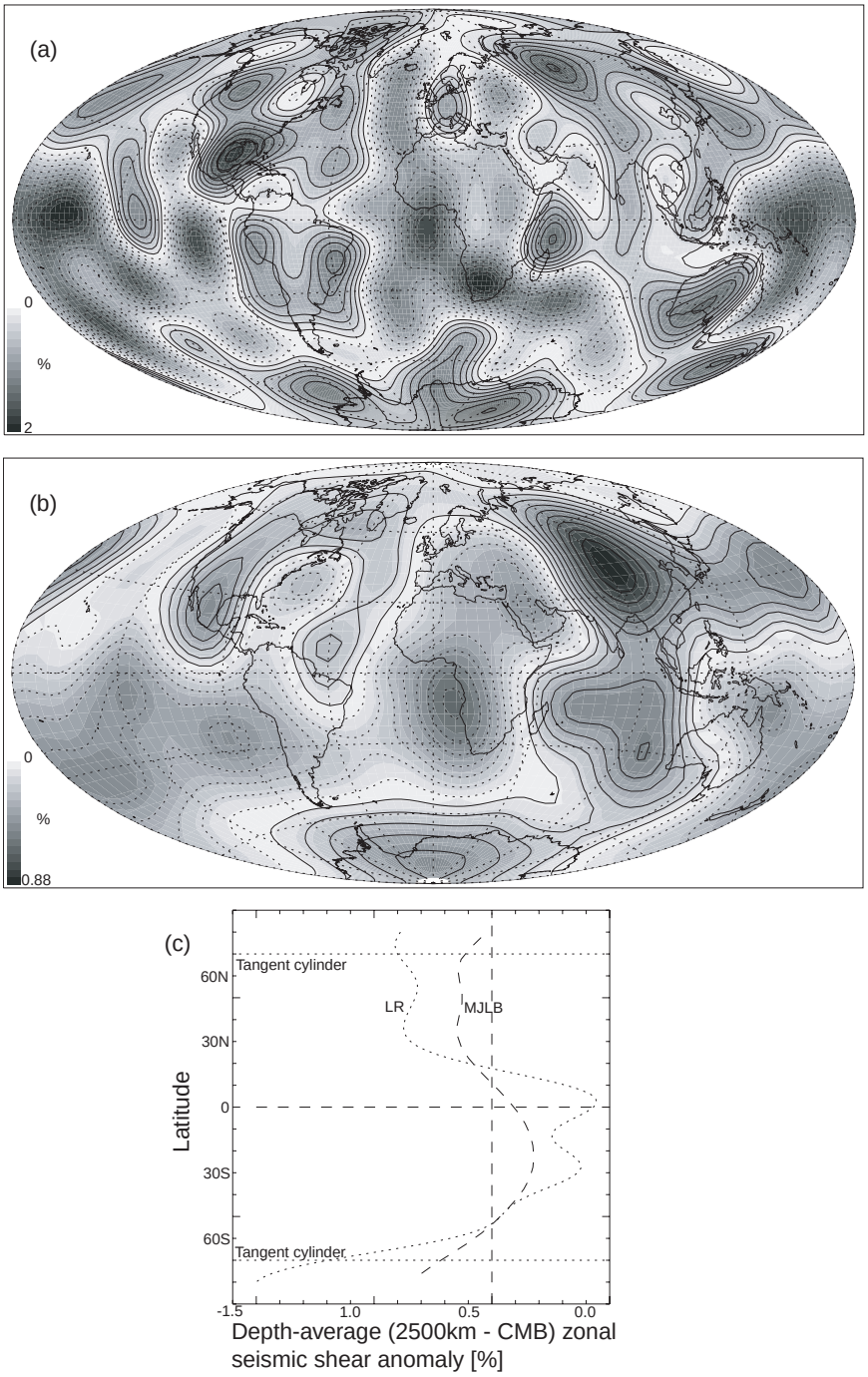

Figure 4.5: Lower mantle tomography models of LR (a) and MJLB (b), averaged from 2500 km depth to the core-mantle boundary. Grey scale represents absolute values, solid lines are positive seismic shear velocity anomalies, dotted lines are negative anomalies. Corresponding zonal averages are shown in (c).

magnetic Prandtl number. I assume rigid boundaries with fixed temperatures. To obtain the zonal angular velocity profile, I averaged the solution over 3 magnetic diffusion times. Fig. 4.6 shows the zonal core flow obtained from the numerical dynamo (depth averaged over 150 km below the outer boundary). Numerical dynamos over a wide range of parameters produce similar time-average zonal flow pattern, although there are significant variations in the zonal flow pattern in individual snapshots.

Fig. 4.6 shows a snapshot and the time-average zonal temperature and azimuthal velocity profiles from the numerical dynamo. The basic convection structure consists of two polar plumes and several equatorial plumes. The equatorial plumes wobble around the equator with time, and at any instant the temperature profile deviates from equatorial symmetry (Fig. 4.6a). However, the time-average positions of equatorial plumes are very close to the equator, and therefore the time-average temperature profile is nearly symmetric with respect to the equator (Fig. 4.6c). The time-average azimuthal velocity field is mostly a thermal wind flow driven by lateral gradients in the time-average temperature field. The most intense zonal flow is within the inner core tangent cylinder, particularly the westward polar vortex (Figs. 4.6b and 4.6d).

4.4.4 Interpretation of time-average core flow: Mantle versus core origins

Fig. 4.7 compares the zonal parts of core, tomographic, and dynamo flows, respectively. The tomographic flows were scaled and shifted to best fit the core flow. The amplitude of the numerical dynamo zonal flow U_ϕ is related to the buoyancy flux using the following scaling law:

$$U_\phi = Ra_q^{*0.5} = [(\frac{R_i}{R})\frac{B}{\Omega^3 D^2}]^{0.5} \tag{4.13}$$

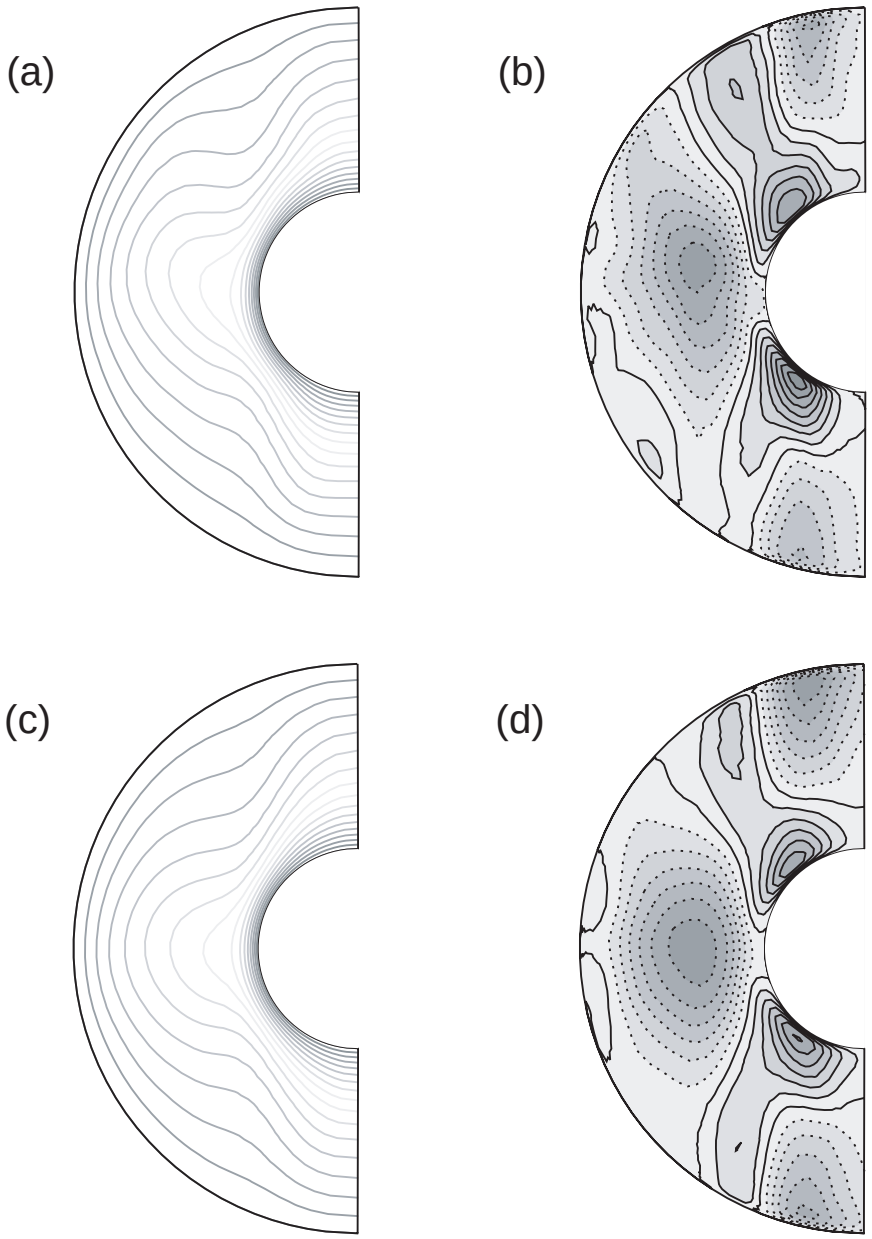

Figure 4.6: Zonal temperature (a) and azimuthal velocity (b) from a snapshot, and time-average zonal temperature (c) and azimuthal velocity (d), from a numerical dynamo with $Ra = 4E5$, $Ek = 7E-4$, $Pr = 1$ and $Pm = 5$. In (b) and (d) solid lines are positive zonal azimuthal velocities (eastward) and dotted lines are negative velocities (westward). Maximum non-dimensional velocities are $2.84Re$ in (b) and $2.43Re$ in (d), where Re is the Reynolds number.

where Ra_q^* is the heat flux based Rayleigh number, R_i is the inner core radius, $D = R - R_i$ is the shell thickness and B is the buoyancy flux (Aubert, 2005). My scaling of U_ϕ corresponds to a buoyancy flux of $\sim 3 \cdot 10^{-12}\ m^2/s^3$ which is within the range of estimated values for this parameter at the outer core (Aurnou et al., 2003). The error bars in the dynamo flow represent variation in time.

Fig. 4.7 shows that the dynamo flow can account for most of the zonal core flow at high latitudes. Specifically, the westward polar vortices seen in the core flow are present in the dynamo flow. In addition, the eastward flow at high latitudes outside the tangent cylinder in the dynamo flow is in agreement with eastward motion at similar latitudes in the core flow. However, core dynamics does not readily explain the asymmetry in the westward drift in the core flow. The dynamo flow is practically zero within 50° of the equator, whereas the core flow has substantial westward amplitude, particularly at mid-latitudes in the southern hemisphere. Mantle-driven flow offers an explanation for this asymmetry. The southern hemisphere has a larger westward drift than the northern hemisphere in both tomographic flows. The LR tomographic flow has the same wavelength and phase as the core flow, and in particular, reproduces the westward jet at $40S$ and the eastward flow at $70N$. Discrepancies between the tomographic and core flows appear mostly in the equatorial region and in mid-latitudes of the northern hemisphere.

Fig. 4.8 shows results of a test of the mantle-driven thermal wind over the entire core-mantle boundary. Fig. 4.8a shows the meridional derivative of the seismic velocities from the LR tomography model, and Fig. 4.8b shows the same quantity based on the thermal wind balance (4.11) and the azimuthal core flow. The tomographic model has a significant thermal wind in the Pacific hemisphere (Fig. 4.8a) where the historical secular variation and the core flow are generally quiet (see Figs. 4.1, 4.2 and 4.3a). The opposite relation is found in the Atlantic hemisphere. As a result, the global correlation is poor (Fig. 4.8c). Possible explanations for the poor global correlation include non-zonal core flow is transient, i.e. the

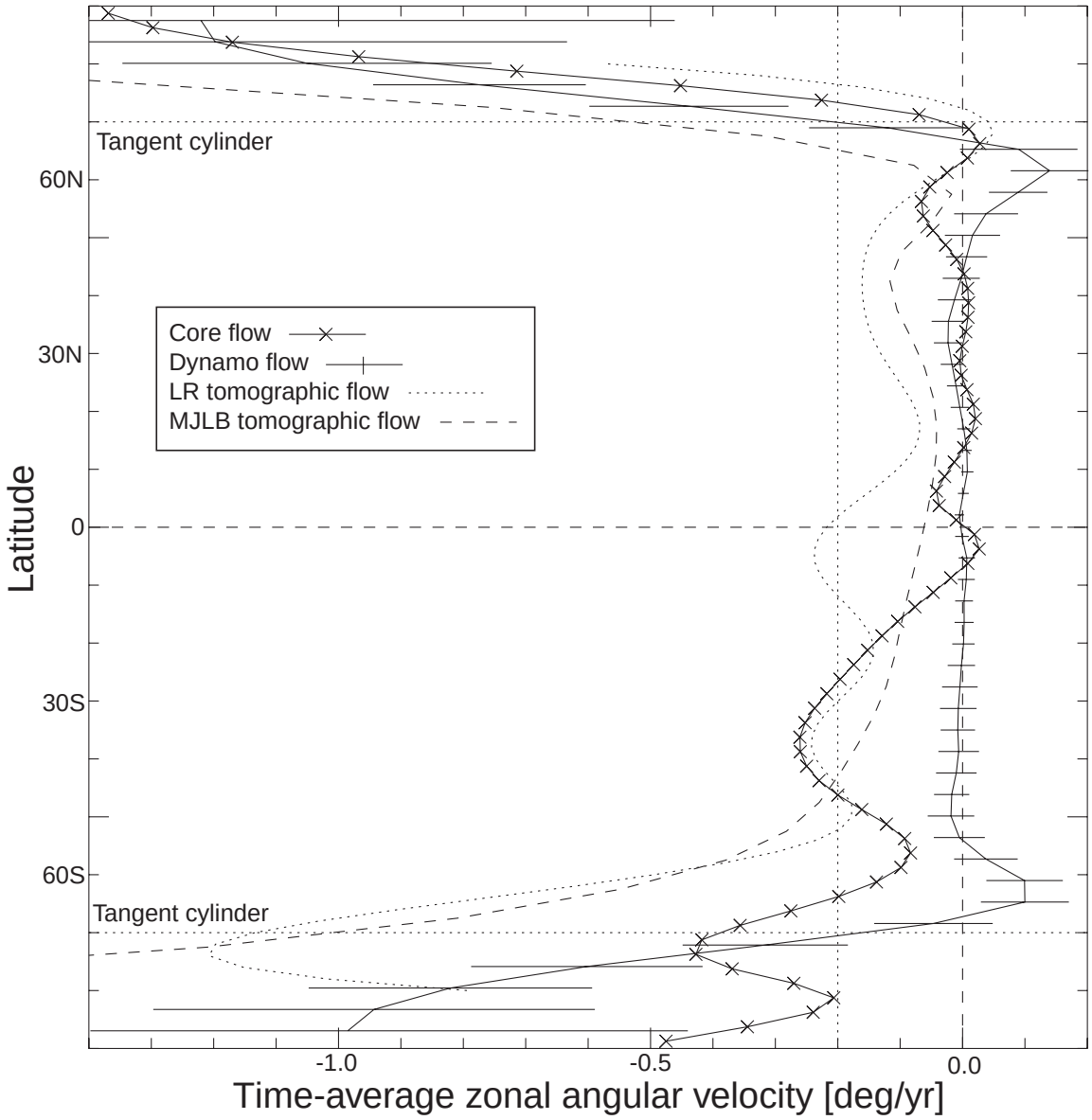

Figure 4.7: Zonal angular velocities from time-average core flow (solid + x), dynamo flow (solid + error bars), LR tomographic flow (dotted), and MJLB tomographic flow (dashed). Error bars in dynamo flow represent variation in time.

100 years interval used in this study is marginally inadequate; core-mantle coupling is not just thermal, as I assumed (see Trampert et al., 2004); or thermal wind is an over-simplified model for core flow. It is also possible that over this time interval the global core flow contains transients, but its zonal flow is essentially steady. For example, several studies assumed steady core flow in an azimuthally drifting reference frame (Voorhies and Backus, 1985; Davis and Whaler, 1996; Holme and Whaler, 2001). In the mantle reference frame, the azimuthal component of such a flow is transient, but its zonal component is steady.

My results have some similarities as well as some differences with other thermal wind interpretations of mantle-driven core flow. Bloxham and Jackson (1990) used the thermal wind equation to diagnose mantle density anomalies consistent with a model of core flow. Their results reproduce the thermal anomaly in the mantle below the Southern Indian Ocean associated with the circulatory core flow there. At that region, my time-average core flow contains the same feature (Fig. 4.3a), and my mantle-driven thermal wind correlation is good (Figs. 4.8a and 4.8b). However, globally my core flow and the core flow of Bloxham and Jackson (1990) do not explain well the seismic data by thermal wind. Comparisons can also be made between my results and thermal wind models from numerical dynamos with heterogeneous boundary conditions. Zhang and Gubbins (1992) investigated the effect of thermal wind driven by mantle heterogeneity in a kinematic dynamo model. They found that core flow structure is shifted in longitude with respect to mantle density anomalies, so that core upwellings occur where the mantle density anomalies change sign. I find this type of correlation in a few places, for example below the Southern Indian Ocean and below the Northern Atlantic Ocean (Figs. 4.3a and 4.5a). Olson and Christensen (2002) applied the MJLB lower mantle tomography model as a boundary condition in numerical dynamos with thermal core-mantle coupling. Their time-average flow contains a southern hemisphere vortex similar to ours, but the circulation in their dynamo model below North America is the reverse of ours. The discrepancy below North America could be because my

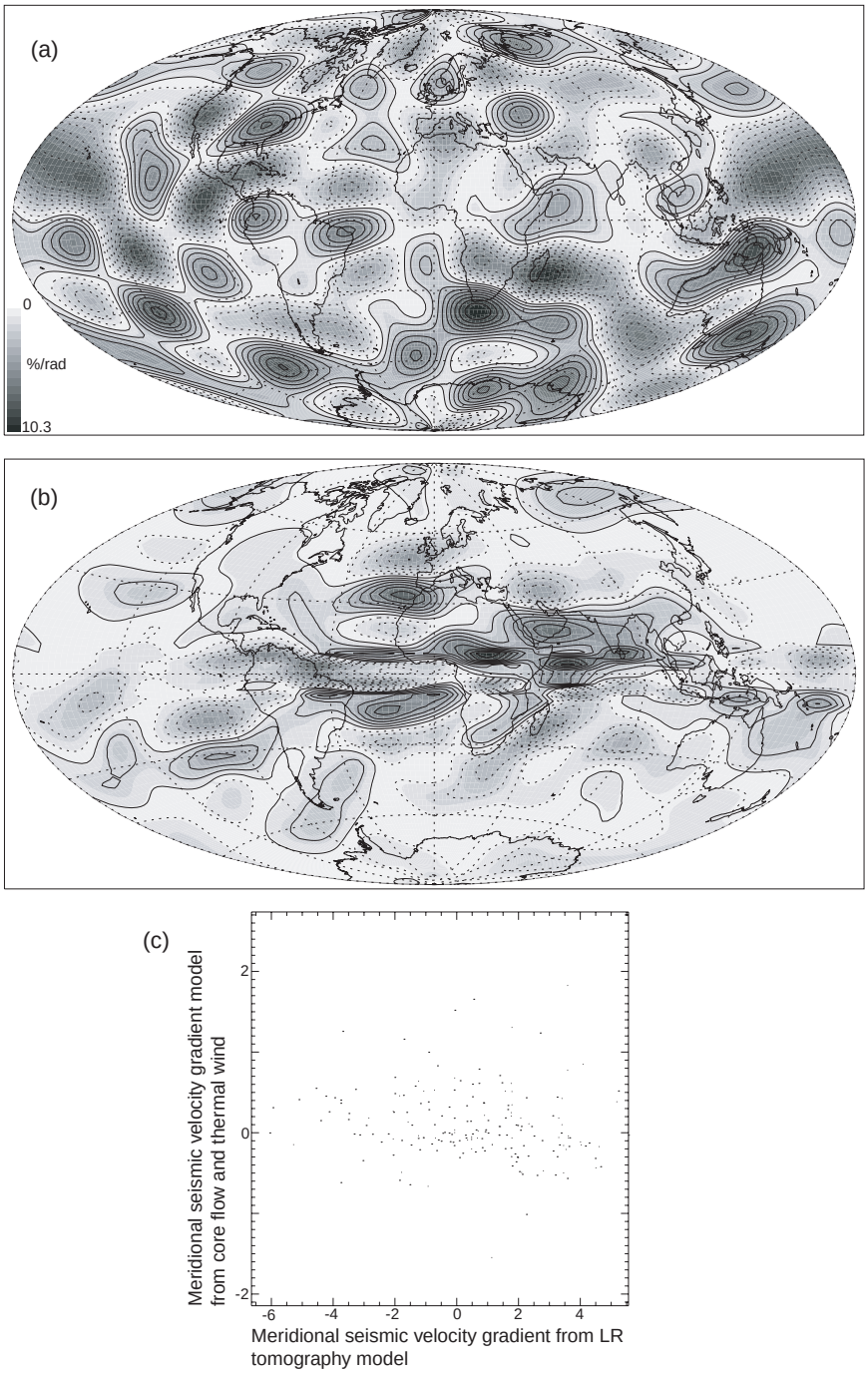

Figure 4.8: Meridional derivatives of seismic shear velocities derived from lower mantle tomography model of LR (a), time-average azimuthal core velocities and thermal wind (b), and their correlation (c). Grey scale in (a) and (b) represents absolute values, solid lines are positive seismic shear velocity gradients, dotted lines are negative velocity gradients.

core flow is transient there, or the tomographic dynamo of Olson and Christensen (2002) has the wrong core-mantle coupling in that location.

In summary, several important features of my time-average zonal core flow are in agreement with thermal wind driven by lower mantle lateral heterogeneities, while other structures appear to have their origin in the core's own dynamics. Likely mantle-driven features include hemispherical asymmetry in the westward drift, westward polar vortices, and a westward jet in the southern hemisphere at the latitude predicted by thermal coupling with the mantle. The equatorial asymmetry of the core flow at mid-latitudes appears to have a mantle origin, because the expected core-driven zonal flow is both very weak and highly symmetric there. The westward polar vortices and eastward flow near latitudes $50N$ and $50S$ may have a core origin. Globally, the azimuthal core flow is not well-correlated with mantle tomographic thermal wind. Possible explanations of this poor correlation include the short record used for averaging the core flow, non-thermal wind core flow components, and my over-simplified core-mantle coupling model. However, my results are consistent with the interpretation that the zonal part of the 100 year average core flow approximates steady-state flow at the top of the core.

4.5 Time-dependent core flow

Time-dependent core flow implies changes in the angular momentum of the core, which can be compared with observations of length-of-day variations. Fig. 4.9 shows the zonal angular velocity profiles from my core flow snapshots at 5 year intervals between 1895-1985. The center of the envelope of curves represents the time-average zonal flow, and the width of the envelope is a measure of its time-dependence. Statistics of the time-dependent flow are given in Table 1. Several points are worth emphasizing here. First, the ratio of standard deviation to mean of the rms velocities of snapshots, which represents the ratio of

time-dependent to time-average parts of my core flow, is 8.6%. Second, time-dependence is generally larger in the northern hemisphere; indeed the drift reverses its direction in some years. The westward drift at mid-latitudes of the southern hemisphere is more persistent in time and its peak angular velocity varies between $0.19 - 0.33\ ^\circ/yr$. Third, the polar vortices are evident in all profiles, despite the resolution problems in the relatively small polar cap area. A strong westward polar vortex ($0.95 - 1.80\ ^\circ/yr$) is evident in the northern polar cap, and a less intense polar vortex ($0.22 - 0.83\ ^\circ/yr$) is evident in the south.

Residual zonal flows were obtained by subtracting the time-average flow (Fig. 4.3b) from the zonal flow snapshots (Fig. 4.9). The parts of the residual flow symmetric with respect to the equator were then calculated. These equatorially-symmetric residual zonal flows represent the part of the core flow contributing to changes in the core's angular momentum. The ratio of symmetric to anti-symmetric parts of the residual zonal flows is shown in Fig. 4.10. The most symmetric zonal flow occurred at 1970, and the least symmetric zonal flow occurred at 1910. This is in agreement with previous studies, which found that core flows are more symmetric after 1970 than before (Jault et al., 1988; Jackson et al., 1993).

4.5.1 Length-of-day variations theory

Observations of length-of-day variations can be related to changes in the core's angular momentum, assuming conservation of angular momentum in the core-mantle system. The Earth changes its rotation rate on several time-scales, from seasonal fluctuations originating in the atmosphere (Eubanks et al., 1985) to geological time-scale fluctuations originating in the mantle (Munk and Mcdonald, 1960). Well-known contributions to length-of-day variations include lunar tidal dissipation ($+2.3 \pm 0.05\ ms \cdot cy^{-1}$) and postglacial rebound in polar regions ($-0.6 \pm 0.1\ ms \cdot cy^{-1}$) which combine to a $1.7 \pm 0.15\ ms \cdot cy^{-1}$ secular increase in the length-of-day over the last 2700 years (Stephenson and Morrison, 1995).

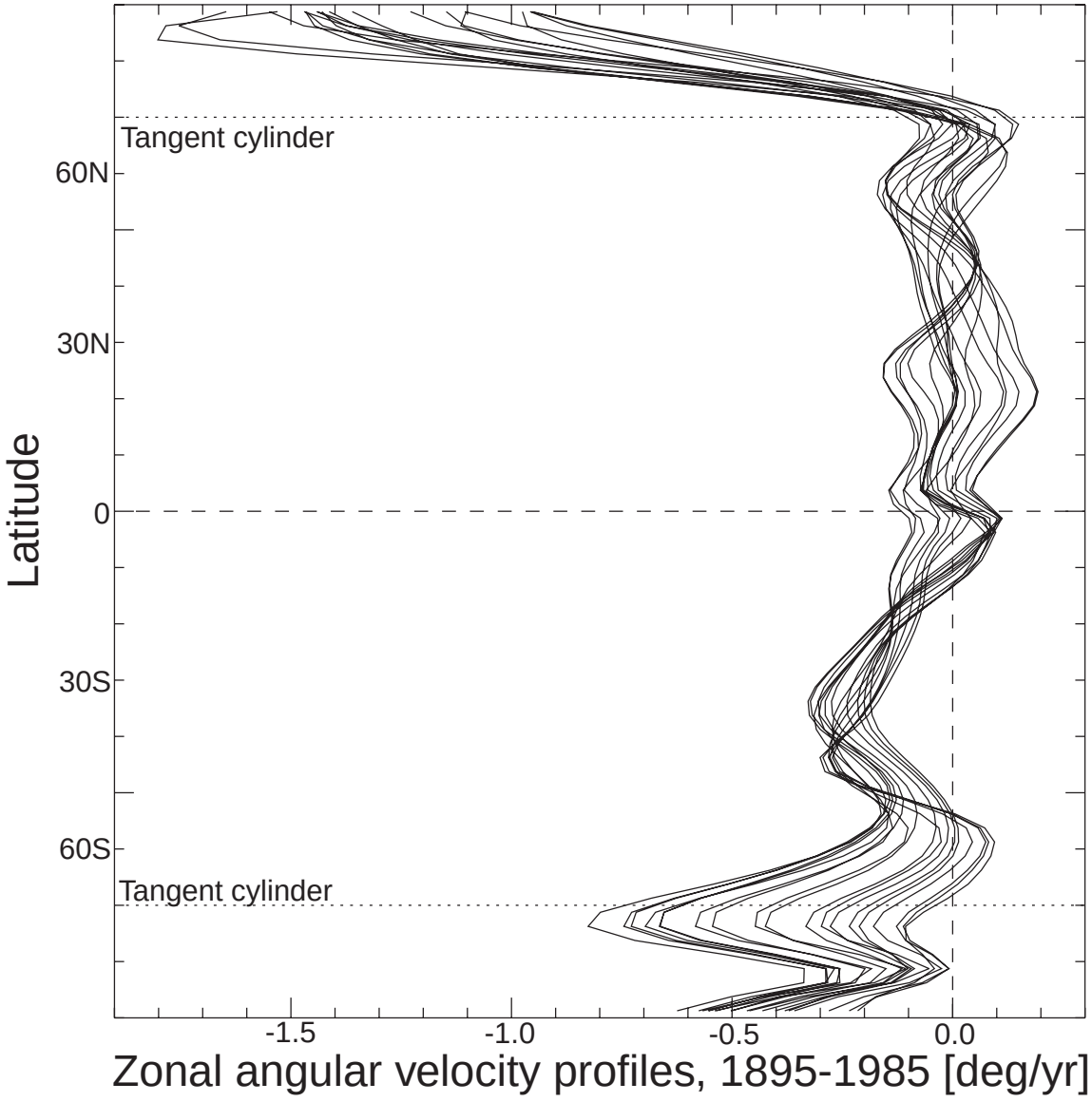

Figure 4.9: Core flow angular velocity profiles for 1895-1985 in 5 years intervals.

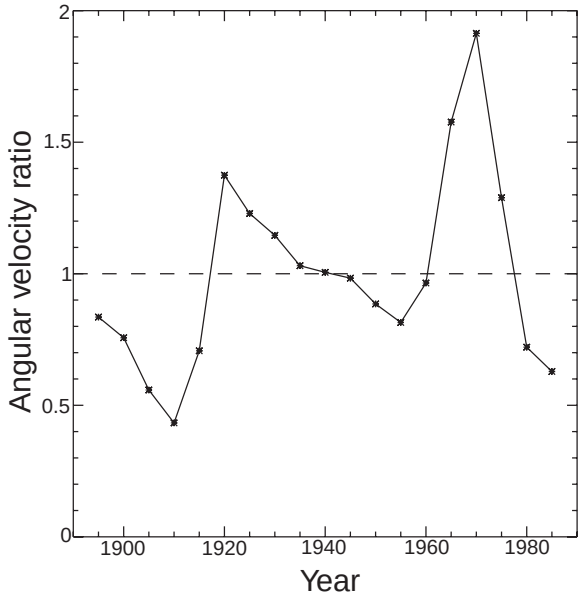

Figure 4.10: Ratio of symmetric to anti-symmetric zonal residual angular velocities for 1895-1985 in 5 years intervals.

Only the decadal variations are usually attributed to time-dependent differential rotation in Earth's liquid outer core (Jault et al., 1988; Jackson et al., 1993; Jackson, 1997; Pais and Hulot, 2000; Hide et al., 2000; Holme and Whaler, 2001).

Calculation of changes in the core's angular momentum from knowledge of core flow just below the core-mantle boundary requires projection of that flow into the volume of the outer core. Bullard and Gellman (1954) suggested that zonal core flow is geostrophic and consists of cylinders in solid body rotation about the Earth's axis of rotation. Taylor (1963) showed that for an inviscid fluid, steady motions of this type are possible when the couple exerted by Lorentz forces on those concentric cylinders vanishes (a condition known as Taylor's constraint). This cylindrical projection was used by Jault et al. (1988) to compare observed versus calculated length-of-day variations. The exact coupling mechanism between the core and the mantle is disputed. Jault and LeMouël (1989) calculated angular momentum transfer between the core and the mantle assuming topographic torques linked

with rigid body flow along such cylinders. Later, Jault and LeMouël (1991) argued that, if the amplitude of core-mantle boundary topography is as large as suggested by seismologists, then topographic torque is too large to account for length-of-day variations. They proposed an electromagnetic torque as a coupling mechanism. Regardless of the coupling mechanism to the mantle, most studies agree that the angular momentum-containing slow motion within the core is along concentric cylinders about the Earth's axis of rotation (Jault et al., 1988; Jackson et al., 1993; Jackson, 1997; Pais and Hulot, 2000).

Changes in length-of-day δT caused by core motions can be expressed as

$$\delta T(t) = \frac{{T_0}^2 (I_c + I_m)}{2\pi} \delta J_z(t) \tag{4.14}$$

where $I_c = 0.85 \cdot 10^{37}\ kg \cdot m^2$ and $I_m = 7.2 \cdot 10^{37}\ kg \cdot m^2$ are the moments of inertia of the core and the mantle respectively, $T_0 = 24$ hours, and

$$\delta J_z(t) = 2\pi \int_{R_i}^{R} \int_0^{\pi} \rho(r) \delta\omega_\phi(r, \theta, t) r^4 \sin^3\theta d\theta dr \tag{4.15}$$

is the time-residual angular momentum component in the direction of the rotation axis associated with the core motions relative to the mantle (Jackson et al., 1993). In (4.15) R_i is the radius of the inner core boundary, R is the radius of the core-mantle boundary, ρ is core density, and $\delta\omega_\phi$ is the zonal angular velocity residual, the deviation of the profiles $\omega_\phi(R, \theta, t)$ shown in Fig. 4.9 from the time-average profile shown in Fig. 4.3b.

To compute $\delta J_z(t)$, the time-average zonal core flow is subtracted from $\omega_\phi(R, \theta, t)$, and the even (symmetric with respect to the equator) angular velocity time residual $\delta\omega_\phi(R, \theta, t)$ is found. To project along concentric cylinders in a spherical coordinate system, the following expression is used:

$$\delta\omega_\phi(r, \theta, t) = \delta\omega_\phi(R, \theta^*, t) \tag{4.16}$$

where $\theta^* = \sin^{-1}(\frac{r}{R}\sin\theta)$ is the co-latitude where an axial cylinder passing through the point (r, θ) intersects the core-mantle boundary.

Although previous studies have ignored the depth-dependent density in the outer core (e.g. Jault et al., 1988; Jackson et al., 1993; Jackson, 1997; Pais and Hulot, 2000), I use the radial density profile model of Dziewonski and Anderson (1981) to evaluate the radial density profile in (4.15). Note that the inner core is not included in (4.15). The inner core has a small volume fraction and even smaller moment of inertia with respect to the whole core (Stacey, 1992), and therefore its contribution to the angular momentum of the entire core is negligible.

4.5.2 Comparison with observed length-of-day variations

Fig. 4.11 shows the δT calculated from my surface core flow and (4.14) - (4.16) versus the observed length-of-day variations since 1895. A linear trend of $1.7\ ms \cdot cy^{-1}$ has been subtracted from the observations to remove the secular increase in Earth's rotation rate due to the long-term causes listed above. Although my calculated length-of-day variations have a larger amplitude then observed, there is a reasonable agreement in terms of general trend and peak-to-peak-correlation.

Some previous studies have obtained better fits between calculated and observed length-of-day variations than ours, especially the amplitude of the variation (Jackson et al., 1993; Jackson, 1997). However, those fits were obtained by linking the core flow at different epochs. Jackson (1997) linked different epochs by minimizing the temporal variations of the flow, and Holme (1998) linked different epochs by minimizing the length-of-day variations misfit. In addition, some previous studies improved their fit by using time-dependent spectral tapering to account for the increasing uncertainty in older data (Jackson, 1997; Pais and Hulot, 2000). I do not constrain my snapshot flows these ways. Instead I invert for the core flow at each epoch independently, so my snapshot flows are uncoupled. In addition, I keep my model parameters fixed over time. Because my snapshot flows are not linked and my model parameters are time-independent, I view the length-of-day comparison as an

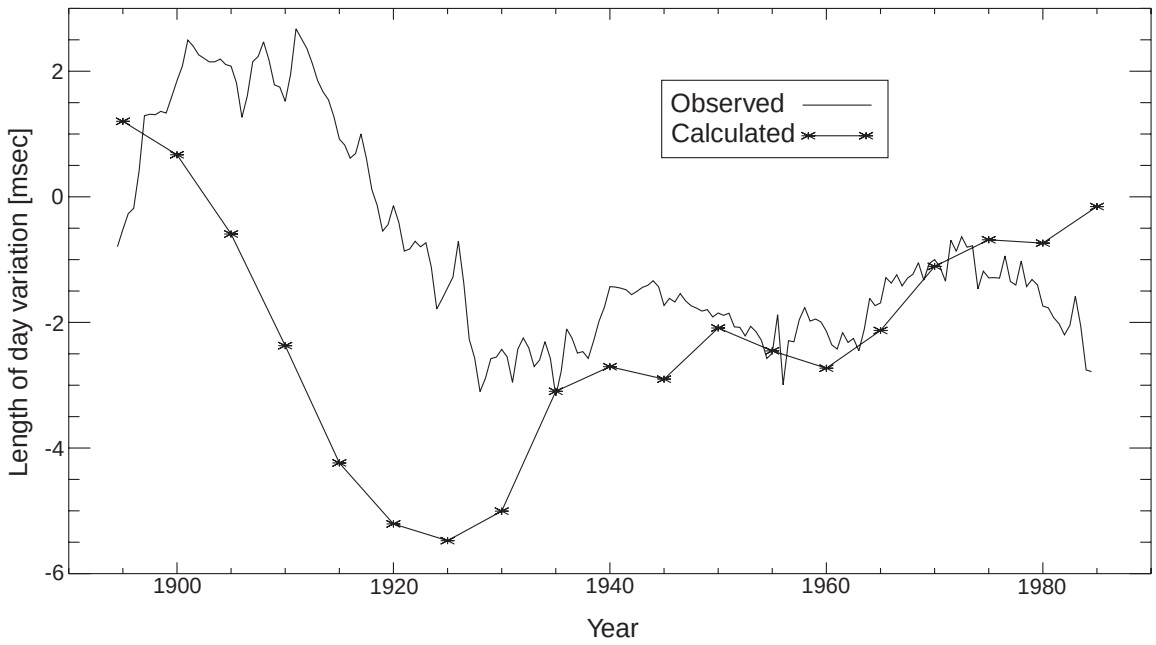

Figure 4.11: Observed versus calculated length-of-day variations. A linear trend of 1.7 $ms \cdot cy^{-1}$ has been removed from the observations.

independent test of my core flow solution.

4.5.3 Torsional oscillations model for time-dependent core flow

The correlation between the observed and calculated length-of-day variations does not answer the question of what mechanism is responsible for the time-dependent motions in the core, but many authors have argued that the mechanism is torsional oscillations. Braginsky (1970) provided a theoretical basis for torsional oscillations within the outer core, and estimated that these oscillations have a period of about 60 years. Jault et al. (1996) argued that core-mantle angular momentum exchange is a by-product of angular momentum exchange among different cylinders inside the outer core, through torsional oscillations. Zatman and Bloxham (1997) fitted the even residual zonal surface flow for the time interval 1900-1990 to a torsional oscillations model and found two damped waves

with periods of 76.2 and 52.7 years. Bloxham et al. (2002) assumed steady acceleration to fit the time interval 1957-2001 and found three damped waves with periods of 45, 20 and 13 years. They also argued that torsional oscillations are the mechanism responsible for the observed geomagnetic jerks, which are abrupt changes in the secular acceleration of the geomagnetic field.

Following Zatman and Bloxham (1997) and Bloxham et al. (2002), I fit a torsional oscillations model to the time-dependent part of my zonal core flow. I use a two-wave model for the equatorially-symmetric time-dependent zonal velocity

$$\delta u_\phi(\theta,t) = A_1(\theta)\cos(\frac{2\pi}{T_1}t + \gamma_1(\theta)) + A_2(\theta)\cos(\frac{2\pi}{T_2}t + \gamma_2(\theta)) \tag{4.17}$$

where A, T and γ are the amplitudes, periods and phases of the two waves. Figs. 4.12a and 4.12b show δu_ϕ from my core flow model and from the least-squares fit to (4.17), respectively. The best-fit periods are $T_1 = 88.3$ years and $T_2 = 48.3$ years. Note that the largest amplitudes occur at high latitudes and in the equatorial region. The misfit is shown in Fig. 4.12c. The ratio of the misfit (Fig. 4.12c) rms to the core flow (Fig. 4.12a) rms is 0.22.

The average of my periods, 68.3 years, as well as the average of the two periods found by Zatman and Bloxham (1997), 64.5 years, are very close to the 60 years period estimated by Braginsky (1970). My high frequency wave has a period close to the one found by Zatman and Bloxham (1997), but my low frequency wave has a larger period than theirs. In contrast, the periods found by Bloxham et al. (2002) are substantially smaller than ours.

Fig. 4.13 shows the latitude-dependent wave amplitudes and phases. Both waves have local amplitude maxima at the equator, but wave 1 also has a significant local maximum near latitude 62. These are not simple standing or propagating waves, since their phases are latitude-dependent. I searched for models with simpler phase relationships, unsuccessfully. For a model with the same periods $T_1 = 88.3$ years and $T_2 = 48.3$ years and $\gamma_1 = 0$,

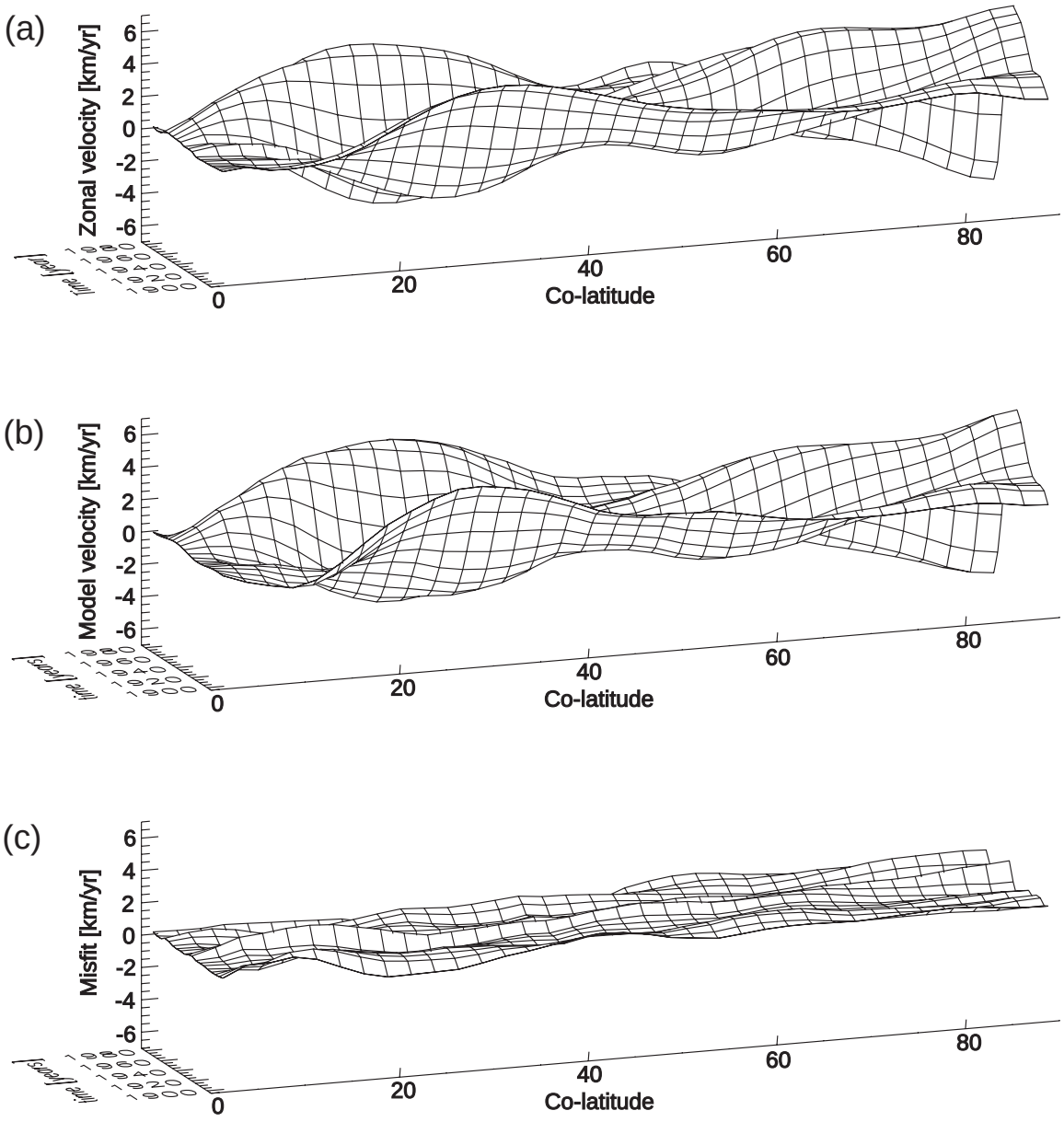

Figure 4.12: Core flow (a), two-wave model (b); and misfit between core flow and two-wave model (c).

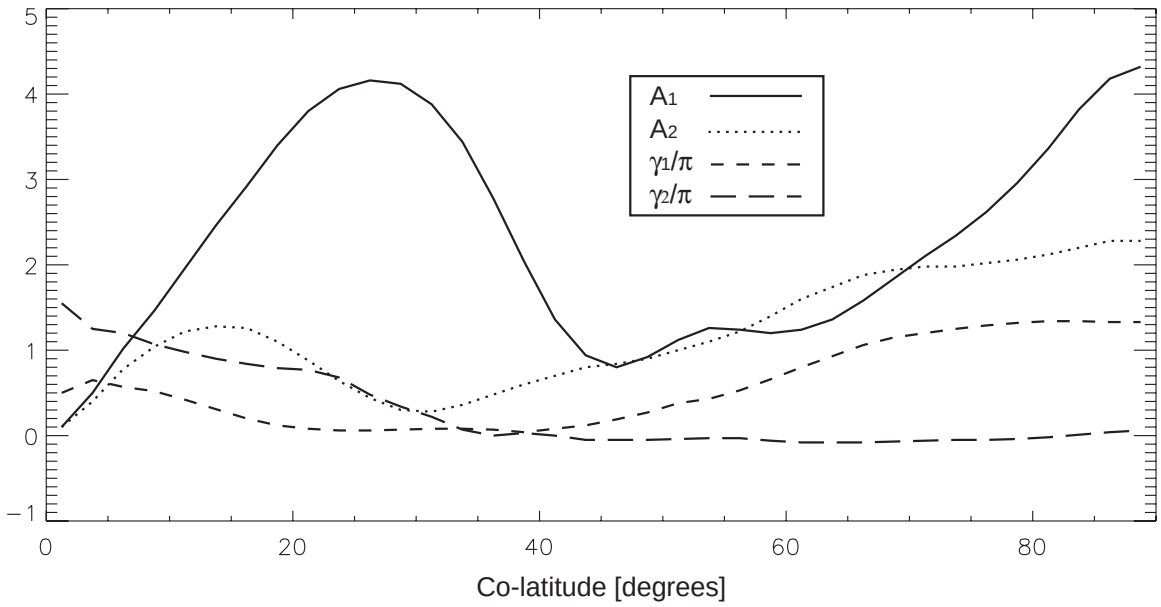

Figure 4.13: Torsional oscillations model wave parameters.

the quality of fit decreases only by 2%, but γ_2 still depends strongly on latitude. I then set both phases constant for the period of time 1940-1985 and found best-fit in periods of $T_1 = 88.4$ years and $T_2 = 59.8$ years, and the quality of fit decreases by 16%. The similarity of the periods (especially T_1) obtained this way to those obtained for the whole 1895-1985 time interval demonstrates they are not a consequence of the sampling interval, but are robust features of the symmetric residual zonal velocities. In summary, I find that the symmetric zonal part of the time-dependent core flow can be successfully fitted using a sum of two harmonic functions with constant periods, and this may be evidence to torsional oscillations at the Earth's core on decadal time-scales. I found that the periods are robust, but the complex phase relationships indicate that these torsional oscillations are not simple standing or propagating waves.

4.6 Summary

I have inverted geomagnetic secular variation data for the fluid flow below the core-mantle boundary at 5 year intervals between 1895-1985. I decompose the core flow into time-average and time-dependent parts. The time-average zonal core flow, which may represent a long-term steady flow at the top of the core, is compared with models of thermal wind at the top of the core driven by density anomalies originating in the core and the mantle. Core-origin flow can account for large westward polar vortices and eastward flow at high latitudes outside the tangent cylinder. Mantle-driven thermal wind seems to account for the hemispherical asymmetry at low and mid-latitudes. The time-dependent part of my core flow is in overall agreement with decade-scale length-of-day variations, and a torsional oscillations model with periods near 88 and 48 years but complex phase relationships provides an adequate fit to this part of my core flow.

Epoch	$\vec{u}_h$		$< u_\phi >$		$< u_\theta >$		$\nabla_h \cdot \vec{u}_h$	
	max	**rms**	**max**	**rms**	**max**	**rms**	**range**	**rms**
1895	105.59	11.94	9.54	2.94	1.46	0.53	-0.16,0.14	0.056
1900	110.40	12.45	10.13	3.08	1.63	0.54	-0.15,0.16	0.062
1905	125.98	13.18	10.73	3.40	1.79	0.56	-0.13,0.17	0.068
1910	132.01	14.18	11.88	3.92	1.93	0.66	-0.17,0.19	0.073
1915	128.66	14.77	13.61	4.53	2.11	0.77	-0.19,0.21	0.077
1920	123.62	14.74	15.09	4.96	2.36	0.90	-0.23,0.23	0.083
1925	120.96	14.71	15.95	5.42	2.55	1.00	-0.27,0.24	0.091
1930	153.94	14.60	16.22	6.12	2.70	1.07	-0.31,0.25	0.100
1935	146.95	13.05	14.31	6.16	2.49	1.01	-0.30,0.21	0.094
1940	145.09	13.74	14.79	7.05	2.50	1.04	-0.30,0.21	0.098
1945	149.57	14.44	15.13	7.40	2.51	1.06	-0.30,0.21	0.099
1950	118.34	12.50	12.95	5.67	1.81	0.78	-0.21,0.17	0.074
1955	100.02	11.88	12.60	5.03	1.40	0.59	-0.13,0.17	0.058
1960	114.63	11.78	12.50	5.31	1.14	0.45	-0.08,0.19	0.053
1965	125.98	11.61	12.08	5.77	1.03	0.41	-0.07,0.22	0.054
1970	120.47	11.44	11.60	5.57	1.07	0.43	-0.08,0.25	0.057
1975	101.65	11.72	11.79	4.96	1.22	0.51	-0.13,0.28	0.062
1980	82.58	11.94	12.31	4.27	1.35	0.58	-0.19,0.30	0.066
1985	92.77	11.99	12.52	3.69	1.43	0.64	-0.24,0.31	0.072
Standard deviation	15.02	1.11	1.54	0.99	0.49	0.20	0.07,0.04	0.013
Time-average	78.69	11.27	12.09	3.60	1.74	0.63	-0.18,0.17	0.063

Table 4.1: Core flow statistics. <> denotes zonal average, rms is areal-average of absolute velocities; standard deviation is with respect to the mean of the epoch values; time-average velocities are from the average of the potentials Ψ and Φ at all epochs. Maximum zonal values are outside the tangent cylinder; maximum zonal azimuthal velocity is westward, maximum zonal meridional velocity is northward; positive divergence is upwelling and negative divergence is downwelling. All velocities are km/yr; divergence is 1/century.

Chapter 5

Testing core flow recovery using numerical dynamos

5.1 Introduction

Models of fluid flow at the top of the Earth's outer core have been obtained by inverting geomagnetic secular variation data using the assumption of frozen magnetic flux (Gire et al., 1986; Voorhies, 1986; Bloxham, 1989; Gire and LeMouël, 1990; Bloxham and Jackson, 1991; Jackson et al., 1993; Pais and Hulot, 2000; Hulot et al., 2002; Amit and Olson, 2004; Amit and Olson, 2005). These inversions suffer from several problems including unmodeled magnetic diffusion, data truncation, inaccurate modeling of the tangential divergence of the core flow, and non-uniqueness. Thus, core flow models differ from each other substantially.

The differences between core flow models obtained from the same secular variation data indicate the need for objective testing. Rau et al. (2000) proposed a core flow inversion test using synthetic secular variation data produced by 3D self-consistent magnetohydrodynamic dynamo models in a spherical shell. Their inversion method assumed tangential

geostrophy or pure toroidal flow, and used a spectral numerical method. Rau et al. (2000) succeeded in recovering most of the main features of the flow, but their results highlighted several problems: (1) The correct flow magnitude is obtained only by degrading the data misfit; (2) unmodeled magnetic diffusion effects contaminate the flow pattern; and (3) data truncation effects might cause flow artifacts.

Recently Amit and Olson (2004) proposed a new core flow inversion method. They assumed that the tangential divergence of the flow is a superposition of tangential geostrophy (e.g. LeMouël, 1984), and helical flow in which the tangential divergence is correlated with the radial vorticity. They solved a set of partial differential equations for the flow potentials on a grid. The helical flow assumption is common in rotating-convecting flows, as shown by analytical examples (Amit and Olson, 2004) and in numerical dynamos (Olson et al., 2002). I test my core flow imaging method using the output of numerical dynamo models. I compare the inverted flow with the true dynamo flow to assess the quality of my inversion method.

5.2 Numerical dynamo models

Recent numerical dynamos model magnetic field generation by thermal convection of an electrically conducting fluid in a rotating spherical shell (e.g. Olson et al., 1999). The model solves the full 3D non-dimensional incompressible magnetohydrodynamics equations for the velocity vector $\vec{u}$, the magnetic field vector $\vec{B}$, and the temperature T

$$Ek(\frac{\partial \vec{u}}{\partial t} + \vec{u} \cdot \nabla \vec{u} - \nabla^2 \vec{u}) + 2\hat{z} \times \vec{u} + \nabla P = Ra \frac{\vec{r}}{R} T + \frac{1}{Pm}(\nabla \times \vec{B}) \times \vec{B} \tag{5.1}$$

$$\frac{\partial \vec{B}}{\partial t} = \nabla \times (\vec{u} \times \vec{B}) + \frac{1}{Pm} \nabla^2 \vec{B} \tag{5.2}$$

$$\frac{\partial T}{\partial t} + \vec{u} \cdot \nabla T = \frac{1}{Pr} \nabla^2 T \tag{5.3}$$

$$\nabla \cdot \vec{u} = 0 \tag{5.4}$$

$$\nabla \cdot \vec{B} = 0 \ , \tag{5.5}$$

where t is time, $\hat{z}$ is a unit vector in the direction of the rotation axis, P is pressure, and $\vec{r}$ is the position vector. Four non-dimensional parameters in (5.1) - (5.5) control the dynamo action. The (modified) Rayleigh number represents the strength of convection

$$Ra = \frac{\alpha g_0 \Delta T D}{\nu \Omega} \ , \tag{5.6}$$

where α is thermal expansivity, g_0 is gravitational acceleration on the outer boundary at radius R, ΔT is temperature difference between the inner and outer boundaries, D is shell thickness, ν is kinematic viscosity, and Ω is rotation rate. The Ekman number represents the ratio of viscous and Coriolis forces

$$Ek = \frac{\nu}{\Omega D^2} \ , \tag{5.7}$$

the Prandtl number is the ratio of kinematic viscosity to thermal diffusivity κ

$$Pr = \frac{\nu}{\kappa} \ , \tag{5.8}$$

and the magnetic Prandtl number is the ratio of viscosity to magnetic diffusivity λ

$$Pm = \frac{\nu}{\lambda} \ . \tag{5.9}$$

I selected four cases from a larger set of cases from a systematic parameter space study (Christensen et al., 1999; Olson and Christensen, 2002). Table 5.1 summarizes the parameters, boundary conditions, resolution, and the depth of "free stream velocity" below the Ekman boundary layer for the four cases I examined. In all cases the boundaries are rigid, the regions outside the shell are perfect insulators, and the inner boundary temperature is fixed. The outer boundary has fixed temperature in cases 1 and 2, fixed uniform heat flux in case 3, and heat flow based on the lowermost mantle seismic tomography model of Masters et al. (1996) in case 4. Cases 1 and 2 have a lower resolution with respect to cases 3 and

4. In all cases the dynamo models reached a state of statistical equilibrium, i.e. the magnetic and kinetic energies fluctuated chaotically without a secular trend. In all cases the dipole mode dominates the magnetic energy spectrum, and a significant secular variation is present.

	Case 1	**Case 2**	**Case 3**	**Case 4**
Ra	3E5	2.4E5 $(4.3Ra_{crit})$	1.5E7 $(22Ra_{crit})$	1.5E7 $(22Ra_{crit})$
Ek	1E-3	1E-3	1E-4	1E-4
Pr	1	1	1	1
Pm	4	3	2	2
T_{cmb}	fixed	fixed	uniform heat flux	tomographic
l_{max}	53	42	85	85
N_r	33	33	41	41
h_{ek}	0.03834	0.03834	0.02474	0.02474
Δt	16.975e-4	4.00066e-3	10.1060e-5	9.29280e-5
R_m	111	70	319	314
R_m^*	145	122	189	195

Table 5.1: Experimental setup. Ra, Ek, Pr and Pm are the (modified) Rayleigh, Ekman, Prandtl and magnetic Prandtl numbers, respectively. T_{cmb} represents the type of thermal boundary condition applied on the outer boundary. l_{max} is the maximal spherical harmonic, and N_r is the number of radial grid points. h_{Ek} is the non-dimensional Ekman boundary layer thickness, the depth of the "free stream" where the dynamo velocity is considered for reference. Δt is the time difference (in units of viscous diffusion time) between the two B_r snapshots from which the average magnetic field and the difference secular variation were calculated. The magnetic Reynolds number R_m is calculated by averaging the dynamo output in volume and time, where the core's radius is taken as a length-scale; in the effective magnetic Reynolds number R_m^* I use $2\pi R/\bar{l}_B$ as a length-scale, where the average magnetic harmonic is given in terms of the magnetic power spectrum ${B_l}^2(l)$ by $\bar{l}_B = \sum_l l{B_l}^2 / \sum_l {B_l}^2$.

The secular variation $\partial B_r/\partial t$ was determined by finite-differencing of B_r in time, using two snapshots of the magnetic field at times t and $t + \Delta t$. Two corresponding snapshots of the velocity field at the top of the "free stream" just below the Ekman boundary layer were averaged to obtain the dynamo flow $\vec{u}_h^*$ that is compared with the inverted flow $\vec{u}_h$. Due to computational limitations, numerical dynamos use an Ekman number larger than

the core's, and therefore, the Ekman boundary layer in the dynamo models is thicker than in the core. Nevertheless, the magnetic boundary layer is thicker than the Ekman boundary layer (Rau et al., 2000), so it is safe to compute the secular variation at the outer boundary, and the dynamo velocity just below the Ekman boundary layer.

5.3 Inversion method

The fluid flow just below the outer boundary $\vec{u}_h$ can be obtained from the radial component of the magnetic field B_r and its time derivative $\partial B_r/\partial t$ on the outer boundary. The radial component of (5.2) just below the outer boundary is

$$\frac{\partial B_r}{\partial t} + \vec{u}_h \cdot \nabla B_r + B_r \nabla_h \cdot \vec{u}_h = \frac{1}{Pm}\left(\frac{1}{r^2}\frac{\partial^2}{\partial r^2}(r^2 B_r) + \nabla_h^2 B_r\right) \ , \tag{5.10}$$

where r is the radial coordinate and $\nabla_h^2 = \nabla^2 - \frac{1}{r^2}\frac{\partial}{\partial r}(r^2\frac{\partial}{\partial r})$. The first term on the right hand side of (5.10) cannot be computed from geomagnetic data because the variation of B_r with depth is unknown, but knowing B_r at the outer boundary the second term can be calculated. In the customary frozen-flux approximation both terms on the right hand side of (5.10) are neglected (Roberts and Scott, 1965).

The tangential velocity can generally be expressed in terms of a streamfunction Ψ and a scalar potential Φ as

$$\vec{u}_h = \vec{u}_{tor} + \vec{u}_{pol} = \nabla \times \Psi \hat{r} + \nabla_h \Phi \ , \tag{5.11}$$

where $\hat{r}$ is the unit radial vector, and $\nabla_h = \nabla - \partial/\partial r$ in a spherical coordinate system (r, θ, ϕ). Substitution of (5.11) into (5.10) yields

$$\frac{\partial B_r}{\partial t} + \frac{1}{R^2 sin\theta}\left(\frac{\partial \Psi}{\partial \phi}\frac{\partial B_r}{\partial \theta} - \frac{\partial \Psi}{\partial \theta}\frac{\partial B_r}{\partial \phi}\right) + \frac{1}{R^2}\left(\frac{\partial \Phi}{\partial \theta}\frac{\partial B_r}{\partial \theta} + \frac{1}{sin^2\theta}\frac{\partial \Phi}{\partial \phi}\frac{\partial B_r}{\partial \phi}\right) + B_r \nabla_h^2 \Phi = \frac{1}{Pm}\left(\frac{1}{r^2}\frac{\partial^2}{\partial r^2}(r^2 B_r) + \nabla_h^2 B_r\right) \tag{5.12}$$

where R is the core radius.

Amit and Olson (2005) modeled the tangential divergence of velocity by a superposition of the previously-used tangential geostrophy assumption (LeMouël, 1984; Gire and LeMouël, 1990; Jackson, 1997; Hulot et al., 2002), and a helical flow assumption

$$\nabla_h \cdot \vec{u}_h = \mp k\zeta + \frac{\tan\theta}{R} u_\theta \ . \tag{5.13}$$

The first term on the right hand side of (5.13) represents the helical flow assumption. It assumes that the tangential divergence is correlated with the radial vorticity ζ, where the minus sign applies to the northern hemisphere and the plus sign to the southern hemisphere. The second term on the right hand side of (5.13) represents the tangential geostrophy assumption. Substitution of (5.11) into (5.13) yields

$$\nabla_h^2 \Phi = \mp k \nabla_h^2 \Psi + \frac{tan\theta}{R^2}\left(\frac{1}{sin\theta}\frac{\partial \Psi}{\partial \phi} + \frac{\partial \Phi}{\partial \theta}\right) \ . \tag{5.14}$$

The non-dimensional constant k is essentially a free parameter and describes the strength of helicity in the core. Simple analytical models of rotational flows and results from numerical dynamos suggest that $0.5 > k > 0.05$ (Amit and Olson, 2004).

I have solved (5.12) and (5.14) simultaneously in an iterative way to obtain the potentials Ψ and Φ just below the outer boundary. I have used a second order, central finite-difference method on a regular spherical grid with radius R. My method is identical to the one used by Amit and Olson (2005), including a special treatment of the equatorial region as a non-geostrophic belt. The numerical convergence of my method relies on positive effective streamfunction diffusivity, therefore the sign of B_r in the helical flow term (part of last term on the left hand side of (5.12)) is reversed in areas of reversed magnetic flux (Amit and Olson, 2004). In some solutions frozen-flux is assumed and both terms on the right hand side of (5.12) are neglected, and in others the term representing tangential magnetic diffusion is included in the inversions.

The areal-average deviation of the secular variation from its forward calculated value based on (5.12), normalized by the areal-average secular variation, is defined as the secular

variation misfit M_{sv}. Similarly, the areal-average deviation of (5.14) from equality, normalized by the areal-average tangential divergence, is defined as the divergence misfit M_{div}. Those misfits are used to verify and quantify the convergence of the iterative inversion scheme.

5.4 Statistic measures of the flow recovery

I evaluate the quality of fit in terms of flow magnitude and flow pattern by comparing the inverted velocity $\vec{u}_h$ with the dynamo velocity $\vec{u}_h^*$. The agreement in magnitude is evaluated by the ratio of the areal-average inverted velocity to the areal-average dynamo velocity, and similarly by the ratio of their maximum absolute velocities. The quality of fit of the flow pattern is evaluated by the correlation coefficient (Rau et al., 2000)

$$c = \frac{\int \vec{u}_h \cdot \vec{u}_h^* dS}{\sqrt{\int \vec{u}_h \cdot \vec{u}_h dS \int \vec{u}_h^* \cdot \vec{u}_h^* dS}} \ , \tag{5.15}$$

where dS is an area element on the outer boundary. A more severe statistical test measures the pointwise quality of the flow recovery, defined by the areal-average absolute vector difference between the inverted and dynamo velocities, $|\vec{u}_h - \vec{u}_h^*|$, normalized by the areal-average absolute dynamo velocity

$$p = 1 - \frac{\int |\vec{u}_h - \vec{u}_h^*| dS}{\int |\vec{u}_h^*| dS} \ . \tag{5.16}$$

Large values of c and p correspond to high-quality recovery of flow. The reference value for p, i.e. the value from two random velocity vectors of the same magnitude, is -0.41 (-41%). In addition, note that c is a measure of pattern, but p is also affceted by the magnitude.

5.5 Results

5.5.1 Large-scale dynamos

I begin by describing the inversions of relatively large-scale numerical dynamos. Fig. 5.1 shows the radial magnetic field and secular variation of case 1. The global magnetic field morphology is similar to the geomagnetic field on the core-mantle boundary, with dipolar dominance and intense flux at high-latitudes. Also, the typical length-scale of the secular variation is smaller than the length-scale of the magnetic field, as is observed for the geomagnetic field on the core-mantle boundary (Hulot et al., 2002). However, some local morphological differences are worth noting. The geomagnetic field in the equatorial region contains high-intensity normal polarity flux (Jackson, 2003), as opposed to the dynamo magnetic field that contains very low-intensity flux there (Fig. 5.1a). Also, a large and intense reversed geomagnetic field structure like the one below mid-latitudes of the Southern Atlantic Ocean is not evident in the dynamo magnetic field.

Figs. 5.2a and 5.2b show the true dynamo velocity and the inverted velocity, respectively. The inverted velocity is obtained using $k = 0.1$ with tangential magnetic diffusion included. Due to the relatively low spatial resolution used in the dynamo model (see Table 5.1), a $5^\circ \times 5^\circ$ grid was sufficient for the inversion. The statistics of case 1 is summarized in Table 5.2.

The dynamo flow is characterized by high-latitude vortices, strong meridional jets due to columnar convection, some equatorial symmetry, and a significant amount of flow along B_r-contours. Most of the main flow features in the dynamo flow are also present in the inverted flow. In the northern hemisphere, the vortices centered at $[195E, 52.5N]$ and $[250E, 42.5N]$ (Fig. 5.2a) appear with the correct position and direction of circulation in the inverted flow (Fig. 5.2b). Northward jets at $20E$ and $95E$ and southward jets at $75E$ and $325E$ and most southern hemispheric main flow features are also well-recovered. For

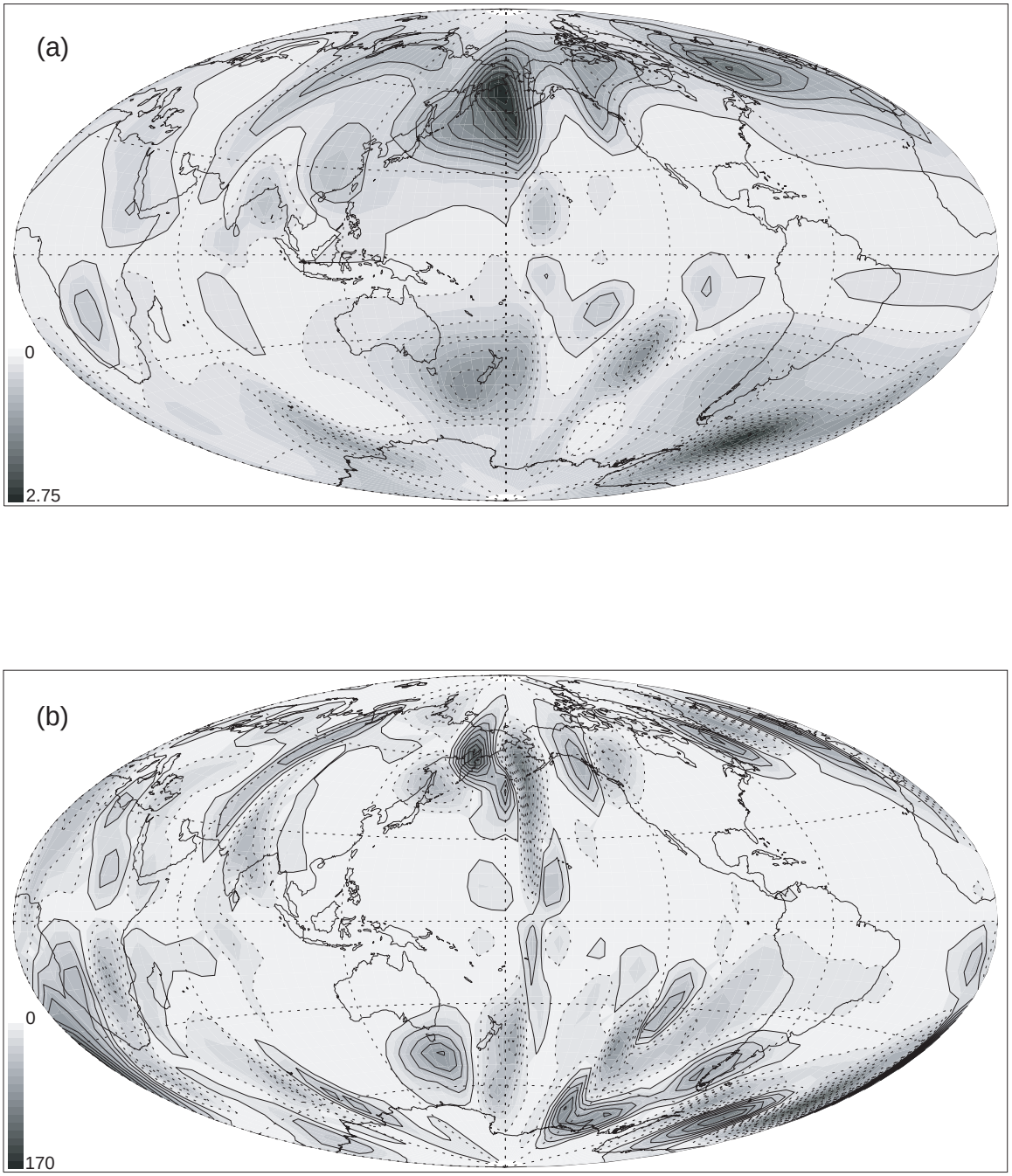

Figure 5.1: Radial magnetic field (a) and secular variation (b) on the outer boundary for case 1. Grey scale represents absolute values, solid lines are positive, dotted lines are negative.

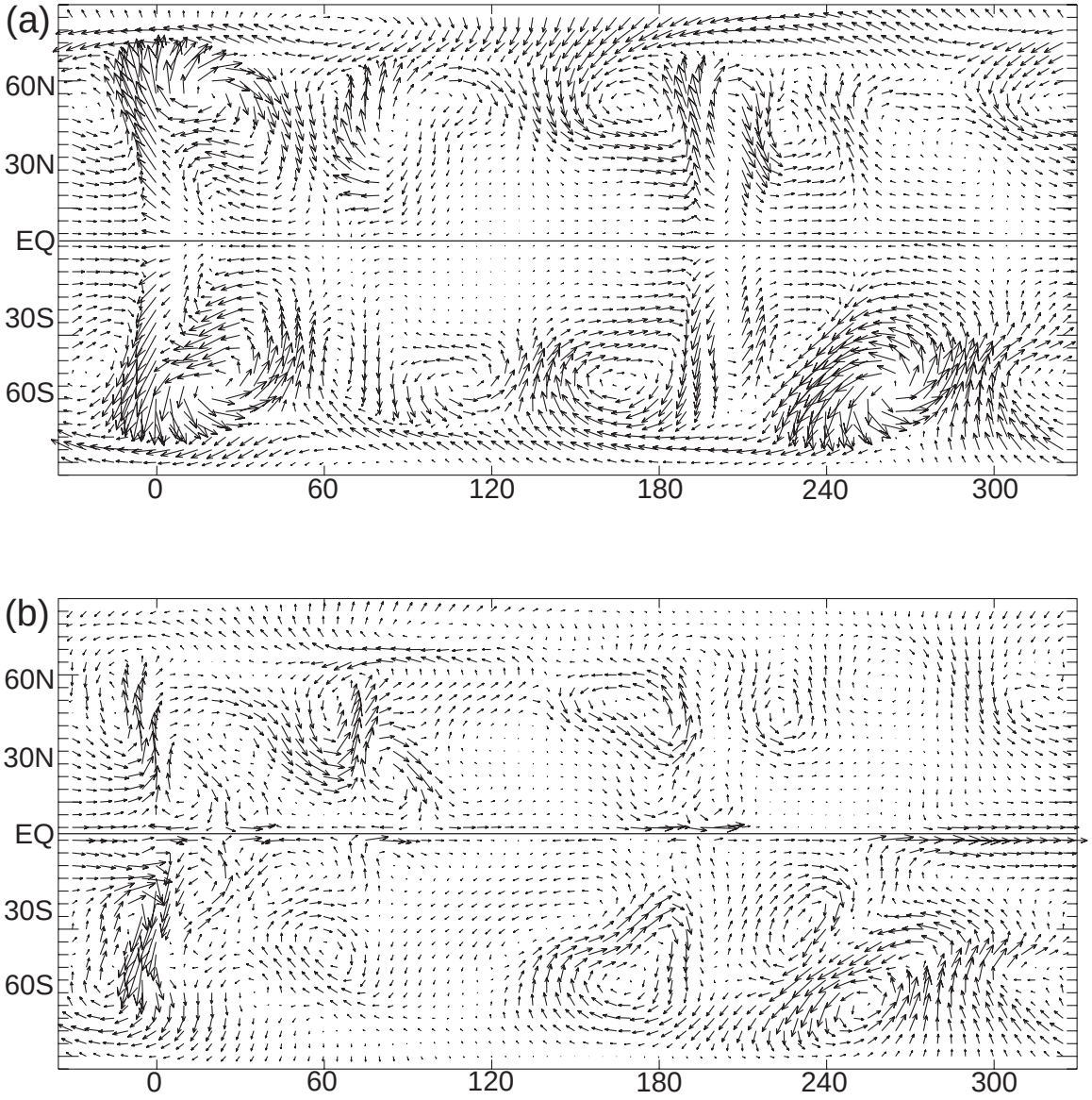

Figure 5.2: Dynamo flow (a) and inverted flow (b) for case 1 with tangential magnetic diffusion. Maximum velocity in (a) is 100.04, and velocity in (b) scales according to (a).

Case	**k**	$\nabla_h^2 B_r$	$\|\vec{u}_h\|_m / \|\vec{u}_h^*\|_m$	$\bar{u_h}/\bar{u_h}^*$	c	c_{ee}	p **%**	M_{sv}	M_{div}
1	0.1	no	0.80	0.71	0.464	0.525	3.97	0.2	2.7
1	0.07	no	1.05	0.86	0.457	0.517	-1.75	0.2	4.1
1	0.05	no	1.35	1.03	0.434	0.492	-11.99	0.3	5.7
1	0.1	yes	0.90	0.79	0.513	0.590	7.56	0.7	2.8
2a	0.1	no	0.85	0.76	0.251	0.278	-10.44	2.42	5.42
2a	0.1	yes	0.74	0.76	0.480	0.555	7.51	0.47	3.22
2b	0.1	no	0.79	0.53	0.305	0.381	0.82	1.85	1.93
2b	0.1	yes	0.91	0.64	0.521	0.644	13.40	0.25	2.22

Table 5.2: Statistics of cases 1 and 2. $\vec{u}_h$ is the inverted velocity, $\vec{u}_h^*$ is the true dynamo velocity. $||$ and m denote absolute value and maximum, respectively. $\bar{u}$ denotes the areal-average of $\vec{u}$. 2a and 2b are two different snapshots of the same simulation. c is the correlation coefficient defined in (5.15), c_{ee} is the same coefficient excluding the 10° latitude band around the equator, p is the pointwise correlation defined in (5.16). M_{sv} and M_{div} are the secular variation and divergence misfits in %, respectively.

example, the vortices centered at $[190E, 57.5S]$ and $[255E, 37.5S]$ are recovered by the inverted flow both in terms of position and direction of circulation. The vortex centered at $[285E, 57.5S]$ in the dynamo flow is shifted by about 10° to the southwest in the inverted flow.

In some places the inversion fails to recover the dynamo flow. For example, the anti-cyclonic vortex centered at $[40E, 52.5N]$ is not found in the inversion. Also, between longitudes $75E - 100E$ the meridional jets in the inverted flow connect by a eastward flow at latitudes $22.5N - 37.5N$, whereas in the dynamo flow this region exhibits a shear flow.

Previously-used physical assumptions for the tangential divergence of the flow do not solve the problem of non-uniqueness completely. Spectral methods handle this problem by minimizing the null-space vector contribution to the flow solutions. My helical flow assumption removes non-uniqueness; therefore, there is no null-space vector in my inversions (Amit and Olson, 2004). Some of the main flow features in the dynamo flow contain significant toroidal flow along B_r-contours, and this flow component is well-recovered by the inverted flow. The secular variation associated with these flow structures arise from ad-

vection and stretching by poloidal flow; my helical-geostrophic toroidal-poloidal coupling model allows to constrain these flows. For example, the main magnetic field structure in the northern hemisphere is a large and intense normal flux located between longitudes $170E - 230E$ and between latitudes $30N - 80N$ (Fig. 5.1a). The dynamo flow at that area is a cyclonic vortex with a significant flow component along B_r-contours (Fig. 5.2a). This vortex is well-recovered by the inverted flow (Fig. 5.2b). Note that the eastern margin of the magnetic flux structure is oriented north-south and coincides with the northward jet in the dynamo and inverted flows.

The dynamo flow in the equatorial region is very weak (Fig. 5.2a). Nevertheless, the inversion predicts some flow, mostly zonal, in that region (Fig. 5.2b). Olson et al. (1999) found that the zonal displacement of magnetic flux at low-latitudes is not due to zonal flow, but due to magnetic diffusion effects. Similar interpretation to equatorial flow artifacts was given by Rau et al. (2000). These flow artifacts degrade the statistics of the fit significantly.

Magnetic diffusion effects are more pronounced for the fully resolved magnetic fields of dynamo models than they are for the geomagnetic field truncated to a moderate spherical harmonic degree. In geomagnetic core flow inversions, the full magnetic diffusion effect cannot be considered because the geomagnetic field is only known over the core-mantle boundary, and its radial variation is unknown. However, the tangential part of magnetic diffusion can be calculated. I have examined the effects of tangential magnetic diffusion on the quality of flow recovery by comparing inversions with and without the second term on the right hand side of (5.12). Including tangential magnetic diffusion has improved the inverted flow, by global pattern at about 4.9% (see c values in Table 5.2), and by pointwise correlation at about 3.6% (see p values in Table 5.2).

The choice of the non-dimensional parameter k is mostly affecting the magnitude of the flow (Amit and Olson, 2004), and can be "tuned" to fit best the magnitude of the dynamo flow. I find that the optimized value is $k = 0.07$ (Table 5.2), as the best-fit ratio of tangential

divergence and radial vorticity in numerical dynamos (Olson et al., 2002). Spectral methods "tune" the taper parameter to fit best both the magnitude and the scale of the flow. In contrast to the taper parameter, the choice of k does not degrade my inversion misfits; my inversions contain much smaller misfits than the ones obtained by Rau et al. (2000).

The flow recovery seems to be successful, based on qualitative identification of flow features and global statistics; however, it is important to note that the pointwise flow recovery is very poor. The magnitude of the difference vector $|\vec{u}_h - \vec{u}_h^*|$ is comparable to the magnitude of the dynamo velocity vector $|\vec{u}_h^*|$ itself (see low p values in Table 5.2), and not significantly smaller as might be expected from a residual to a successful fit.

In the second large-scale dynamo case 2, the magnetic Reynolds number is lower than in case 1. Fig. 5.3 shows the radial magnetic field and secular variation of case 2. As in case 1, the magnetic field morphology is dominantly dipolar. Figs. 5.4a and 5.4b show the true dynamo velocity and the inverted velocity, respectively. Because of the lower magnetic Reynolds number, effects of diffusion are much stronger here than in case 1. Indeed, the improvement in the quality of recovery by accounting for tangential magnetic diffusion is remarkable in case 2. For two different snapshots of the same case, 2a and 2b, including tangential magnetic diffusion has improved the the correlation coefficient at about 22.9% and 21.6% respectively (see c values in Table 5.2). The inversions of cases 2a and 2b without tangential magnetic diffusion are less successful than case 1, but with tangential magnetic diffusion the recoveries are comparable.

The quality of the flow recovery is degraded in the equatorial region, where (1) effects of radial magnetic diffusion are large, and (2) my inversion method is weak due to the reversed flux patches in numerical dynamos there. I repeated the calculation of the correlation coefficient, this time excluding the 10° low-latitudes from the integration in (5.15). For example, case 2b with tangential magnetic diffusion has a correlation coefficient of $c = 0.521$. Excluding the band $\pm 10^\circ$ around the equator gives $c = 0.644$ for this case, and

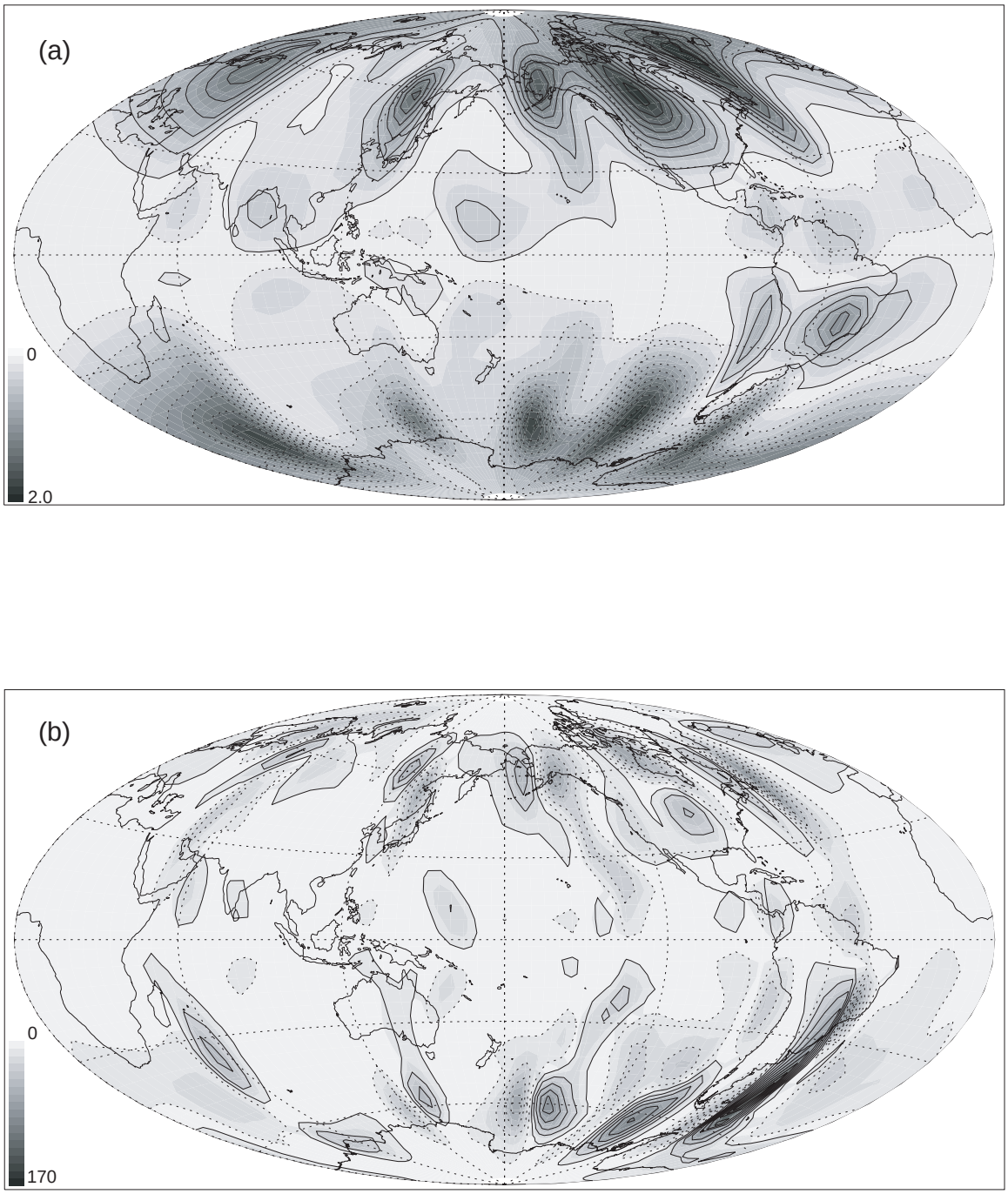

Figure 5.3: Radial magnetic field (a) and secular variation (b) on the outer boundary for case 2. Grey scale represents absolute values, solid lines are positive, dotted lines are negative.

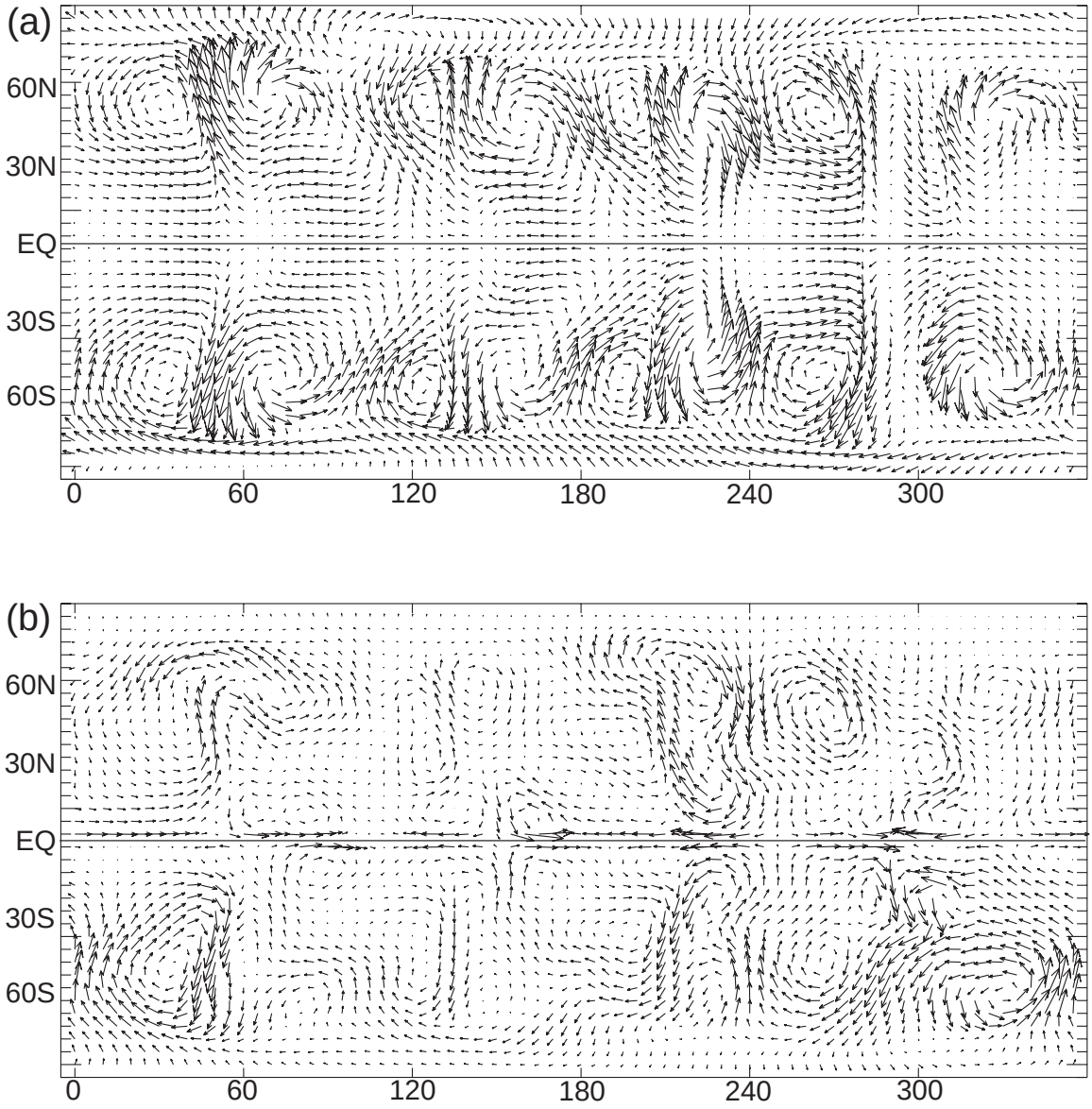

Figure 5.4: Dynamo flow (a) and inverted flow (b) for case 2a with tangential magnetic diffusion. Maximum velocity in (a) is 79.7, and velocity in (b) scales according to (a).

excluding the lowest 30° latitudes gives $c = 0.71$. Clearly, the flow recovery is adequate at high latitudes where most of the intense flow structures are present in the dynamo flow; the recovery is substantially degraded at low-latitudes due to strong radial magnetic diffusion effects, the singularity of the tangential geostrophy, and methodological problems of my inversion there.

Overall, the large-scale properties of the flow are well-recovered, both in magnitude and in pattern. The quality of fit is better in terms of magnitude and comparable in terms of pattern with respect to the quality of fits obtained by Rau et al. (2000). Most main flow features in the dynamo flow are present in the inverted flow at the correct position and with the correct direction of circulation.

5.5.2 Small-scale dynamos

I proceed to describe my results for more complex numerical dynamos. Figs. 5.5 and 5.6 show the radial magnetic field and secular variation of cases 3 and 4, respectively. These cases are characterized by a larger Rayleigh number and a smaller Ekman number than cases 1 and 2 (Table 5.1), resulting in more vigorous convection and stronger rotational effects. In these dynamos the magnetic Reynolds number is larger and smaller-scale magnetic and velocity fields are obtained. On the outer boundary the heat flux is imposed, uniform in case 3 and with a heterogeneous pattern obtained from a lower mantle tomography model (Masters et al., 1996; Olson and Christensen, 2002) in case 4. As in cases 1 and 2, the magnetic field is dominantly dipolar in cases 3 and 4, but is now of much smaller spatial scale (Figs. 5.5 and 5.6). Therefore, I used a finer $2.5^\circ \times 2.5^\circ$ grid for the inversions of cases 3 and 4.

Figs. 5.7 and 5.8 compare the original and inverted velocities for cases 3 and 4, respectively. The statistics of cases 3 and 4 is summarized in Table 5.3. As in cases 1 and 2, including tangential magnetic diffusion improves the quality of the flow pattern - in case 3

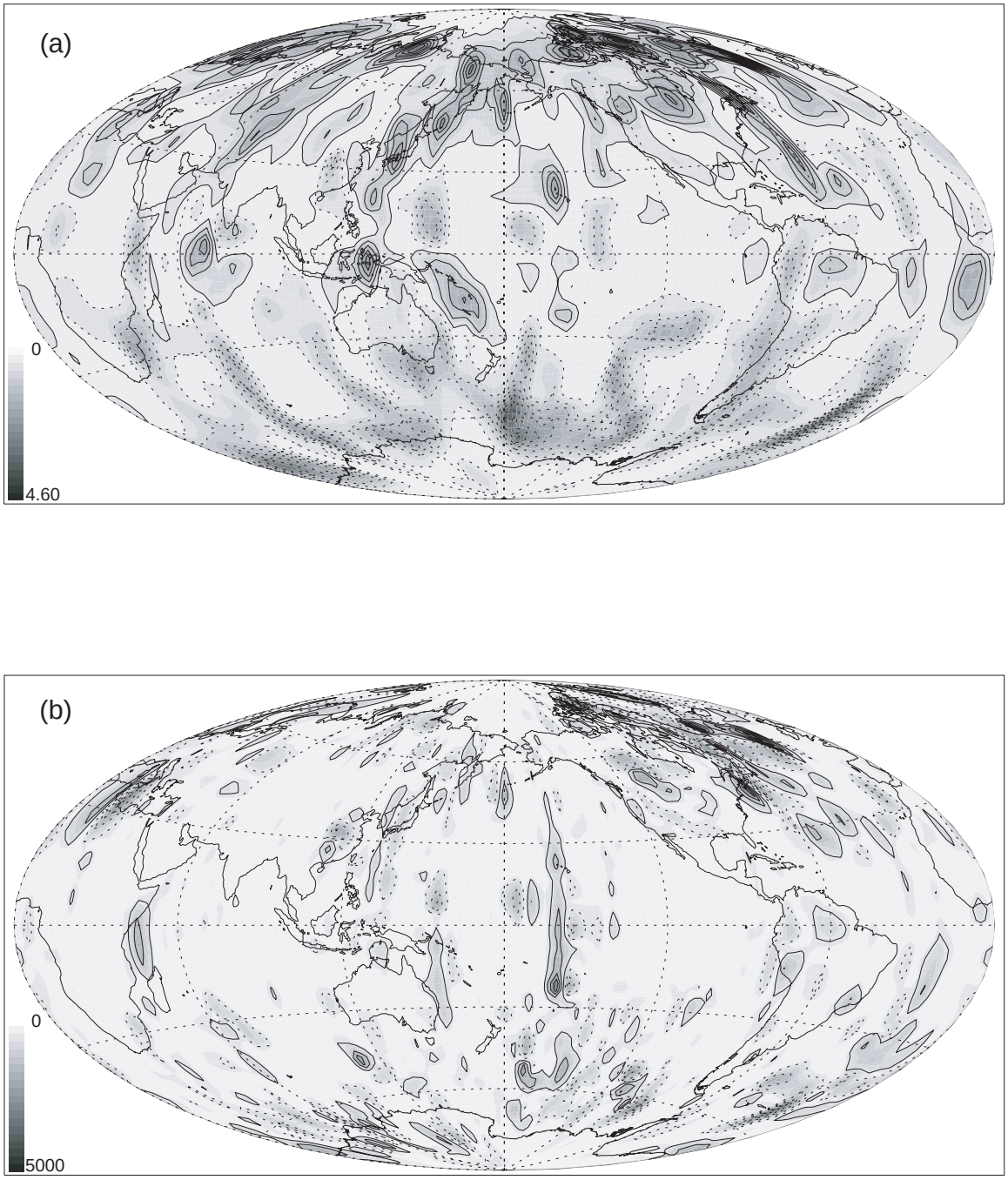

Figure 5.5: Radial magnetic field (a) and secular variation (b) on the outer boundary for case 3. Grey scale represents absolute values, solid lines are positive, dotted lines are negative.

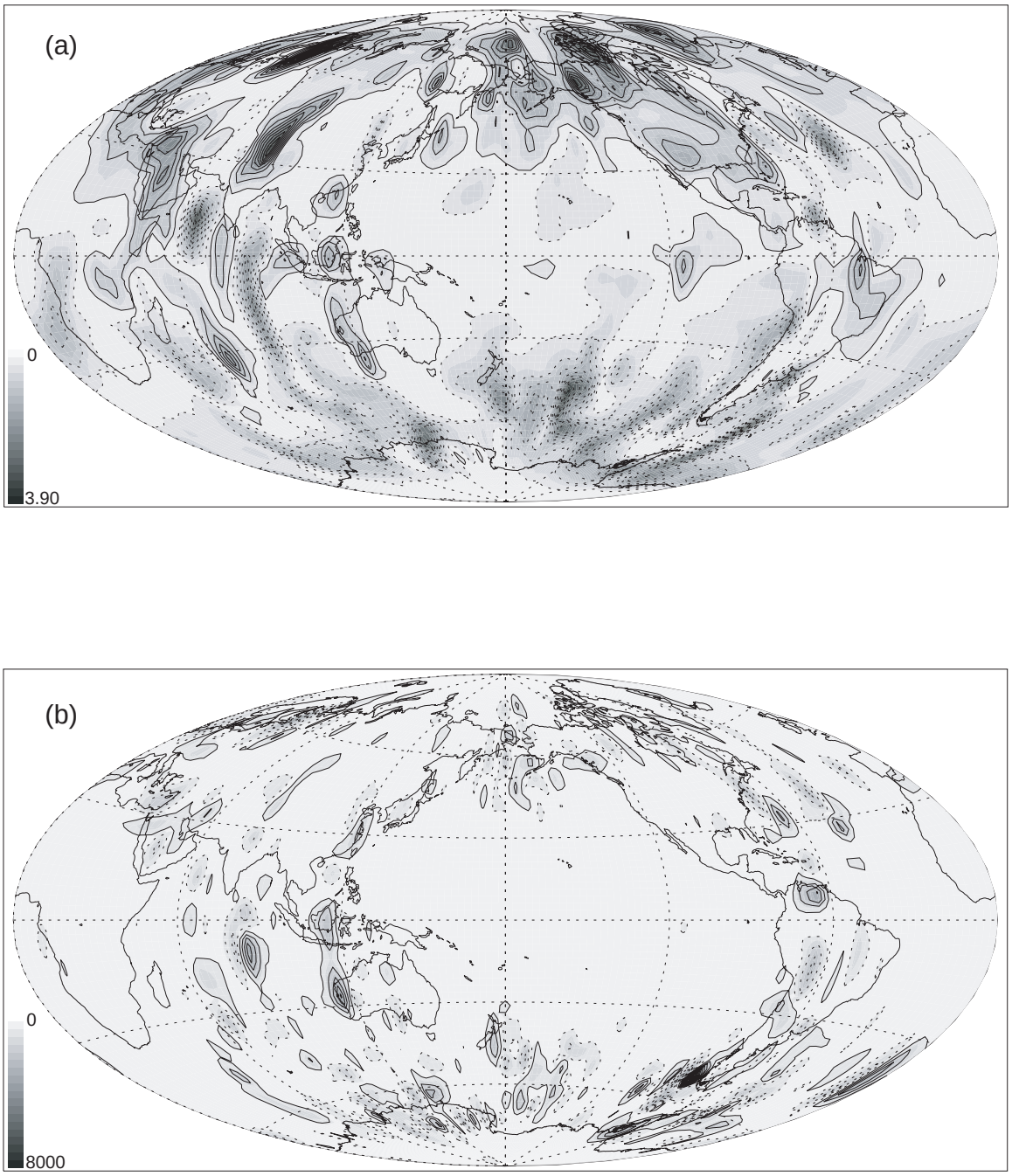

Figure 5.6: Radial magnetic field (a) and secular variation (b) on the outer boundary for case 4. Grey scale represents absolute values, solid lines are positive, dotted lines are negative.

by 2.7% and in case 4 by 2.8% (see c values in Table 5.3). From Table 5.3 it is evident that the qualities of the inversions of cases 3 and 4 are much lower than the quality of the inversions of cases 1 and 2, due to the higher complexity of the dynamos expressed by the finer resolution of the secular variation in cases 3 and 4. A small-scale magnetic field is accompanied by strong local magnetic diffusion effects, which are not well-represented by the magnetic Reynolds number, because the shell thickness is an overestimated length-scale. Some of the diffusive effects may be captured by including tangential magnetic diffusion, but the radial diffusion cannot be modeled without knowledge of the variation of the magnetic field with depth. Therefore, the quality of smaller-scale secular variation inversions is significantly lower.

Case	**k**	$\nabla_h^2 B_r$	$\lvert\vec{u}_h\rvert_m / \lvert\vec{u}_h^*\rvert_m$	$\bar{u_h}/\bar{u_h}^*$	c	c_{ee}	p **%**	M_{sv}	M_{div}
3	0.1	no	1.58	0.97	0.207	0.244	-25.57	1.61	3.44
3f	0.1	no	2.48	1.49	0.197	0.216	-62.20	0.12	4.26
3	0.1	yes	1.53	0.99	0.234	0.275	-24.63	1.87	3.01
4	0.1	no	2.28	1.04	0.072	0.100	-40.67	1.64	3.62
4f	0.1	no	3.94	1.90	-0.014	-0.016	-115.39	2.08	4.20
4	0.1	yes	2.13	1.02	0.100	0.113	-35.98	1.82	3.23

Table 5.3: Statistics of cases 3 and 4. $\vec{u}_h$ is the inverted velocity, $\vec{u}_h^*$ is the true dynamo velocity. $||$ and m denote absolute value and maximum, respectively. $\bar{u}$ denotes the areal-average of $\vec{u}$. f denotes filtered cases. c is the correlation coefficient defined in (5.15), c_{ee} is the same coefficient excluding the 10° latitude band around the equator, p is the pointwise correlation defined in (5.16). M_{sv} and M_{div} are the secular variation and divergence misfits in %, respectively.

The problems of imaging small-scale flow structures are illustrated by the intense flow structure in the inverted flow of case 3 in the equatorial region at about longitude $180E$ (Fig. 5.7b). There is no corresponding structure in the dynamo flow (Fig. 5.7a); however, in the same location there is a significant secular variation structure (Fig. 5.5b). Because the magnetic field there is weak (Fig. 5.5a), tangential magnetic diffusion is not cannot be the major source of secular variation. The radial part of the magnetic diffusion, represented

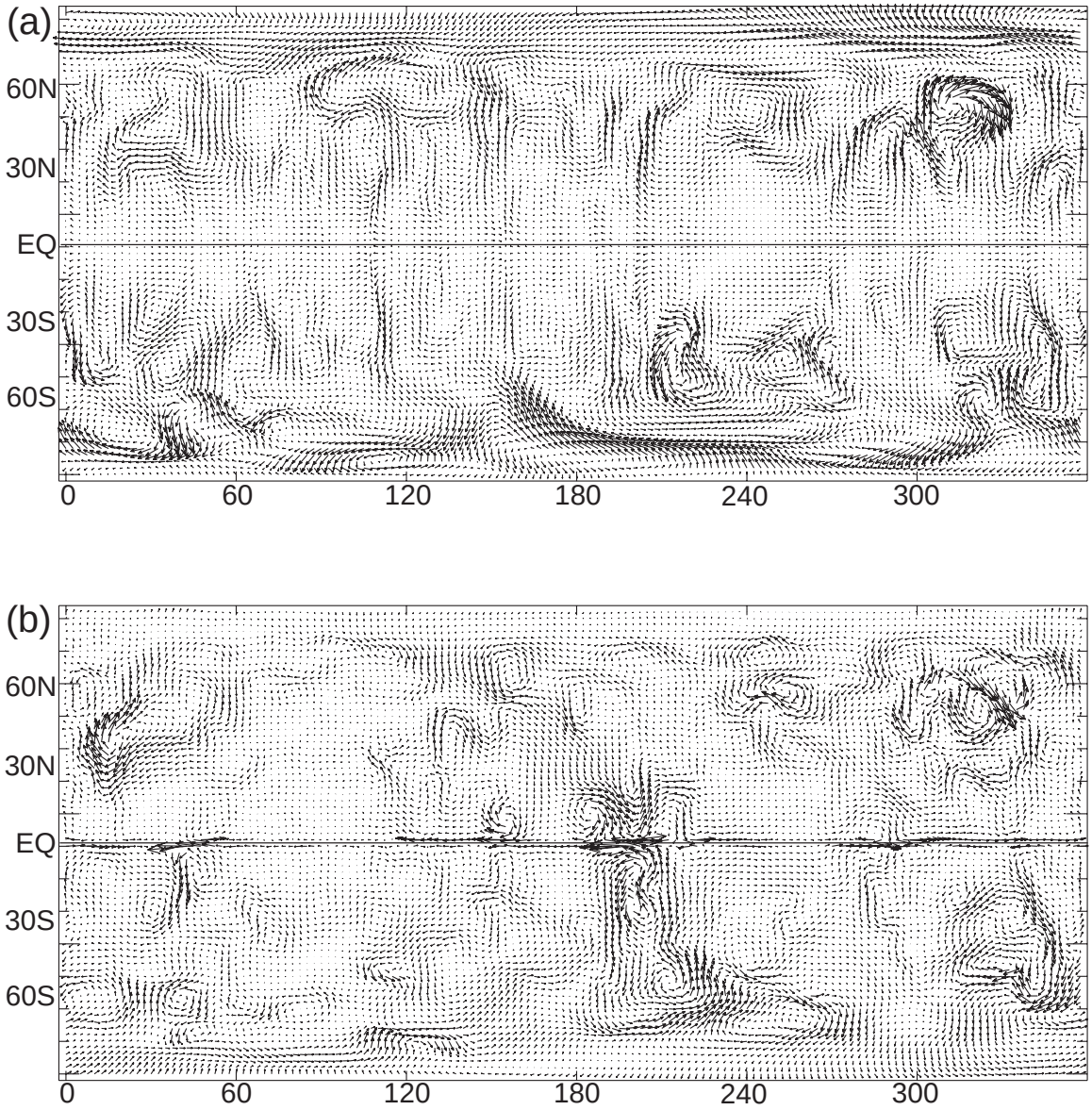

Figure 5.7: Dynamo flow (a) and inverted flow (b) for case 3 with tangential magnetic diffusion. Maximum velocity in (a) is 879.14, and velocity in (b) scales according to (a).

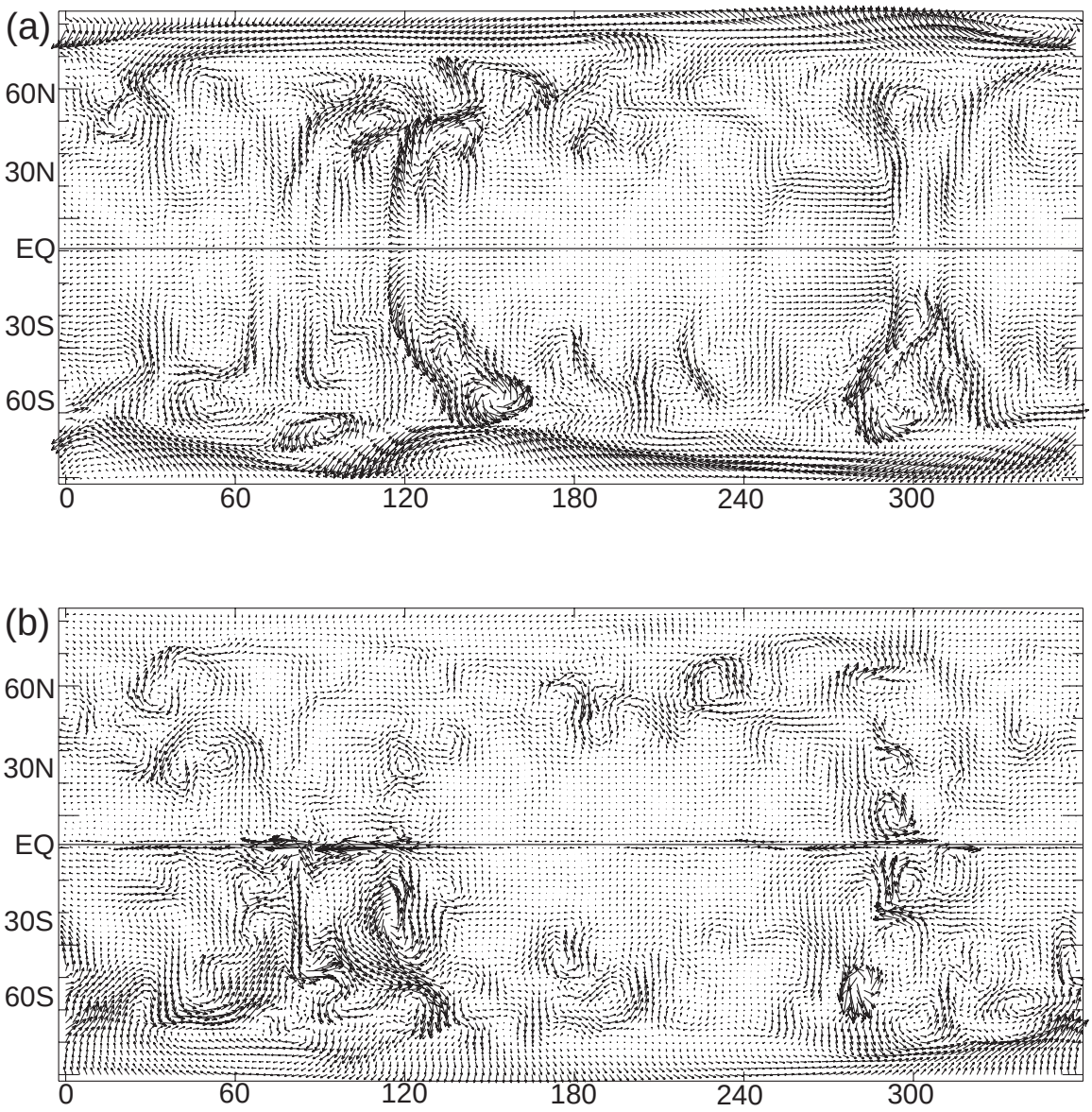

Figure 5.8: Dynamo flow (a) and inverted flow (b) for case 4 with tangential magnetic diffusion. Maximum velocity in (a) is 753.26, and velocity in (b) scales according to (a).

by the first term on the right hand side of (5.10), causes local rapid changes in the radial magnetic field at this area, which results in a severe flow artifact.

Despite the problems of imaging small-scale dynamo flow, case 3 recovers several main flow features. The most intense dynamo flow feature is an anti-cyclonic vortex centered at about $[310E, 45N]$ (Fig. 5.7a). This structure is well-recovered in position and direction of circulation in the inverted flow, and it is one of the most intense flow features (Fig. 5.7b). More examples of successful flow recoveries include an intense cyclonic vortex centered at about $[215E, 50S]$ and equatorially-symmetric poleward jets at about longitude $345E$. The quality of flow recovery in case 4 is even poorer than in case 3, probably because the tomographic boundary conditions induce a more complex smaller-scale flow.

I tested the effects of magnetic field truncation on core flow inversions in cases 3f and 4f. I inverted the same magnetic secular variation of cases 3 and 4, but this time I used a low-pass filter. The filter is a cosine function centered at spherical harmonic degree $l = 12$ with a width $w = 2$, so $l = 10$ is unchanged, $l = 12$ is moderately truncated, and $l \geq 14$ is completely removed. The inverted flow was compared with the dynamo flow filtered in the same way. The statistics of the filtered cases is given in Table 5.3 (cases 3f and 4f). I find that the filtered inversions degrade the quality of the flow recoveries. The same conclusion was reached by Rau et al. (2000).

My small-scale dynamo inversions are less successful in terms of the correlation coefficient in comparison with similar cases inverted by Rau et al. (2000), because of the flexibility of spectral methods in the choice of the taper parameter. This choice selects the trade-off between misfits and flow-scale, and allows for large misfits that absorb magnetic diffusion effects (Rau et al., 2000). These large misfits are useful when the true flow in known, but typically would not be used in geomagnetic secular variation inversions. My method does not apriori selects the flow-scale or the misfits.

Cases 3 and 4 demonstrate that complex flow at low Ekman number and high magnetic

Reynolds number might be not well-resolved by core flow inversions, even when the magnetic field and secular variation is known at small spatial scale. Furthermore, the errors in core flow models due to geomagnetic data truncation may be severe (Hulot et al., 1991). The unmodeled local effects of radial magnetic diffusion are enhanced in small-scale numerical dynamos with vigorous convection, especially in the equatorial region, resulting in flow artifacts. Nevertheless, some main flow features are recovered.

5.6 Discussion

Several problems are associated with core flow inversions. First, the observed geomagnetic data is truncated at spherical harmonic degree ~ 14 to remove the effect of crustal magnetization, and therefore the data does not contain the small-scale core field. Second, most previous core flow models neglected magnetic diffusion due to the large magnetic Reynolds number estimated in the core. However, magnetic Reynolds number based on the outer core radius is may be misleading because the geomagnetic core field may change on much smaller length-scales. Furthermore, frozen-flux tests based on local conservation integrals show that in some regions of the core-mantle boundary, diffusion plays an important role (Bloxham, 1989). Also, the expansion and intensification of reversed flux patches on the core-mantle boundary, especially below the Southern Atlantic Ocean, suggest that magnetic diffusion effects are significant at these regions (Gubbins, 1987; Bloxham et al., 1989; Olson and Amit, 2005). Third, core flow inversions contain non-uniqueness; there is some flow component that does not generate secular variation of its own (Backus, 1968). Various physical assumptions have been used to further constrain the flow and to reduce its non-uniqueness, including steady flow (Voorhies, 1986), pure toroidal flow (Whaler, 1980), and tangential geostrophy (LeMouël, 1984). These assumptions reduce but do not remove non-uniqueness from the inverse problem. In pure toroidal core flow models the

component parallel to B_r-contours is non-unique, whereas in tangential geostrophic models the non-uniqueness is reduced to ambiguous patches that occupy about 40% of the core-mantle boundary (Bloxham and Jackson, 1991). Therefore the non-uniqueness in tangential geostrophy is more restricted than in pure toroidal flow (Backus and LeMouël, 1986), but still the problem remains. Core flow models that assume steady flow are advantageous for their simplicity and were found compatible with the gross secular variation, but cannot account for the observed changes in the length-of-day (Bloxham, 1992; Holme and Whaler, 2001).

The problems of data truncation and unmodeled magnetic diffusion are common to my method and conventional spectral methods. The filtered cases have demonstrated that truncation effects degrade the flow recovery, when compared with filtered flow. At lower magnetic Reynolds number I have demonstrated that accounting for just a part of the diffusion effects, the tangential part, improves significantly the quality of the flow recovery. However, unmodeled effects of radial magnetic diffusion degrade the quality of the flow recovery, especially at the equatorial region.

My method has several conceptual advantages over conventional spectral methods. First, my method does not suffer from non-uniqueness (Amit and Olson, 2004); the helical flow assumption resolves significant field-aligned flow that is in the null-space of the tangential geostrophy or pure toroidal flow assumptions. Second, the trade-off between flow-scale to data misfit in spectral methods leads to large misfits for best-fit recovered flows (Rau et al. 2000), whereas in my method the magnitude of the flow can be "tuned" without damaging the data misfit. Finally, I have demonstrated that including tangential magnetic diffusion significantly improves the quality of flow recovery.

In summary, my inversion method recovers most of the main features of the flow, both in position of flow structures and in direction of circulation. Choice of an appropriate k value resolves the correct magnitude of flow without degrading the inversion misfits. Inclusion

of magnetic diffusion effects in core flow inversion improves the quality of flow pattern. A lack of accurate knowledge about toroidal-poloidal coupling at the top of the core and unmodeled effects of radial diffusion result in some flow artifacts. However, the overall flow pattern is well-recovered. Inversions of high-complexity small-scale secular variation data yield poor core flow recoveries.

Chapter 6

Dynamo mechanisms for rapid magnetic dipole moment changes

6.1 Introduction

Since the advent of geomagnetic intensity measurements, the geomagnetic dipole moment has decreased at an average rate of about 6 % per century. This is approximately 12 times faster than the dipole free decay rate in the core. Rapid dipole moment decrease is significant because it indicates a decrease in the intensity of the geomanetic field, and a sustained decline may indicate instability of the geodynamo. According to the paleomagnetic record, for example, polarity reversals and excursions often begin with a large dipole moment decrease. Linear extrapolation of the present-day decrease predicts that the dipole moment would vanish in about 1650 years. The moment decrease is accompanied by an increase in the intensity and area of reversed magnetic flux patches on the core-mantle boundary, especially in the southern hemisphere.

The magnetic dipole moment vector is an intrinsic property of planetary magnetic fields, and are generally inclined with respect to the planets' spin axes. The geomagnetic

dipole is now tilted about 10.5 degrees from the geographic pole. The North Geomagnetic Pole changed very little between 1900 $(78.6°N)$ and 1960 $(78.5°N)$, then drifted rapidly poleward to $79.5°N$ in 2000.

The high-latitude normal magnetic flux lobes account for most of the positive contributions to the dipole moment. Previous studies argued that the dipole moment decrease is mostly due to the dynamics of the reversed magnetic flux patches, especially in the Southern Atlantic (Bloxham and Gubbin, 1985; Gubbins, 1987; Bloxham et al., 1989). Gubbins (1987) argued that the dipole moment decrease in 1945 is almost entirely due to the intensification of the reversed flux patch below south of Madagascar and the poleward motion of the reversed flux patch below Patagonia. Reversed flux intensification was modeled as expulsion of toroidal magnetic field by fluid upwelling (Bloxham, 1986; Gubbins, 1987; Bloxham et al., 1989; Gubbins, 1996; Christensen and Olson, 2003). Bloxham et al. (1989) argued that despite the overall validity of the frozen-flux approximation, in which magnetic field diffusion is assumed negligible with respect to advection of magnetic field by core flow (Roberts and Scott, 1965), time-dependency of magnetic flux integrals in the Southern Atlantic provide strong evidence for diffusion.

Although previous studies have identified meridional advection and radial diffusion as the main mechanisms of dipole moment decrease (e.g. Gubbins, 1987), their analysis were different in several important respects. First, advective contributions were inferred indirectly from magnetic flux integrals, rather then directly from the interaction between geomagnetic field and core flow models. Second, contributions of normal polarity magnetic flux to dipole moment changes were not considered. Third, the dipole decrease was studied only at a certain year; the analysis at that time might not necessarily represent well the time-dependent dipole moment dynamics. Fourth, the contribution of meridional diffusion was not addressed. Finally, only the dipole moment strength has been analyzed; little attention has been given to the mechanisms that control changes in the geomagnetic tilt.

In this chapter I derive equations for the various mechanisms of magnetic dipole moment change on the core-mantle boundary. I identify and quantify these mechanisms in the core over a period of 90 years, including contributions from normal and reversed magnetic flux patches. I compute mechanisms of geomagnetic dipole moment decrease as well as temporal changes in the geomagnetic tilt. I confirm my geomagnetic interpretation with an analysis of rapid magnetic dipole moment decrease in a numerical dynamo.

The chapter is outlined as follows. In section 2 I review the theory for the rate of change of the magnetic dipole moment vector (Moffatt, 1978; Davidson, 2001), and I expand this theory to derive equations for the rate of change of its axial and equatorial components. I present my results in section 3. The concept of my approach and the geophysical interpretations are discussed in section 4.

6.2 Theory

Previous authors derived equations for the rate of change of the magnetic dipole moment vector on a spherical surface (Moffatt, 1970; Davidson, 2001). Here I expand this derivation for the axial and equatorial components of the dipole moment in terms of the magnetic and velocity fields just below the core-mantle boundary, and discuss the physical meaning of the different terms.

6.2.1 The rate of change of the magnetic dipole moment vector

I begin by reviewing the derivation of Moffatt (1978) for the temporal rate of change of the magnetic dipole moment vector. The dipole moment vector $\vec{m}$ is generally defined as

$$\vec{m} = \frac{1}{2} \int_V \vec{r} \times \vec{J} dV \quad , \tag{6.1}$$

where V is volume of the outer core, $\vec{r}$ is position vector, and $\vec{J}$ is electric current density. The dipole moment vector can also be defined in terms of the magnetic field $\vec{B}$,

$$\vec{m} = \frac{3}{2\mu_0} \int_V \vec{B} dV \ . \tag{6.2}$$

$\mu_0 = 4\pi \cdot 10^{-7}\ N/A^2$ is permeability of free space. The temporal rate of change of the dipole moment vector is therefore

$$\frac{d\vec{m}}{dt} = \frac{3}{2\mu_0} \int_V \frac{\partial \vec{B}}{\partial t} dV \ , \tag{6.3}$$

where t is time. Using Faraday's law, (6.3) can be rewritten as

$$\frac{2\mu_0}{3} \frac{d\vec{m}}{dt} = -\int_V \nabla \times \vec{E} dV = -\int_S \hat{r} \times \vec{E} dS \ , \tag{6.4}$$

where $\vec{E}$ is electric field, $\hat{r}$ is radial unit vector, the spherical surface increment is $dS = R^2 \sin\theta d\theta d\phi$, R is the core's radius, and (r, θ, ϕ) are the spherical coordinates. The electric field can be expressed in terms of the magnetic and velocity fields using Ohm's law for a moving conductor,

$$\vec{E} = -\vec{u} \times \vec{B} + \lambda \nabla \times \vec{B} \ , \tag{6.5}$$

where $\vec{u}$ is the velocity field and λ is the magnetic diffusivity of the fluid. Substituting (6.5) into (6.4) and assuming $u_r|_{cmb} = 0$ gives the rate of change of the dipole moment vector in terms of the magnetic and velocity fields just below the core-mantle boundary (Moffatt, 1970; Davidson, 2001):

$$\frac{2\mu_0}{3} \frac{d\vec{m}}{dt} = \int_S \vec{u} B_r dS - \lambda \int_S \hat{r} \times (\nabla \times \vec{B}) dS \ . \tag{6.6}$$

6.2.2 The rate of change of the *axial* dipole moment

I proceed to derive an expression for the temporal rate of change of the *axial* component (aligned with the rotation axis) of the magnetic dipole moment. The axial magnetic dipole

moment is defined

$$m_z = \frac{3}{2\mu_0}\int_S B_r \cos\theta dS \ . \tag{6.7}$$

The axial component of the first integrand on the right hand side of (6.6) can be written

$$\hat{z}\cdot\vec{u}B_r = u_z B_r = -u_\theta \sin\theta B_r \ , \tag{6.8}$$

where $\hat{z}$ is the axial unit vector, and again I used $u_r|_{cmb} = 0$. The second integrand on the right hand side of (6.6) can be rewritten as

$$\hat{r}\times(\nabla\times\vec{B}) = -\frac{1}{r}[\frac{\partial}{\partial r}(rB_\theta) - \frac{\partial B_r}{\partial\theta}]\hat{\theta} + \frac{1}{r}[\frac{1}{\sin\theta}\frac{\partial B_r}{\partial\phi} - \frac{\partial}{\partial r}(rB_\phi)]\hat{\phi} \ . \tag{6.9}$$

The axial component of (6.9) is then

$$\hat{z}\cdot(\hat{r}\times(\nabla\times\vec{B})) = \frac{\sin\theta}{r}[\frac{\partial}{\partial r}(rB_\theta) - \frac{\partial B_r}{\partial\theta}] \ . \tag{6.10}$$

Substituting (6.7), (6.8) and (6.10) into the axial component of (6.6) yields the expression for the rate of change of the axial dipole moment by three different contributions,

$$\frac{2\mu_0}{3}\frac{dm_z}{dt} = \int_S \frac{\partial B_r}{\partial t}\cos\theta dS = \\ -\int_S u_\theta \sin\theta B_r dS - \int_S \frac{\lambda\sin\theta}{r}\frac{\partial}{\partial r}(rB_\theta)dS + \int_S \frac{\lambda\sin\theta}{r}\frac{\partial B_r}{\partial\theta}dS \ . \tag{6.11}$$

The terms on the right hand side of (6.11) from left to right represent meridional advection, radial diffusion, and meridional diffusion mechanisms of axial dipole moment change, respectively.

The axial dipole moment can be computed from its spherical harmonic representation,

$$m_z = \frac{4\pi a^3}{\mu_0} g_1^0 \ , \tag{6.12}$$

where a is the radius of the Earth, and g_1^0 is the axial dipole Gauss coefficient. The left hand side of (6.11) is then

$$\frac{2\mu_0}{3}\frac{dm_z}{dt} = \frac{2\mu_0}{3}\frac{4\pi a^3}{\mu_0}\frac{dg_1^0}{dt} = \frac{8\pi a^3}{3}\frac{dg_1^0}{dt} \ . \tag{6.13}$$

6.2.3 The rate of change of the *equatorial* dipole moment

Next I derive an expression for the temporal rate of change of the magnetic *equatorial* dipole moment

$$m_e = \frac{3}{2\mu_0}\int_S B_r \sin\theta\cos\phi' dS \ , \tag{6.14}$$

where the equatorial axis points where the equatorial plane intersects the time-dependent longitude line of the magnetic pole $\phi_0(t)$, and $\phi' = \phi - \phi_0$ is the longitudinal distance from the magnetic pole. The equatorial component of the first integrand on the right hand side of (6.6) becomes

$$\hat{e}\cdot\vec{u}B_r = u_e B_r = (\cos\theta\cos\phi' u_\theta - \sin\phi' u_\phi)B_r \ , \tag{6.15}$$

where $\hat{e}$ is the radial cylindrical unit vector, and again I used $u_r|_{cmb} = 0$. The equatorial component of the second integrand on the right hand side of (6.6) is

$$\hat{e}\cdot(\hat{r}\times(\nabla\times\vec{B})) = -\frac{\cos\theta\cos\phi'}{r}[\frac{\partial}{\partial r}(rB_\theta) - \frac{\partial B_r}{\partial\theta}] - \frac{\sin\phi'}{r}[\frac{1}{\sin\theta}\frac{\partial B_r}{\partial\phi} - \frac{\partial}{\partial r}(rB_\phi)] \ . \tag{6.16}$$

Substituting (6.15) and (6.16) into the equatorial component of (6.6) and reorganizing yields the expression for the rate of change of the equatorial dipole moment in terms of three different contributions,

$$\begin{aligned}\frac{2\mu_0}{3}\frac{dm_e}{dt} &= \int_S(\cos\theta\cos\phi' u_\theta - \sin\phi' u_\phi)B_r dS \\ &+ \int_S \frac{\lambda}{r}[\cos\theta\cos\phi'\frac{\partial}{\partial r}(rB_\theta) - \sin\phi'\frac{\partial}{\partial r}(rB_\phi)]dS \\ &+ \int_S \frac{\lambda}{r}[-\cos\theta\cos\phi'\frac{\partial B_r}{\partial\theta} + \frac{\sin\phi'}{\sin\theta}\frac{\partial B_r}{\partial\phi}]dS \ .\end{aligned} \tag{6.17}$$

The terms on the right hand side of (6.17) from left to right represent tangential advection, radial diffusion, and tangential diffusion mechanisms of equatorial dipole moment change, respectively.

The equatorial dipole moment can be computed from its spherical harmonic representation,

$$m_e = \frac{4\pi a^3}{\mu_0}\sqrt{{g_1^1}^2 + {h_1^1}^2} \ , \tag{6.18}$$

where g_1^1 and h_1^1 are the dipole Gauss coefficients in the equatorial plane. The left hand side of (6.17) is then

$$\frac{2\mu_0}{3}\frac{dm_e}{dt} = \frac{2\mu_0}{3}\frac{4\pi a^3}{\mu_0}\frac{d\sqrt{{g_1^1}^2 + {h_1^1}^2}}{dt} = \frac{8\pi a^3}{3}\frac{d\sqrt{{g_1^1}^2 + {h_1^1}^2}}{dt} \ , \tag{6.19}$$

The magnetic dipole tilt θ_0 is defined in terms of the axial and equatorial dipole moment components,

$$\theta_0 = tan^{-1}(\frac{m_e}{m_z}\ ), \tag{6.20}$$

and its temporal rate of change is given by

$$\dot{\theta_0} = \frac{1}{1+(m_e/m_z)^2}[\frac{\dot{m_e}m_z - \dot{m_z}m_e}{m_z^2}] \ , \tag{6.21}$$

where $\dot{x} \equiv dx/dt$. Equation (6.21) allows to compute the contributions of the three mechanisms to magnetic tilt change from the contributions of these mechanisms to the temporal rates of change of the axial (6.11) and equatorial (6.17) dipole moment components.

6.2.4 The zonal drift of the dipole

Next I derive an equation for the zonal drift of the magnetic dipole, by deriving time-evolution equations for the fixed cartesian dipole moment components m_x and m_y, which lie in the equatorial plane along longitudes $0^\circ E$ and $90^\circ E$, respectively. The x and y dipole moment components are defined by

$$m_x = \frac{3}{2\mu_0}\int_S B_r \sin\theta\cos\phi dS \tag{6.22}$$

$$m_y = \frac{3}{2\mu_0}\int_S B_r \sin\theta\sin\phi dS \ . \tag{6.23}$$

The x and y components of the first integrand on the right hand side of (6.6) are

$$\hat{x} \cdot \vec{u} B_r = (\cos\theta \cos\phi u_\theta - \sin\phi u_\phi) B_r \tag{6.24}$$

$$\hat{y} \cdot \vec{u} B_r = (\cos\theta \sin\phi u_\theta + \cos\phi u_\phi) B_r \tag{6.25}$$

where again I used $u_r|_{cmb} = 0$. The x and y-components of the second integrand on the right hand side of (6.6) are

$$\hat{x} \cdot (\hat{r} \times (\nabla \times \vec{B})) = -\frac{\cos\theta\cos\phi}{r}[\frac{\partial}{\partial r}(rB_\theta) - \frac{\partial B_r}{\partial \theta}] - \frac{\sin\phi}{r}[\frac{1}{\sin\theta}\frac{\partial B_r}{\partial \phi} - \frac{\partial}{\partial r}(rB_\phi)] \tag{6.26}$$

$$\hat{y} \cdot (\hat{r} \times (\nabla \times \vec{B})) = -\frac{\cos\theta\sin\phi}{r}[\frac{\partial}{\partial r}(rB_\theta) - \frac{\partial B_r}{\partial \theta}] + \frac{\cos\phi}{r}[\frac{1}{\sin\theta}\frac{\partial B_r}{\partial \phi} - \frac{\partial}{\partial r}(rB_\phi)] \ . \tag{6.27}$$

Substituting (6.24) and (6.26) into the x-component of (6.6) and rearranging yields the expression for the rate of change of m_x,

$$\begin{aligned} \frac{2\mu_0}{3}\frac{dm_x}{dt} &= \int_S (\cos\theta\cos\phi u_\theta - \sin\phi u_\phi) B_r dS \\ &+ \int_S \frac{\lambda}{r}[-\cos\theta\cos\phi\frac{\partial}{\partial r}(rB_\theta) + \sin\phi\frac{\partial}{\partial r}(rB_\phi)]dS \\ &+ \int_S \frac{\lambda}{r}[\cos\theta\cos\phi\frac{\partial B_r}{\partial\theta} - \frac{\sin\phi}{\sin\theta}\frac{\partial B_r}{\partial\phi}]dS \end{aligned} \tag{6.28}$$

and similarly substituting (6.25) and (6.27) into the y-component of (6.6) yields the corresponding expression for the rate of change of m_y,

$$\begin{aligned} \frac{2\mu_0}{3}\frac{dm_y}{dt} &= \int_S (\cos\theta\sin\phi u_\theta + \cos\phi u_\phi) B_r dS \\ &+ \int_S \frac{\lambda}{r}[-\cos\theta\sin\phi\frac{\partial}{\partial r}(rB_\theta) - \cos\phi\frac{\partial}{\partial r}(rB_\phi)]dS \\ &+ \int_S \frac{\lambda}{r}[\cos\theta\sin\phi\frac{\partial B_r}{\partial\theta} + \frac{\cos\phi}{\sin\theta}\frac{\partial B_r}{\partial\phi}]dS \end{aligned} \tag{6.29}$$

The terms on the right hand side of (6.28) and (6.29) from left to right represent tangential advection, radial diffusion, and tangential diffusion mechanisms of changes in the fixed equatorial dipole moment components, respectively.

The x and y-components of the dipole moment in terms of the Gauss coefficients are

$$m_x = \frac{4\pi a^3}{\mu_0} g_1^1 \tag{6.30}$$

$$m_y = \frac{4\pi a^3}{\mu_0} h_1^1 \ . \tag{6.31}$$

The left hand sides of (6.28) and (6.29) are respectively,

$$\frac{2\mu_0}{3}\frac{dm_x}{dt} = \frac{2\mu_0}{3}\frac{4\pi a^3}{\mu_0}\frac{dg_1^1}{dt} = \frac{8\pi a^3}{3}\frac{dg_1^1}{dt} \tag{6.32}$$

$$\frac{2\mu_0}{3}\frac{dm_y}{dt} = \frac{2\mu_0}{3}\frac{4\pi a^3}{\mu_0}\frac{dh_1^1}{dt} = \frac{8\pi a^3}{3}\frac{dh_1^1}{dt} \ . \tag{6.33}$$

The longitude of the dipole is defined in terms of m_x and m_y

$$\phi_0 = tan^{-1}(\frac{m_y}{m_x}) \tag{6.34}$$

and the zonal drift of the dipole is given by

$$\dot{\phi_0} = \frac{1}{1+(m_y/m_x)^2}[\frac{\dot{m_y}m_x - \dot{m_x}m_y}{m_x^2}] \ . \tag{6.35}$$

Equation (6.35) allows to compute the contributions of the three mechanisms to the zonal drift of the magnetic dipole from the contributions of these mechanisms to the temporal rates of change of the x-component (6.28) and y-component (6.29) of the dipole moment.

6.3 Results

6.3.1 Dipole moment change analysis using a geomagnetic field model

Here I analyze models of the geomagnetic field on the core-mantle boundary. All the data prior to 2000 is from the core field model of Bloxham and Jackson (1992), and the data for 2000 is from the Ørsted satellite (Olsen et al., 2000). My goal here is to relate the geomagnetic dipole moment decrease to the growth of reversed flux patches and the changes in the geomagnetic tilt over the last century.

Observations of geomagnetic dipole moment intensity

Fig. 6.1 shows the decrease of the geomagnetic dipole moment intensity over the last century, compared to the theoretical free decay rate for a typical core magnetic diffusivity value of $\lambda = 2$ m^2/sec. From Fig. 6.1 it is clear that the current decrease is significantly more rapid than the expected decrease if the geodynamo ceased. This rapid decrease is accompanied by expansion and intensification of reversed flux patches on the core-mantle boundary. Fig. 6.2 shows the radial magnetic field on the core-mantle boundary in 1900 (a) and 2000 (b). In 1900, intense reversed flux patches appeared mostly below Patagonia, whereas by 2000 these patches are also present below wide areas of the Southern Atlantic, South Africa, and some polar regions in both hemispheres.

The geomagnetic dipole is very axisymmetric, i.e. the axial part constitutes most of the vector intensity. To get an insight for the role of reversed flux patches in geomagnetic dipole moment decrease, I investigate maps of the relative contributions to the axial dipole moment, $B_r \cos\theta$ (Fig. 6.3a), and to its rate of change (Fig. 6.3b), in a given year (I chose 1985 as an example). Positive values in Fig. 6.3a represent positive contributions to the negative dipole moment, i.e. local areas with reversed polarity. Similarly, positive values in Fig. 6.3b represent increase in the negative dipole moment, i.e. local areas which contribute to the decrease in dipole moment intensity. The main contributions to the axial dipole moment originate in high-latitude normal flux lobes at both hemispheres; reversed flux patches, mostly below Patagonia and South Africa, have opposite contributions with respect to the current normal polarity (Fig. 6.3a). However, the relative contributions to the changes in the axial dipole moment (Fig. 6.3b) seems balanced, though the imbalance in this map is large and represents the rapid dipole moment decrease. I integrated numerically the relative contributions of normal (Fig. 6.4a) and reversed (Fig. 6.4b) flux to the axial dipole moment over the last century. Most of the axial dipole moment change originates

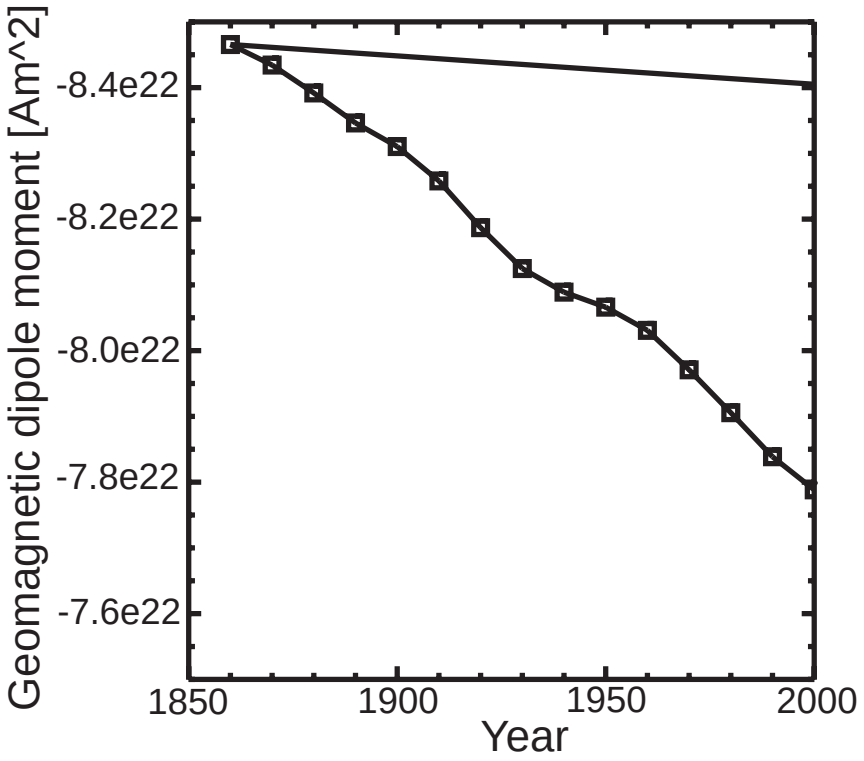

Figure 6.1: Geomagnetic dipole moment intensity over the last century and a half (squares); and theoretical free decay rate in the core assuming magnetic diffusivity of $\lambda = 2$ m^2/sec (solid line).

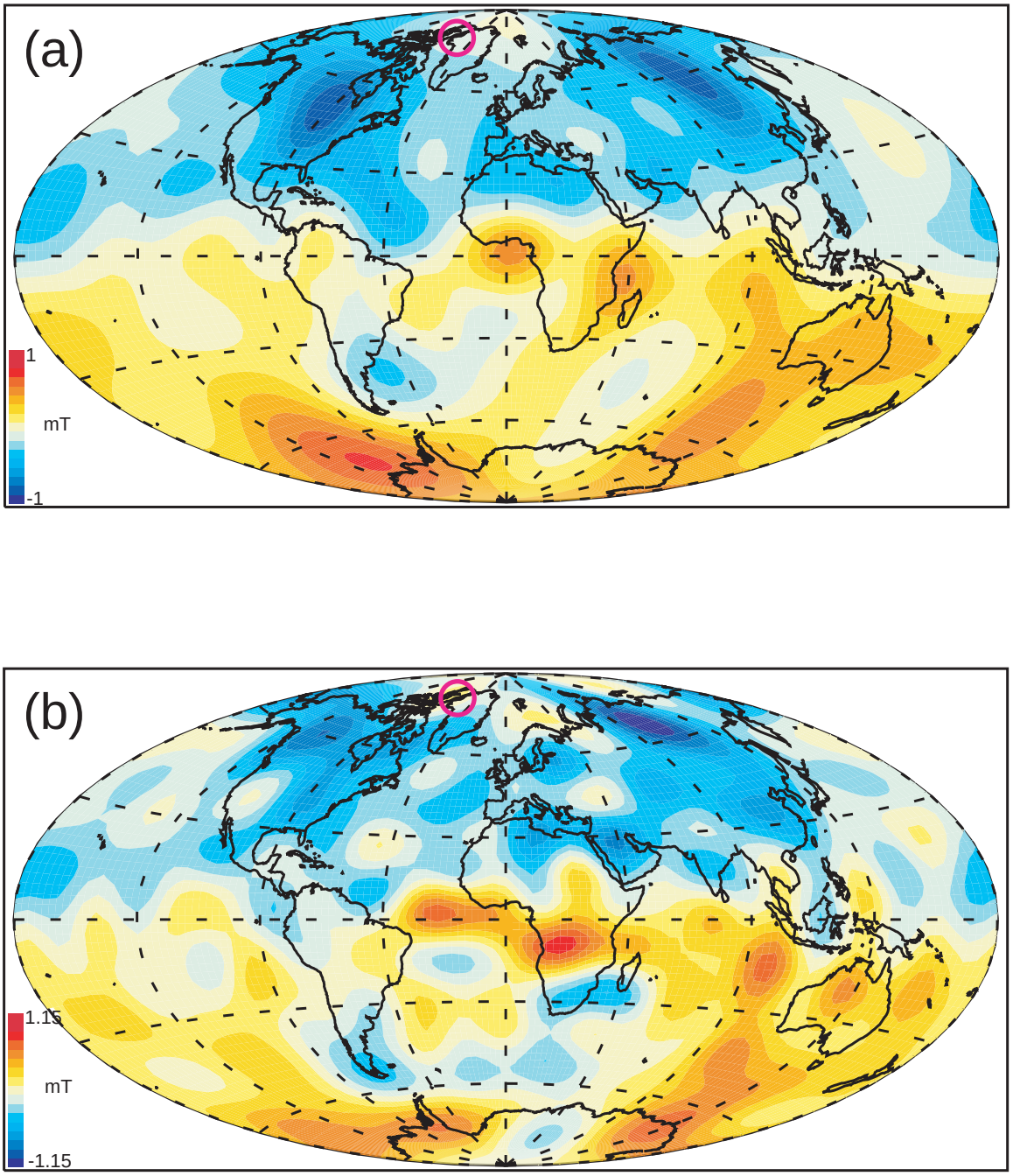

Figure 6.2: Radial magnetic field on the core-mantle boundary in 1900 (a) and 2000 (b). The North Geomagnetic Pole is marked by a circle.

in the southern hemisphere, where reversed flux intensifies and normal flux weakens. In the northern hemisphere, temporal changes are small, and both normal and reversed flux increase their contributions, resulting in cancellation of the overall change there.

Observations of geomagnetic tilt

Fig. 6.5 shows the latitude of the North Geomagnetic Dipole over the last century. In contrast to the monotonic trend in the decrease of the dipole moment intensity (Fig. 6.1), the geomagnetic tilt is nearly constant between 1900-1960, and then drifts poleward until today. The recent poleward drift of the geomagnetic tilt indicates a rapid decrease of the equatorial dipole moment strength.

Fig. 6.6 shows the contributions to the equatorial dipole moment, $B_r \sin\theta \cos\phi'$, in 1900 (a) and 2000 (b). The North Geomagnetic Pole (circled) is located below Northern Canada, and has drifted poleward from about $11.4^\circ N$ in 1900 to $10.5^\circ N$ in 2000. The equatorial dipole (circled) is located below Indonesia, and has drifted westward from $111.3^\circ E$ in 1900 to $108.4^\circ E$ in 2000 (an average rate of about 0.03 °/year). From hereafter I shall refer to eastern/western hemispheres with respect to a dividing longitude $\phi_{div} = \phi_0(t) - \pi/2$, where $\phi_0(t)$ is the time-dependent longitude of the dipole. In the last century the dividing longitude is at about $20^\circ E$. Generally, the equatorial dipole moment receives positive contributions from the southeast and northwest quadrants, and negative contributions from the northeast and southwest quadrants. From Fig. 6.6, significant differences in the contributions to the equatorial dipole moment between 1900 and 2000 appear mostly below southeast of Indonesia (increase), China (decrease), and North America (decrease). A map of the temporal rate of change in the equatorial dipole moment in 1975 is given in Fig. 6.7. Like the axial case (Fig. 6.3b), the imbalance is difficult to detect visually. Fig. 6.8 shows results of numerical integrations of contributions to the equatorial dipole moment over the last century, by flux and by eastern/western hemispheres. Fig. 6.8a indicates that most of

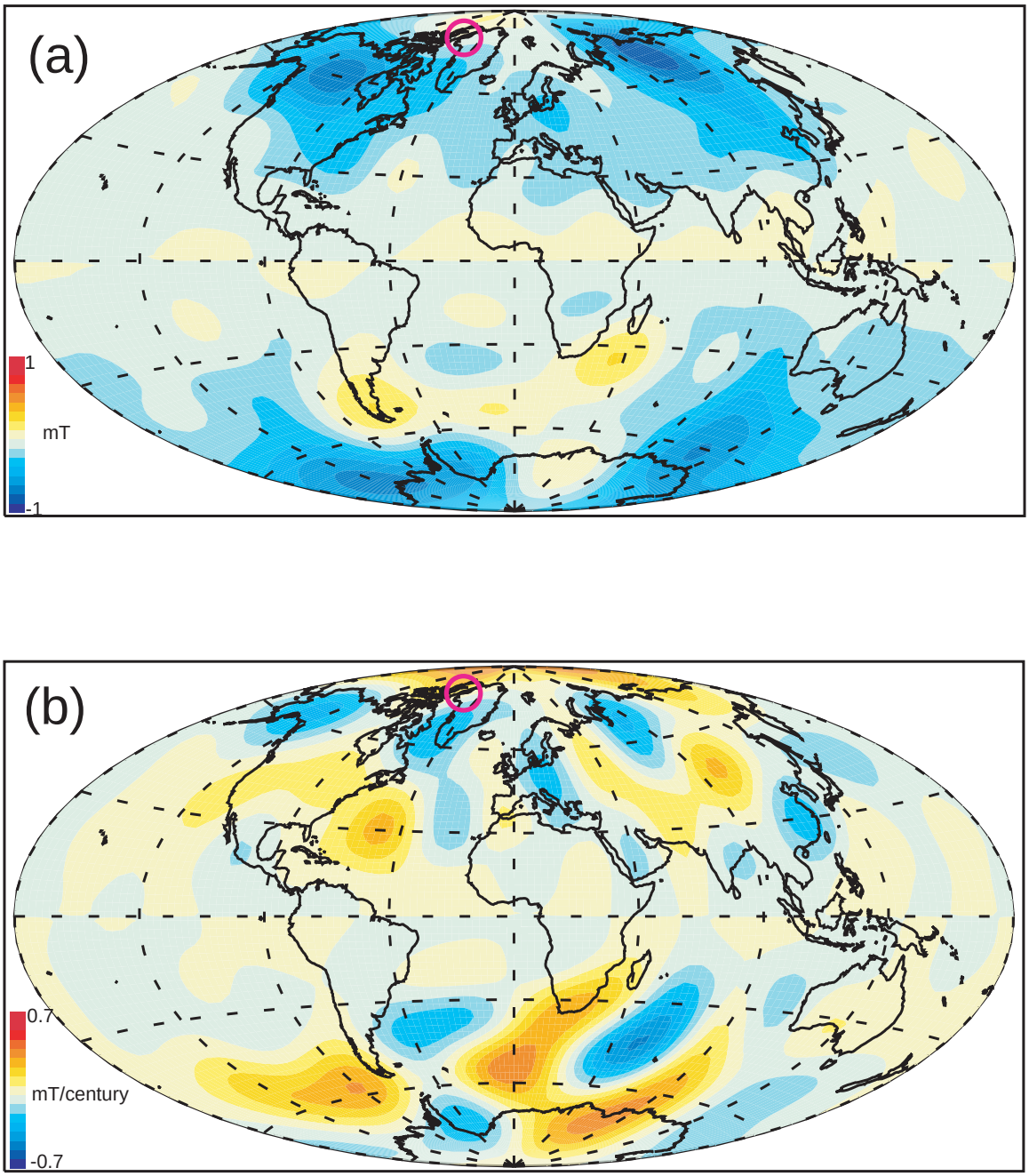

Figure 6.3: Contributions to the geomagnetic axial dipole moment (a) and to its temporal change (b) in 1985. The North Geomagnetic Pole is marked by a circle.

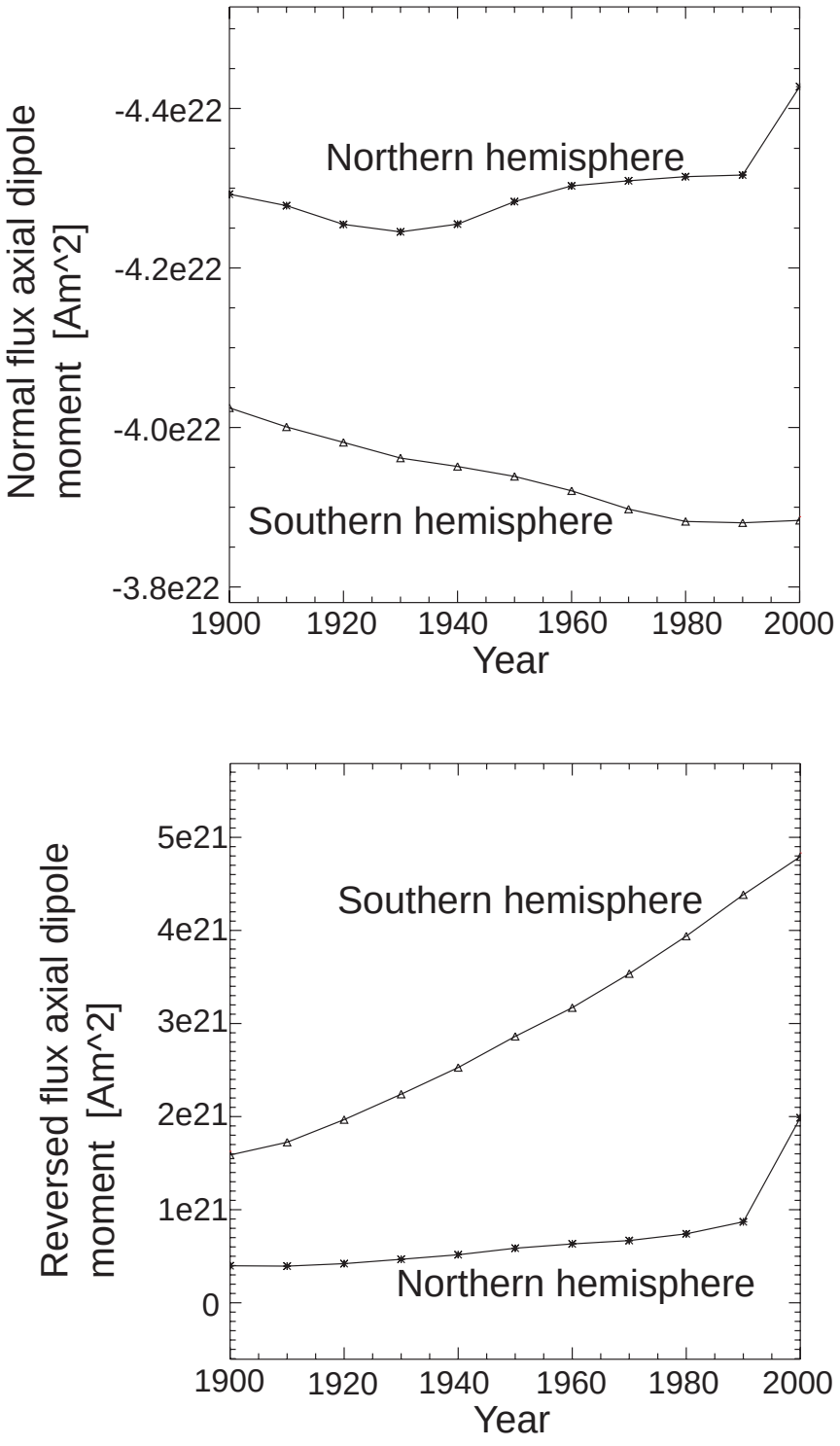

Figure 6.4: Contributions to the geomagnetic axial dipole moment from normal (a) and reversed (b) flux by hemispheres over the last century.

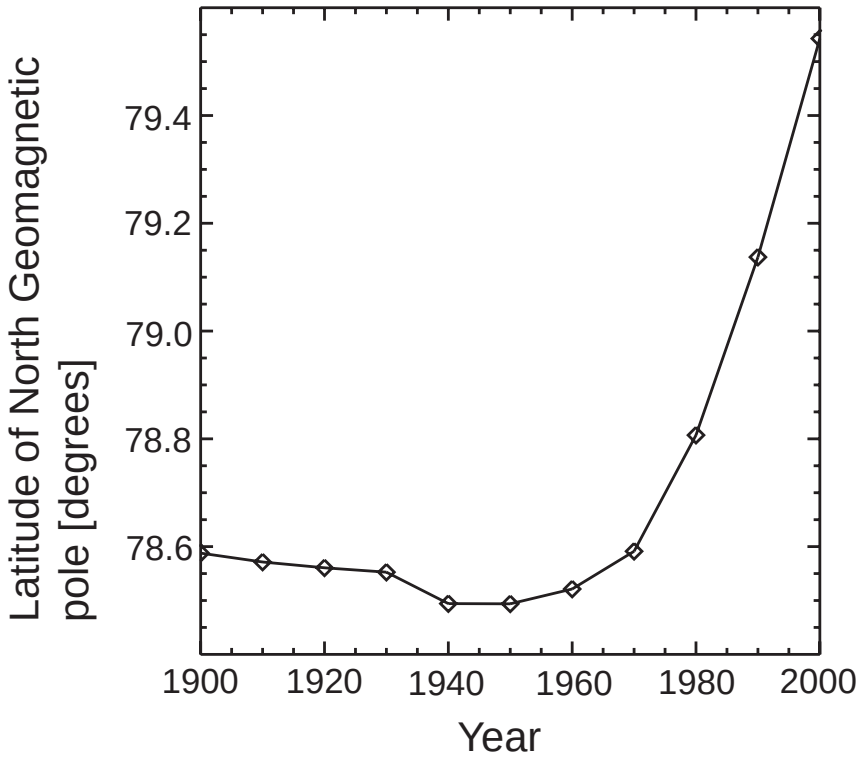

Figure 6.5: Geomagnetic tilt over the last century.

the equatorial dipole moment decrease originates in the western hemisphere. The southeast quadrant has the largest (positive) contribution to the equatorial dipole moment, but the increase in the southeast quadrant is canceled by the increase in the negative contribution from the northeast quadrant (Fig. 6.8b). The decrease in the western hemisphere is due to changes in both flux types (Figs. 6.8a and b).

6.3.2 Analysis of core flow model

The dipole moment equations indicate that temporal changes in the geomagnetic dipole moment can be attributed to three mechanisms: (1) Tangential advection of magnetic flux by core flow just below the core-mantle boundary; (2) radial diffusion of magnetic field from the interior of the core; and (3) tangential diffusion of magnetic flux on the core-mantle boundary. Here I identify and quantify these three mechanisms for the changes in the geomagnetic intensity and tilt over a period of 90 years using the time-dependent core flow model of Amit and Olson (2005). In addition I analyze an event of rapid magnetic dipole moment decrease in a numerical dynamo model. I detect changes in the dipole moment intensity by the axial component, and in the tilt by the equatorial component.

Mechanisms of geomagnetic dipole moment decrease

Fig. 6.9 shows the streamfunction solution for 1985 over the radial magnetic field on the core-mantle boundary for the same year. The contributions to the axial dipole moment rate of change are computed as follows: Total changes are calculated from the geomagnetic data, meridional diffusion contributions are calculated from the geomagnetic data and assuming core magnetic diffusivity of $\lambda = 2$ m^2/sec, meridional advection contributions are calculated from the geomagnetic data and the core flow model, and radial diffusion contributions are calculated as the residuals of the axial dipole moment equation (6.11). The contributions for the changes in the axial dipole moment for 1985 in Am^2/sec are:

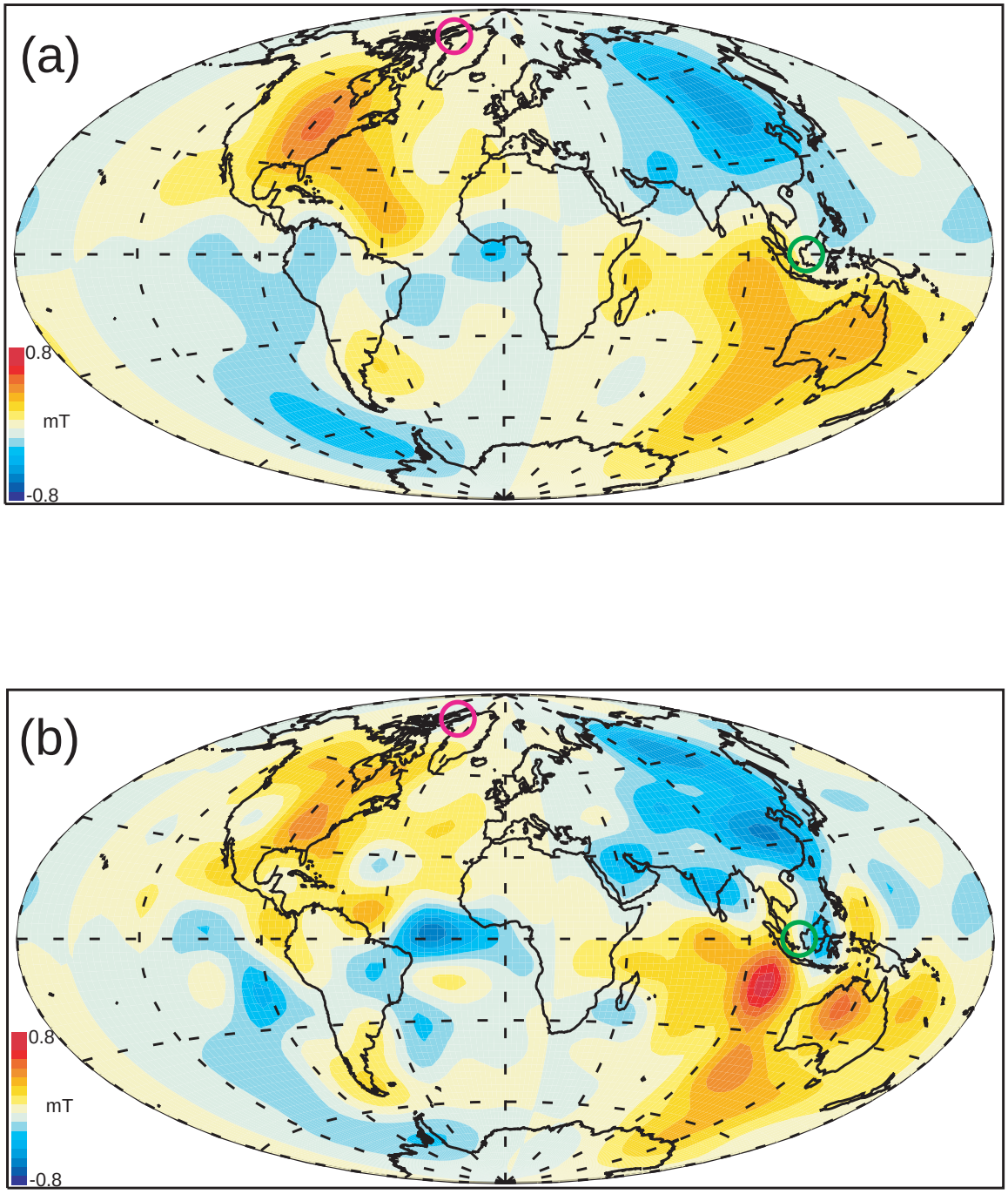

Figure 6.6: Contributions to the geomagnetic equatorial dipole moment in 1900 (a) 2000 (b). The North Geomagnetic Pole and the equatorial dipole axis are marked by circles.

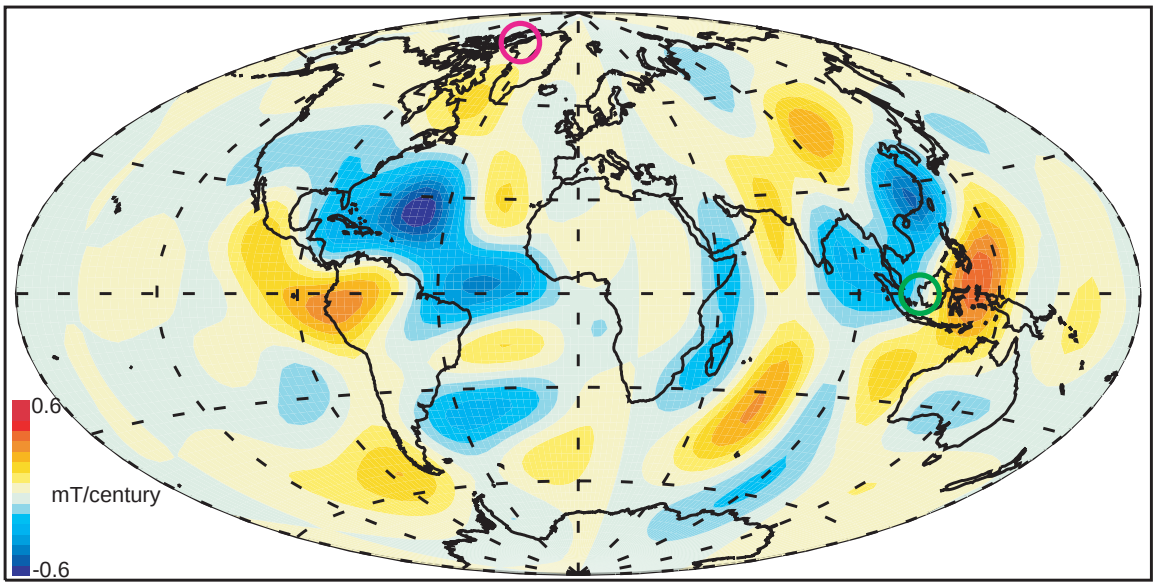

Figure 6.7: Contributions to the temporal change in the equatorial dipole moment in 1975. The North Geomagnetic Pole and the equatorial dipole axis are marked by circles.

Total$= 1.8e12$, meridional advection$= 8.8e11\ (49.0\%)$, radial diffusion$= 8.9e11\ (49.6\%)$, and meridional diffusion $= 2.5e10\ (1.4\%)$. These numerical integrations indicate that meridional advection and radial diffusion have comparable contributions to the axial dipole moment decrease, whereas meridional diffusion is negligible.

To illustrate the action of these two dominant effects, I focus on two regions. Fig. 6.10 shows the full velocities over the radial magnetic field below the South Indian Ocean (a) and south of Madagascar (b). In Fig. 6.10a, a normal flux patch coincides with an equatorward jet, resulting in axial dipole moment decrease by meridional advection. The local contributions for the change in the axial dipole moment below South Indian Ocean in Am^2/sec are: Total$= 1.8e11$, meridional advection$= 3.8e11\ (223.4\%)$, radial diffusion$= -2.0e11\ (-123.8\%)$, and meridional diffusion $= 6.6e8\ (0.4\%)$. In Fig. 6.10b, a reversed flux patch coincides with a westward jet, therefore effects of meridional advection are expected to be small. The contributions of reversed flux only for the change in the axial dipole moment below south of Madagascar in Am^2/sec are: Total$= 1.5e11$, meridional

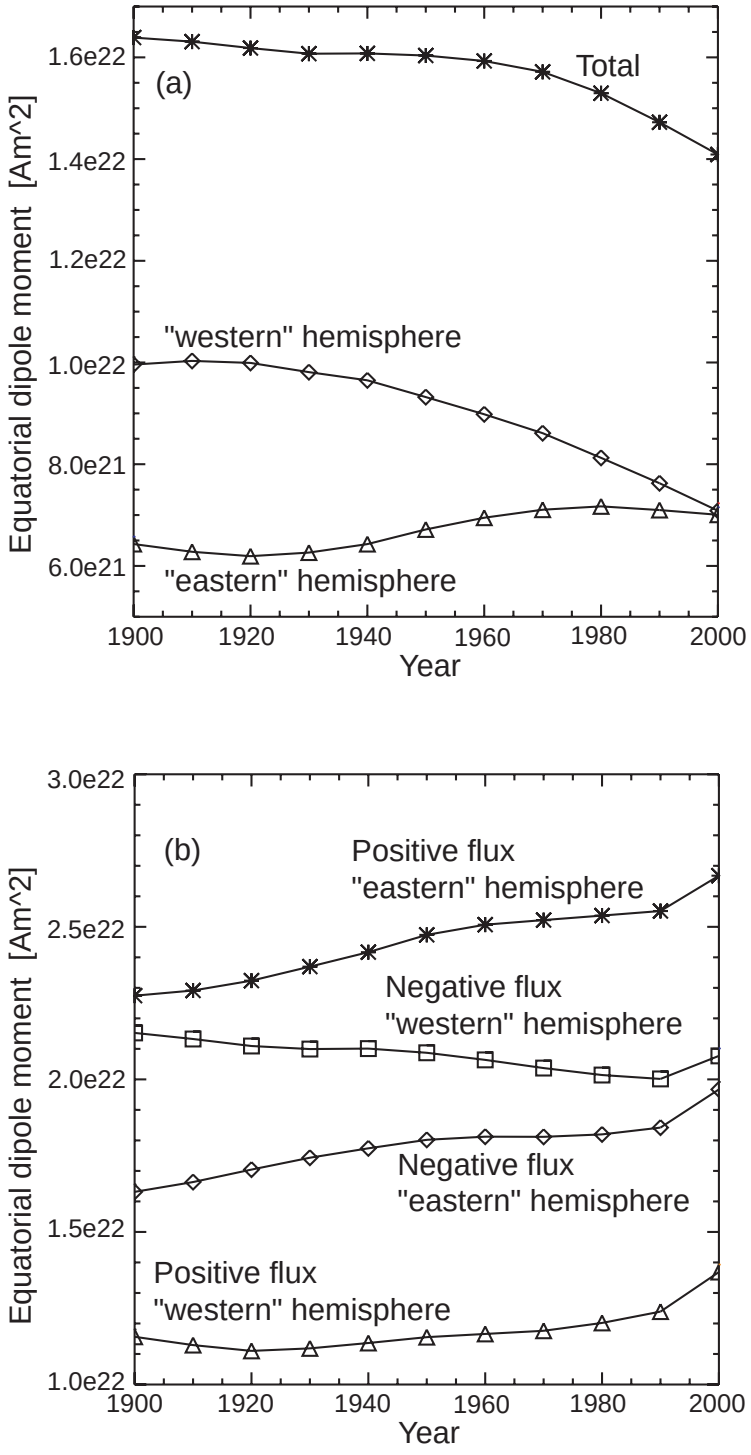

Figure 6.8: Unsigned (absolute) contributions to the equatorial dipole moment over the last century, by eastern/western hemispheres (a), and by flux at each hemisphere (b).

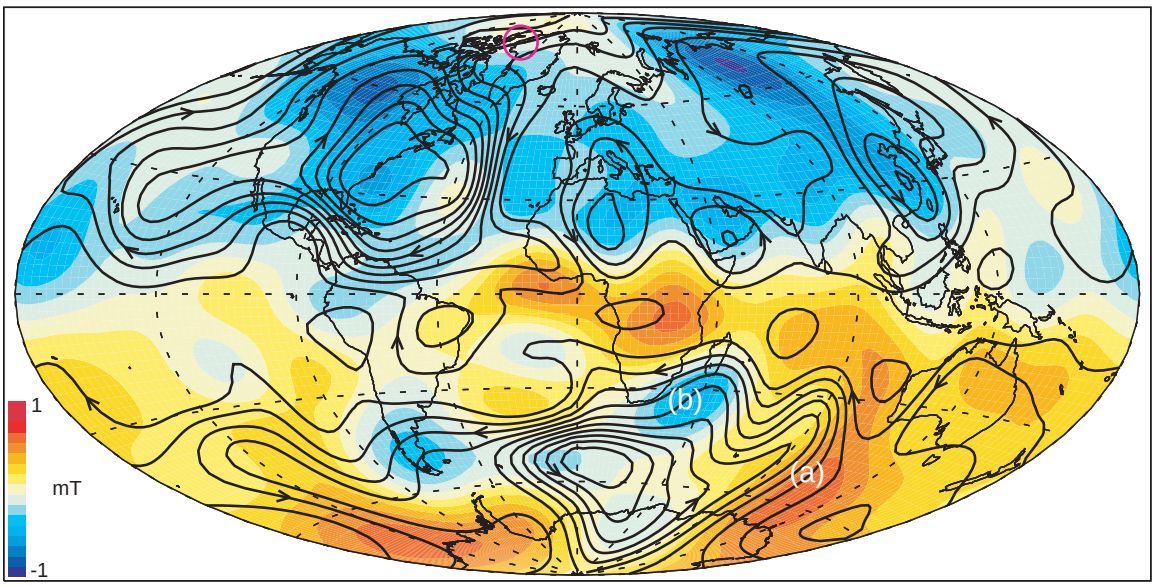

Figure 6.9: Streamlines of a model of fluid flow below the core-mantle boundary and the radial magnetic field on the core-mantle boundary in 1985. The North Geomagnetic Pole is marked by a circle.

advection= $4.2e9$ (3.0%), radial diffusion= $1.5e11$ (97.3%), and meridional diffusion $= -4.9e8$ (-0.3%).

I have repeated this analysis for the period 1895-1985 (Fig. 6.11). The main balance at all times is between meridional advection and radial diffusion, whereas meridional diffusion is always negligible. At the beginning of the studied period and between 1950-1985, meridional advection and radial diffusion are comparable; between 1910-1945 meridional advection is dominant.

Mechanisms of geomagnetic tilt changes

Next I perform the analysis for the equatorial dipole moment, to study the dynamics of the geomagnetic tilt. Fig. 6.12 shows the streamfunction solution for 1975 plotted over the radial magnetic field on the core-mantle boundary for the same year. The contributions to the equatorial dipole moment rate of change are computed in the same way as for

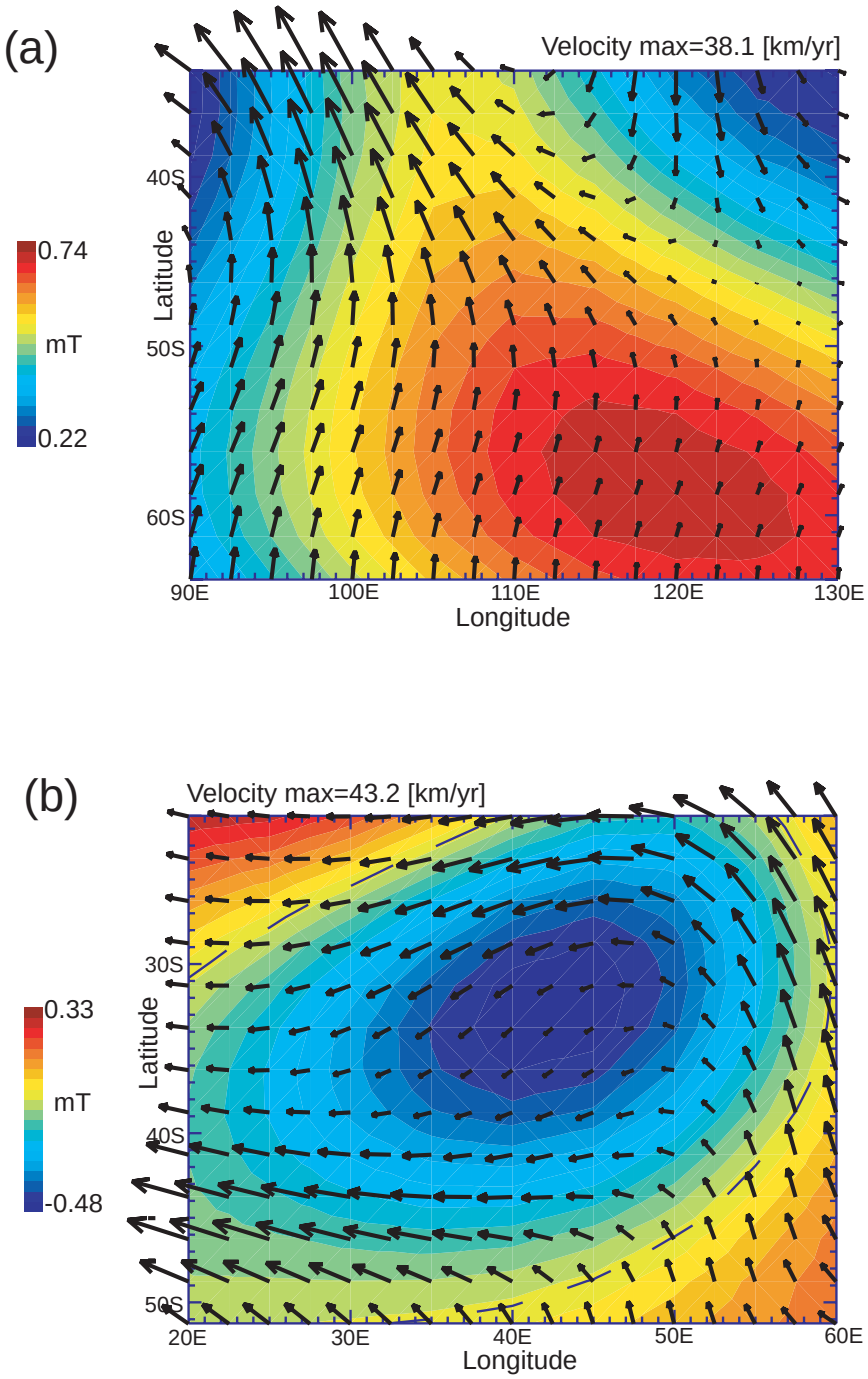

Figure 6.10: Core flow model and the radial magnetic field below the South Indian Ocean (a) and south of Madagascar (b).

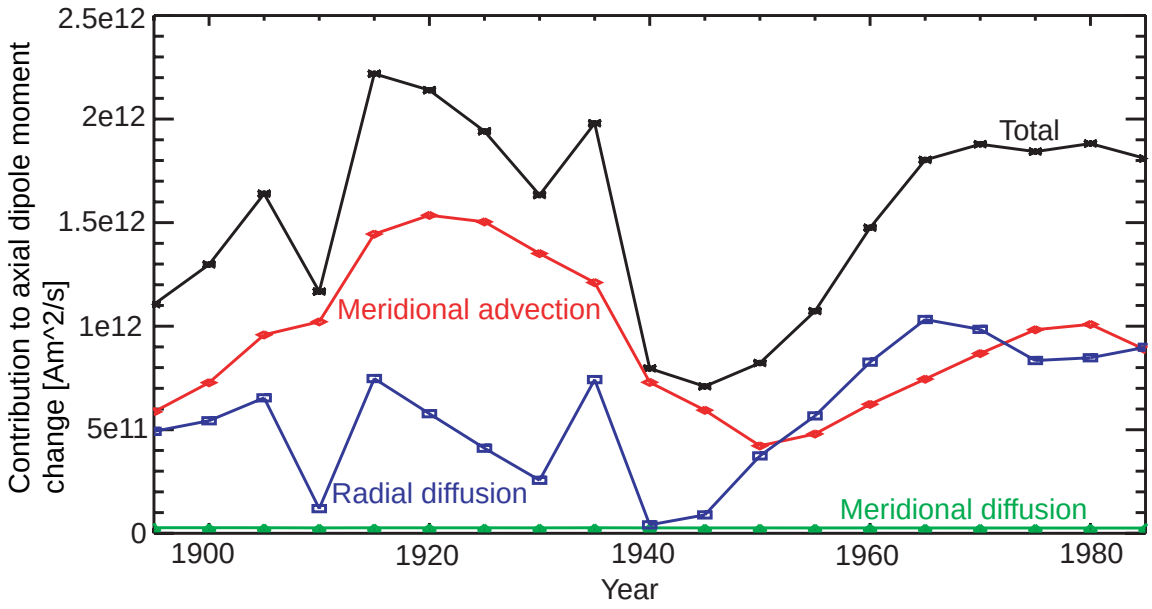

Figure 6.11: Contributions of meridional advection, radial diffusion, and meridional diffusion to the decrease in the geomagnetic axial dipole moment, 1895-1985.

the axial component, this time using the equatorial dipole moment equation (6.17). The contributions for the change in the equatorial dipole moment for 1975 in Am^2/sec are: Total$= -1.33e12$, tangential advection$= -4.76e11$ (35.7%), radial diffusion$= -8.53e11$ (63.9%), and tangential diffusion $= -5.29e9$ (0.4%). As in the axial case, advection and radial diffusion are dominant in the equatorial dipole moment decrease, whereas tangential diffusion is negligible.

Fig. 6.13 shows the relative contributions of the three mechanisms to the change in the equatorial dipole moment for the period 1895-1985. Between 1895-1960 tangential advection and radial diffusion counteract each other, resulting in very little change in the equatorial dipole moment, and the geomagnetic tilt is almost constant (Fig. 6.5). However, between 1965-1985 tangential advection and radial diffusion act in unison, resulting in the decrease of the equatorial dipole moment, and the recent poleward drift of the dipole (Fig. 6.5).

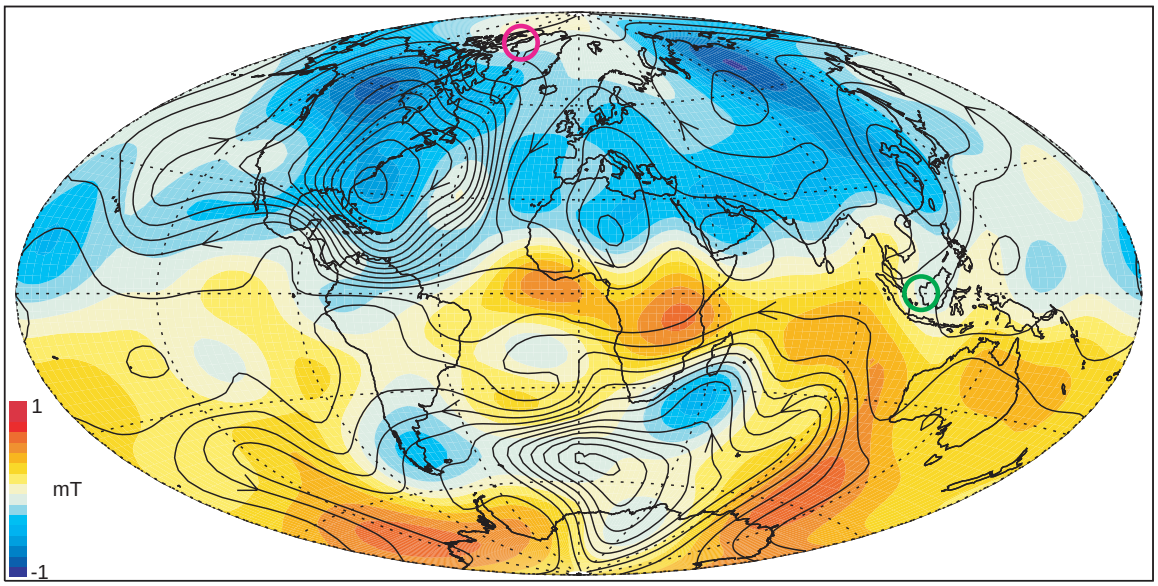

Figure 6.12: Streamlines of a model of fluid flow below the core-mantle boundary and the radial magnetic field on the core-mantle boundary in 1975. The North Geomagnetic Pole and the equatorial dipole are marked by circles.

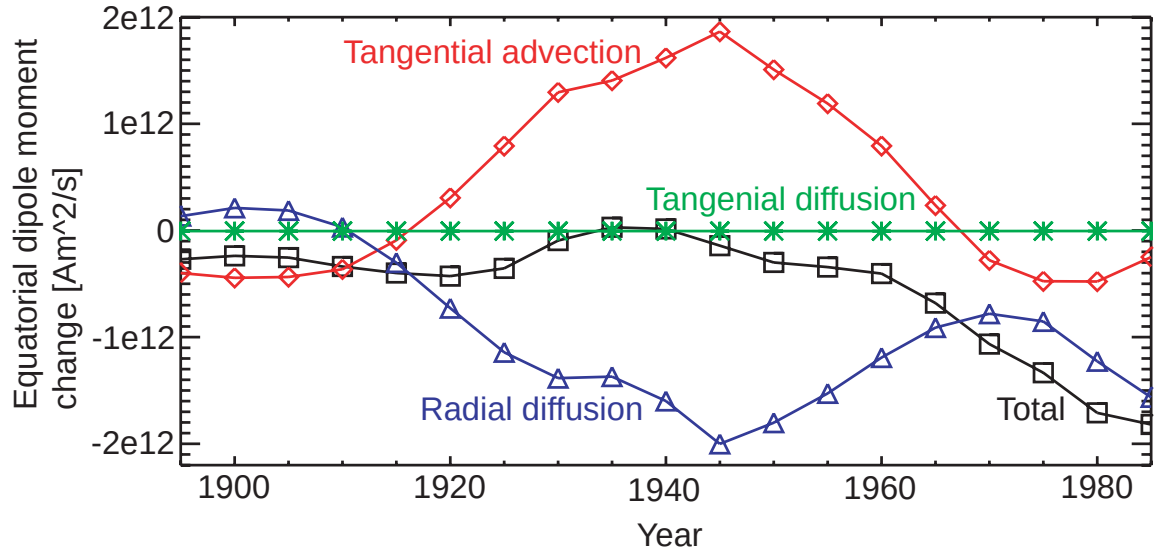

Figure 6.13: Contributions of tangential advection, radial diffusion, and tangential diffusion to the change in the geomagnetic equatorial dipole moment, 1895-1985.

Mechanisms of magnetic dipole moment decrease in a numerical dynamo

I repeat my analysis of the time-evolution dipole moment equation for an event of rapid axial magnetic dipole moment decrease in a numerical dynamo model. This particular numerical dynamo models magnetic field generation by thermal convection in an electrically conducting fluid in a spherical shell (Olson et al., 1999). Here I use rigid boundaries with fixed temperatures, and the regions outside the fluid shell are perfect insulators. The control parameters of the simulation are given in Table 6.1. In order to analyze a dynamo with Earth-like dipole moment dynamics, I chose a dominantly-dipolar numerical dynamo. This dynamo does not exhibit polarity reversals, and the magnetic dipole tilt is very small. Therefore this model is appropriate for analyzing the axial dipole moment change, but not the equatorial part.

Symbol	**Number**	**Ratio**	**Value**
Ra	Rayleigh	Convecting/retarding forces	6.5E5
Ek	Ekman	Viscous/Coriolis forces	4E-4
Pr	Prandtl	Viscous/thermal diffusivities	1
Pm	Magnetic Prandtl	Viscous/magnetic diffusivities	5

Table 6.1: Control parameters in the numerical dynamo.

It is important to emphasize that the calculation of the contributions to the axial dipole moment change is more complete than the calculation in the geomagnetic case. First, radial diffusion can be calculated directly because all magnetic field components and their radial derivatives are known. Second, magnetic diffusivity is known a priori. Third, the depth in which the calculation should be applied is not trivial.

Fig. 6.14 shows timeseries of the axial magnetic dipole moment (a) and its temporal rate of change (b) from a numerical dynamo. The dashed vertical line indicates the time of the rapid dipole decrease event that I focus on here. Although this dynamo does not reverse, the dipole moment fluctuates significantly (Fig. 6.14a). The dimensionless time in

Fig. 6.14a is related to dimensional time by $\tau_\nu = (D^2/\lambda)Pm^{-1}$, where D is the outer core thickness, $Pm = \nu/\lambda$ is the magnetic Prandtl number, and ν is the kinematic viscosity. In Fig. 6.14b I converted to dimensional time assuming a core magnetic diffusivity of $\lambda = 2$ m^2/sec. The numerical dynamo dipole moment decreases at a rate of about 1.6% per century, about 4 times slower than the current geomagnetic dipole moment decrease. Fig. 6.14c shows low-pass filtered timeseries of the axial magnetic dipole moment and the kinetic energy modes $m = 3$ and $m = 4$. Changes in the axial magnetic dipole moment are overall related to vascillations in flow structures between $m = 3$ and $m = 4$.

Fig. 6.15 shows images of the dynamo near the outer boundary at the time of the dipole decrease event. The radial magnetic field on the outer boundary is dominantly dipolar, with earth-like intense high-latitude normal flux lobes (Fig. 6.15a). A pair of intense reversed flux patches elongated meridionally is present at low-latitudes. I found that reversed flux patches are present at times of strong dipole moment; when the dipole moment weakens, the reversed flux patches disappear, and it is the weakening of the normal flux lobes that accounts for most of the dipole moment decrease. The radial velocity below the outer boundary is organized in coloumns (Fig. 6.15b). The Northern hemisphere reversed flux patch coincides with a margin between upwelling and downwelling coloumns, whereas the Southern hemisphere patch coincides with a downwelling. I expect reversed flux patches to emerge by fluid upwelling and intensify by downwelling. High heat flux is mostly concentrated at equatorial regions (Fig. 6.15c). Fig. 6.16 shows zonal profiles at the same time. The zonal velocity profile (Fig. 6.16a) inside the tangent cylinder is dominated by polar upwelling, intense westward polar vortices, and downelling at the tangent cylinder margin that concentrates the magnetic field there. Outside the tangent cylinder the zonal flow is mostly westward and weaker, with eastward flow at high-latitudes. Similar core flow features were found in analysis of geomagnetic field models, core flow inversions, and numerical dynamos (Jault et al., 1988; Olson and Aurnou, 1999; Olson et al., 1999;

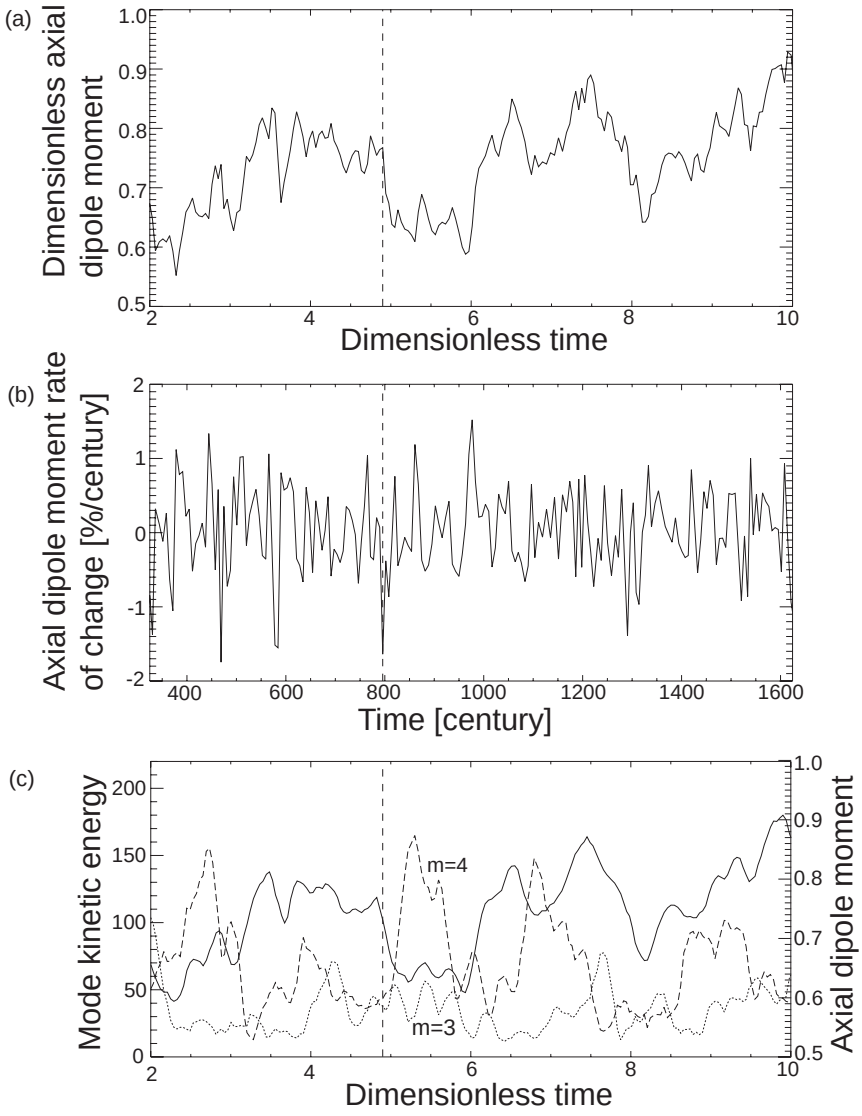

Figure 6.14: Numerical dynamo timeseries of the axial magnetic dipole moment (a), its temporal rate of change (b), and low-pass filtered axial magnetic dipole moment and kinetic energy modes $m = 3$ and $m = 4$ (c). The dashed vertical line indicates the time of the rapid magnetic dipole moment decrease event.

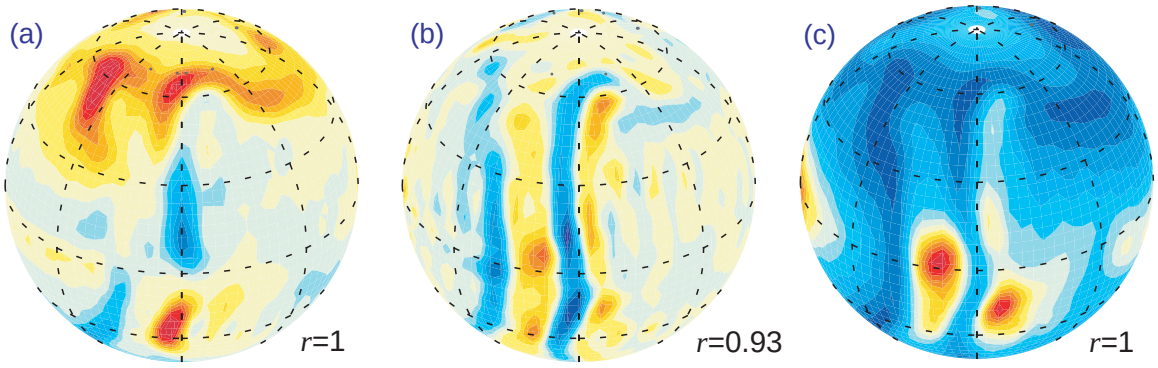

Figure 6.15: Snapshots of the dynamo near the outer boundary at the time of the magnetic dipole moment decrease event. Radial magnetic field on the outer boundary (a), radial velocity below the outer boundary (b), and heat flux on the outer boundary (c).

Hulot et al., 2002; Amit and Olson, 2005; Aubert, 2005). The relations between axial magnetic dipole moment, meridional circulation, zonal electric currents, and magnetic field are illustrated schematically in Fig. 6.16c. Initial dipolar magnetic field lines (right hand side of Fig. 6.16c) are advected by upwellings in polar (Fig. 6.16a) and equatorial (Fig. 6.15c) regions, resulting in bending of magnetic field lines to produce reversed (westward) zonal electric currents, which decrease the axial magnetic dipole moment (6.1). Note that reversed magnetic flux patches on the outer boundary in the are actually associated with positive electric currents.

I integrated numerically the contributions of meridional advection, radial diffusion, and meridional diffusion to the axial magnetic dipole moment changes during the rapid decrease event. Here the contribution of radial diffusion is directly computed from knowledge of all magnetic field components and their radial derivatives. Magnetic diffusivity is also accurately known. The depth-dependent contributions are given in Fig. 6.17. Magnetic diffusion effects are more pronounced in numerical dynamos because of the smaller-scale magnetic field. Therefore, the contribution of meridional diffusion is larger here than in the geomagnetic analysis (Fig. 6.11) by an order of magnitude. Nevertheless, the contribu-

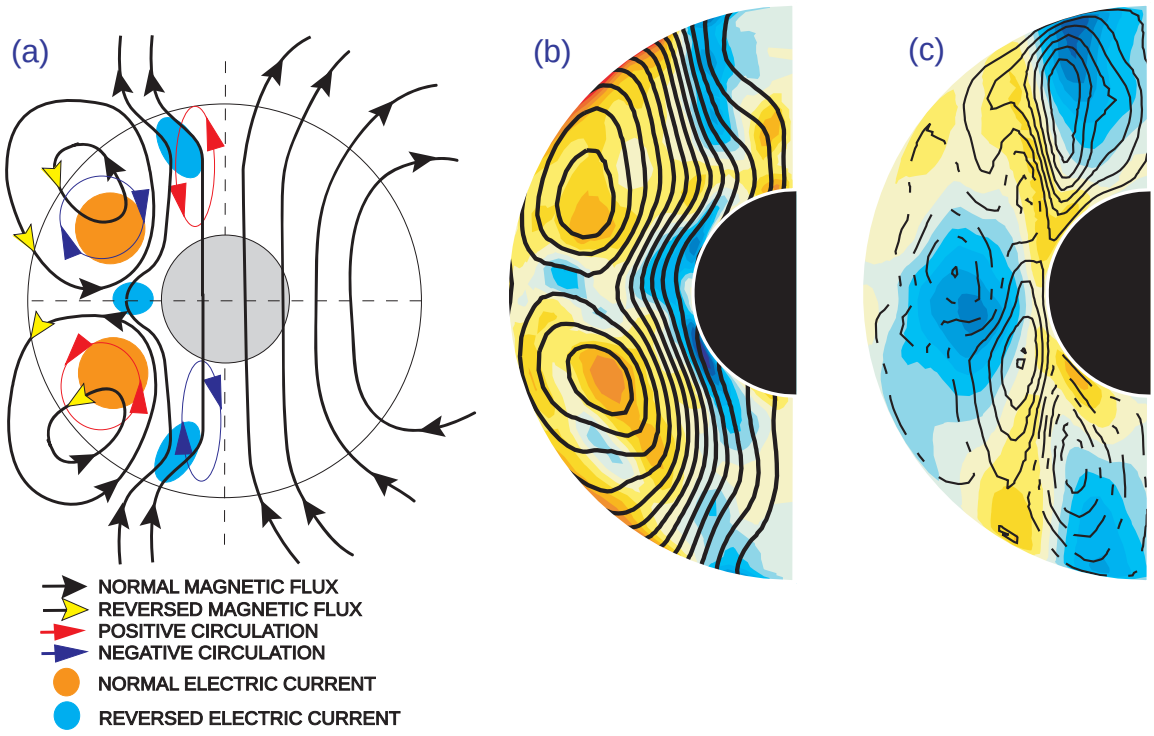

Figure 6.16: Zonal velocity (a) and magnetic field and electric current (b) profiles of the dynamo at the time of the magnetic dipole moment decrease event, and schematic illustration (c).

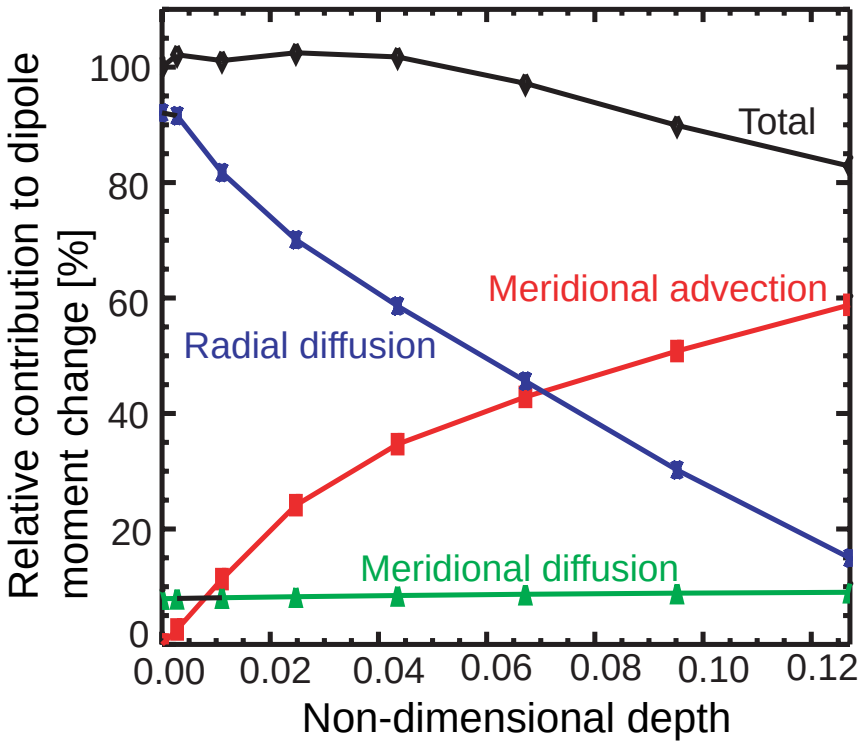

Figure 6.17: Relative contributions (in $\%$) of meridional advection, radial diffusion, and meridional diffusion to the decrease in the magnetic axial dipole moment in a numerical dynamo.

tion of meridional diffusion is still secondary. The main balance, like in the geomagnetic analysis, is between meridional advection and radial diffusion. On the outer boundary, advection is identically zero. Far from the boundary, meridional advection is dominant, but the dipole moment equation that assumes zero radial velocity (near boundary approximation) loses its validity. At a depth of $0.06D$ (about $3h_{ek}$ where h_{ek} is the thickness of the viscous boundary layer) the total axial magnetic dipole moment change departs from a constant value, suggesting that this depth represents well the top of the "free stream". At that depth, meridional advection and radial diffusion are comparable. I conclude that in the numerical dynamo studied, the contribution of radial diffusion is either larger or comparable to the contribution of meridional advection.

6.4 Discussion

6.4.1 Concept

In this study, I make two important non-trivial statements. First, although most of the geomagnetic secular variation is caused by advection, diffusive effects play an important role in geomagnetic dipole moment changes. Second, although local magnetic diffusion effects might contaminate core flow inversions and lead to flow artifacts, global dipole diffusion cannot be mimicked by advection. Since these two arguments are crucial in my approach, I will elaborate on them.

The magnetic Reynolds number in the core is estimated to be ~ 500 (e.g. Amit and Olson, 2004), suggesting that magnetic diffusion is negligible with respect to advection of magnetic field by core flow (Roberts and Scott, 1965). However, it is possible (even probable) that a very large part of core flow does not modify the dipole moment. Such flow types include (1) zonal flow - does not change the latitude of magnetic flux; (2) flow along B_r-contours - does not advect magnetic field; (3) self-cancellation effects - flow structures that partially increase and partially decrease the dipole moment, for example a vortex interacting with a purely dipolar axisymmetric magnetic field. Zonal flow and field-aligned flow are dominant flow features in the core (Olson et al., 1999). Self-cancellation effects are evident in the balanced maps of the contribution to total changes in the dipole moment (Figs. 6.3b and 6.7). I therefore argue that the secular variation is mostly advective-driven, but dipole moment changes may be driven equally by advection and diffusion.

To address the question of whether a core flow model obtained by a frozen-flux inversion method can be used to estimate a diffusive contribution to dipole moment change, consider a pure axisymmetric dipolar magnetic field of magnitude B_0

$$B_r(t = t_0) = B_0 \cos\theta \tag{6.36}$$

that is uniformly diffused, i.e, after Δt time,

$$B_r(t = t_0 + \Delta t) = (1 - \epsilon) B_0 \cos\theta, \tag{6.37}$$

where $\epsilon < 1$ for dipole decay and $\epsilon > 1$ for dipole increase. The secular variation in this case is

$$\frac{\partial B_r}{\partial t} = -\frac{\epsilon B_0}{\Delta t} \cos\theta \ . \tag{6.38}$$

The only flows that can mimic uniform global decrease/increase in intensity are uniform global upwelling/downwelling, but such flows are not physical because they do not conserve net divergence. I have verified in my core flow solutions that the net divergence is practically zero, within the error of grid discretization (Amit and Olson, 2005). Therefore, uniform diffusion of a dipole magnetic field cannot be represented by frozen-flux flow in my method. It is possible that local diffusion effects may contaminate frozen-flux flow locally, but magnetic secular variation consistent with global dipole diffusion cannot be adequately satisfied by a flow model. Rau et al. (2000) found in core flow inversion tests using numerical dynamos that diffusion effects are absorbed in the misfits of frozen-flux methods.

Another way to examine the validity of my approach to estimate diffusive contributions to dipole moment change by frozen-flux inverted core flow models is using inversions of synthetic magnetic secular variation from numerical dynamos. As mentioned in chapter 5, the flow solutions from these inversions can be compared with the true dynamo flows to test the validity of the inversion assumptions and method. I have calculated the contribution of meridional advection to the axial dipole moment change by the inverted flow of case 1 chapter 5. I found that the change has the correct sign and recovers 88.6% and 80.8% of the advective change in the dynamo flow, without and with tangential magnetic diffusion, respectively. This result verifies empirically that the frozen-flux inversion method can identify well the advective contribution to dipole moment change, in a case where the true

contribution is known, and both radial diffusion and meridional advection are significant.

I inferred radial diffusion in the geomagnetic analysis of the time-evolution dipole moment equations in an indirect way. The total changes were computed from geomagnetic data, tangential diffusion contributions were computed from geomagnetic data and an assumption for the core's magnetic diffusivity, tangential advection contributions were computed from the interaction of geomagnetic data and a core flow model, and radial diffusion contributions were computed from the residual of the dipole moment equations. In the analysis of axial dipole moment change in a numerical dynamo, all contributions are calculated in the same way as in the geomagnetic analysis, apart from radial diffusion which is computed directly from the knowledge of the full magnetic field vector and its radial variations.

6.4.2 Geophysical interpretation

The persistent rapid geomagnetic dipole moment decrease over the last century is dominated by meridional advection of magnetic flux by core flow just below the core-mantle boundary and radial diffusion of magnetic flux from the deeper outer core. These changes are not exclusive for reversed flux; for example, advective contributions to the dipole decrease may originate from poleward motion of reversed flux or equatorward motion of normal flux. Analysis of a time-dependent geomagnetic field model on the core-mantle boundary reveals that normal and reversed flux in the southern hemisphere had comparable contributions to the dipole decrease over the last century. In the northern hemisphere, overall changes are smaller, and normal flux is actually strengthening the dipole moment with time. I demonstrated the action of meridional advection and radial diffusion mechanisms by focusing on two local areas. The northward jet below the South Indian Ocean advects an intense normal magnetic flux patch equatorward. The reversed flux patch below south of Madagascar coincides with zonal flow; the axial dipole moment decreases there

due to expansion and intensification of reversed magnetic flux by radial diffusion. In both examples the flow features are parts of the large anticyclonic vortex in the southern hemisphere, a robust flow feature in most core flow models (Bloxham and Jackson, 1991; Hulot et al., 2002; Amit and Olson, 2005). The results of the numerical integrations for the contributions of the three mechanisms to the geomagnetic dipole moment decrease between 1895-1985 suggest that at some epochs meridional advection dominates over radial diffusion, whereas at other epochs the two mechanisms are comparable. Since 1950, meridional advection and radial diffusion had comparable contributions to the dipole decrease. The mechanism of meridional advection has limited efficiency in modifying the dipole moment (Moffatt, 1978); the recent balanced partitioning between meridional advection and radial diffusion suggests that the current decrease will continue in the near future.

Analysis of a rapid magnetic dipole moment decrease event in a numerical dynamo reinforces my findings from the geomagnetic analysis; although the secular variation is dominated by advection, the dipole moment decrease recieves comparable contributions from meridional advection and radial diffusion, whereas meridional diffusion plays a secondary role. Depending on the effective depth of the ”free stream” in numerical dynamos, radial diffusion is either larger or comparable to meridional advection in their contributions to the dipole decrease. I also observed on a longer time-scale a correlation between dipole moment changes to vacillations in flow structure. Numerical dynamos suggest that reversed zonal electric currents in the fluid shell are induced by the interaction of equatorial and polar upwellings with the axisymmetric dipole magnetic field.

The time-evolution of the geomagnetic tilt is not monotonic over the last century. Between 1900-1960, the geomagnetic tilt is nearly constant; however, between 1965-2000 the tilt drifts polewards rapidly. The equatorial dipole moment recieves its most significant local contributions from below the Indian Ocean, where positive (normal) magnetic flux is supplied by meridional advection of normal flux from higher latitudes toward the current

location of the positive equatorial dipole. Over the last century, this region has actually intensified the equatorial dipole moment. The decrease in the equatorial dipole moment originates mostly from the region below North America, where negative (normal) flux is advected polewards, away from the negative equatorial dipole. Analysis of the equatorial dipole moment changes shows that the geomagnetic tilt dynamics is governed by tangential advection and radial diffusion. The balance between the two mechanisms of equatorial dipole moment changes is quite different than the balance in the axial dipole moment analysis. Between 1895-1915, relatively small global effects of both tangential advection and radial diffusion results in nearly constant tilt. Between 1920-1965, the two mechanisms counteracted each other; tangential advection acted to increase the equatorial dipole moment, but radial diffusion denied this action. Between 1970-1985, both mechanisms have acted in unison to decrease the equatorial dipole moment, resulting in the recent poleward drift of the geomagnetic tilt.

Chapter 7

Conclusions

I introduced a new method to invert geomagnetic secular variation data for the fluid flow at the top of the liquid outer core just below the core-mantle boundary. The main concepts behind this method are:

- The tangential divergence of the flow is modeled by a superposition of a previously-used tangential geostrophy assumption and a new helical flow assumption, in which the tangential divergence is correlated with the radial vorticity.
- The helical flow assumption removes non-uniqueness from the inverse problem.
- The inversion does not rely on a priori assumptions about the scale of the flow; instead a converged numerical solution is obtained by streamfunction diffusion from the helical flow assumption.
- A numerical solution is obtained using a local finite-difference method on a grid.

I applied the inversion method to the historical geomagnetic secular variation data 1895-1985. The resulting core flow model was decomposed to time-average and time-dependent parts. Time-average core flow was interpreted as thermal wind originating from

two sources: Convection in the core assuming an homogeneous core-mantle boundary, and mantle control by heterogeneous core-mantle boundary. Time-dependent core flow was interpreted in terms of angular momentum exchange between the core and the mantle. My main conclusions are:

- Common features in most core flow snapshots include a large anticyclonic vortex below the Southern Atlantic, an anticyclonic vortex below North America, a strong westward jet below mid-latitudes of the Southern Atlantic, and intense westward polar vortices (especially below the North Pole).

- The time-average core flow includes the common flow features that appear in the individual snapshots.

- The zonal part of the time-average core flow may be explained by a thermal wind model. The non-zonal core flow and the thermal wind model consistent with the density heterogeneity at the lower mantle do not correlate well.

- Time-average westward polar vortices and eastward zonal flow at high latitudes outside the tangent cylinder are driven by the core's own dynamics.

- Equatorial asymmetry in the time-average zonal core flow, i.e. the strong westward drift in the Southern hemisphere as opposed to the weak zonal flow in the Northern hemisphere, seems to be driven by the lateral heterogeneity of the lower mantle.

- Time-dependent core flow is in agreement with the observed length of day variations.

- A torsional oscillations model fits the time-dependent core flow with dominant periods of 88 and 48 years.

I tested my inversion method using synthetic magnetic secular variation data from numerical dynamo models that are characterized by Earth-like magnetic field morphology.

The conclusions of these tests are:

- Most main flow features are well recovered, in terms of magnitude, location, and direction of circulation.
- Including tangential magnetic diffusion in the inversions improves significantly the quality of flow recovery. Effects of radial magnetic diffusion cannot be modeled and might cause severe flow artifacts.
- The magnitude of the inverted flow depends on the value of the model parameter k; data misfits are not degraded by the choice of this parameter.
- Low-pass filtered secular variation data degrade the flow recovery, suggesting that effects of data truncation might be problematic in geomagnetic secular variation inversions.
- The quality of the inversions degrades substantially for more complex dynamos characterized by a lower Ekman number.

I used the time-evolution equation for the magnetic dipole moment vector to derive time-evolution equations for the magnetic dipole moment components. These equations were then applied to study rapid changes in the geomagnetic dipole moment over the last century. My main conclusions are:

- The dominant mechanisms of dipole moment changes are tangential advection and radial diffusion, whereas tangential diffusion plays a secondary role.
- The rapid decrease in the geomagnetic dipole moment intensity is due to comparable contributions of meridional advection and radial diffusion. Similar conclusion was obtained in an event of rapid magnetic dipole moment decrease in a numerical dynamo.

- Unlike the dipole moment strength, directional changes in the dipole are not monotonic, and my analysis shows why. Between 1895-1965 tangential advection and radial diffusion counteracted each other, and the geomagnetic tilt was almost constant. Toward the end of the century tangential advection and radial diffusion have worked in unison to decrease the equatorial dipole moment, resulting in the poleward drift of the dipole.

Chapter 8

Future work

8.1 Inversions of paleomagnetic secular variation data

In this thesis, I introduced a new inversion method to image core flow from magnetic secular variation data (chapter 3). I applied this method for modern satellite-based (chapter 3) and historical observatories-based (chapter 4) data. In recent years, several studies have extended (backwards in time) and improved paleomagnetic field models (Hongre et al., 1998; Constable et al., 2000; Korte and Constable, 2003; Korte and Constable, 2005). However, no published study has inverted paleomagnetic secular variation data for paleo-core flow models.

I plan to apply my inversion method to construct models of core flow over the last several millenia. Hulot et al. (1994) performed a statistical analysis to the paleomagnetic field and resolved the dominant time-scales of the field. I plan to apply similar statistical analysis to the inverted millennial time-scale flow. More specifically, this study should address the following questions:

- Does paleomagnetic time-average core flow contain features that appear in flow snapshots over the studied period?

- Is the westward drift persistent in millenial time-scale?
- What are the typical time-scales of the flow?
- What part of millennial time-scale dipole moment changes, intensity and dipole drift, can be explained by advection, and how important is magnetic diffusion on long time-scales?

8.2 Core-mantle interaction

I examined the hypothesis that the mantle controls a portion of the core flow (chapter 4). I used lower-mantle tomography data and a thermal wind model to infer core flow, and I compared this mantle-driven flow with my geomagnetic time-average core flow. This analysis contains several crucial choices: The type of correlation between seismic velocity anomalies to lower mantle density anomalies, and the type of core-mantle coupling (thermal or chemical). I assumed a simple linear thermal core-mantle coupling. A recent study argues that this relationship is more complex, and most of the buoyancy in the lower mantle is actually chemical (Trampert et al., 2004).

I plan to examine various relationships between seismic velocity anomalies and density anomalies in the mantle, and various core-mantle coupling scenarios, to derive various core density anomalies models. These models may be used

- to construct tomographic boundary conditions for numerical dynamos, and to test mantle control on core flow in numerical dynamos.
- to calculate mantle-driven thermal wind (as in chapter 4).

In both cases, results of mantle-driven core flow models may be compared with geomagnetic time-average core flow.

The thermal wind equation developed in chapter 4 relied on the assumption that the radial shear is proportional to the flow itself (Lloyd and Gubbins, 1990; Jackson and Bloxham, 1991). I plan to examine the validity of this assumption in numerical dynamos over a wide range of control parameters. I intend to search for a scaling law for this proportionality as a function of the dynamo control parameters, and I plan to attempt to extrapolate this scaling law to Earth-like values.

8.3 Inversion test

I used synthetic magnetic secular variation data from numerical dynamos to test my core flow inversion method (chapter 5). Though the main results were encouraging, the inversions succeeded less in the recovery as more complex flows were tested.

I plan to extend this project by examining more aspects of the inversion method:

- I plan to invert for several more dynamo flows with various control parameters to examine the quality of the recovered flow (see statistical measures in chapter 5) as a function of the complexity of the flow (represented by the control parameters of the numerical dynamos).

- I plan to produce “non-diffusive” synthetic secular variation data, i.e. secular variation with diffusive contributions removed, to examine the true quality of a frozen-flux inversion method.

References

Allegre, C.J., Poirier, J.-P., Humler, E., Hofmann, A.W., 1995. The chemical composition of the Earth. Earth Planet. Sci. Lett., 134, 515-526.

Amit, H., Olson, P., 2004. Helical core flow from geomagnetic secular variation. Phys. Earth Planet. Inter., 147, 1-25, doi:10.1016/j.pepi.2004.02.006.

Amit, H., Olson, P., 2005. Time-average and time-dependent parts of core flow. Phys. Earth Planet. Inter., submitted.

Andrews, D.G., 2000. Atmospheric physics. Cambridge University Press, Cambridge, 229 pp.

Aubert, J., 2005. Steady zonal flows in spherical shell fluid dynamos. J. Fluid Mech., submitted.

Aurnou, J., Andreadis, S., Zhu, L., Olson, P., 2003. Experiments on convection in Earth's core tangent cylinder. Earth and Planet. Sci. Let., 212, 119-134.

Backus, G.E., 1958. A class of self-sustaining dissipative spherical dynamos. Ann. Phys., 4, 372-447.

Backus, G.E., 1968. Kinematics of geomagnetic secular variation in a perfectly conducting core. Phil. Trans. R. Soc. Lond., A263, 239-266.

Backus, G.E., LeMouël, J.-L., 1986. The region on the core mantle boundary where a geostrophic velocity field can be determined from frozen flux magnetic data. Geophys. J. R. Astron. Soc., 85, 617-628.

Bloxham, J., 1986. The expulsion of magnetic field from the Earth's core. Geophys. J. R. Astr. Soc., 80, 695-713.

Bloxham, J., 1989. Simple models of fluid flow at the core surface derived from geomagnetic field models. Geophys. J. Int., 99, 173-182.

Bloxham, J., 1992. The steady part of the secular variation of the Earth's magnetic field. J. Geophys. Res., 97, 19565-19579.

Bloxham, J., Gubbins, D., 1985. The secular variation of the Earth's magnetic field. Nature, 317, 777-781.

Bloxham, J., Gubbins, D., 1987. Thermal core-mantle interactions. Nature, 325, 511-513.

Bloxham, J., Gubbins, D., Jackson, A., 1989. Geomagnetic secular variation. Phil. Trans. R. Soc. Lond., A329, 415-502.

Bloxham, J., Jackson, A., 1990. Lateral temperature variations at the core-mantle boundary deduced from the magnetic field. Geophys. Res. Lett., 17, 1997-2000.

Bloxham, J., Jackson, A., 1991. Fluid flow near the surface of Earth's outer core. Rev. Geophys., 29, 97-120.

Bloxham, J., Jackson, A., 1992. Time-dependent mapping of the magnetic field at the core-mantle boundary. J. Geophys. Res., 97, 19565-19579.

Bloxham, J., Zatman, S., Dumberry, M., 2002. The origin of geomagnetic jerks. Nature, 420, 65-68.

Bondi, H., Gold, T., 1950. On the generation of magnetism by fluid motion. Mon. Roy. Astr. Soc., 110, 607-611.

Braginsky, S.I., 1970. Torsional magnetohydrodynamic vibrations in the Earth's core and variations in length of day. Geomag. Aeron., Engl. Transl., 10, 1-8.

Braginsky, S.I., 1997. On a realistic geodynamo model. J. Geomag. Geoelectr., 49, 1035-1048.

Bullard, E.C., Freedman, C., Gellman, H., Nixon, J., 1950. The westward drift of the Earth's magnetic field. Phil. Trans. Roy. Soc., London A243, 67-92.

Bullard, E.C., Gellman, H., 1954. Homogeneous dynamos and terrestrial magnetism. Phil. Trans. R. Soc. Lond., A 247, 213-278.

Busse, F.H., 1975. A model of the geodynamo. Geophys. J. R. Astron. Soc., 42, 437-459.

Chandrasekhar, S., 1961. Hydrodynamic and hydromagnetic stability. Dover Publications, New York, 652 pp.

Christensen, U.R., Aubert, J., Cardin, P., Dormy, E., Gibbons, S., Glatzmaier, G.A., Grote, E., Honkura, Y., Jones, C., Kono, M., Matsushima, M., Sakuraba, A., Takahashi, F., Tilgner, A., Wicht, J., Zhang, K., 2001. A numerical dynamo benchmark. Phys. Earth Planet. Inter., 128, 25-34.

Christensen, U. R., Olson P., 2003. Secular variation in numerical geodynamo models with lateral variations of boundary heat flow. Phys. Earth Planet. Inter., 138, 39-54.

Christensen, U., Olson, P., Glatzmaier, G.A., 1998. A dynamo model interpretation of geomagnetic field structures. Geophys. Res. Lett., 25, 1565-1568.

Christensen, U., Olson, P., Glatzmaier, G.A., 1999. Numerical modeling of the geodynamo: A systematic parameter study. Geophys. J. Int., 138, 393-409.

Christensen, U. R., Tilgner, A., 2004. Power requirement of the geodynamo from ohmic losses in numerical and laboratory dynamos. Nature, 429, 169-171, doi: 10.1038/nature02508.

Chulliat, A., Hulot, G., 2000. Local computation of the geostrophic pressure at the top of the core. Phys. Earth Planet. Inter., 59, 259-287.

Constable, C.G., Johnson, C.L., Lund, S.P., 2000. Global geomagnetic field models for the past 3000 years: transient or permanent flux lobes? Phil. Trans. R. Soc. Lond. A., 358, 991-1008.

Cowling, T.G., 1934. The magnetic field of sunspots. Mon. Not. R. Astron. Soc., 94, 39-48.

Cushman-Roisin, B., 1994. Introduction to geophysical fluid dynamics. Prentice Hall, Englewood Cliffs, 320 pp.

Davidson, P.A., 2001. An Introduction to Magnetohydrodynamics. Cambridge University Press, Cambridge, 431 pp.

Davis, R.G., Whaler, K.A., 1996. Determination of a steady velocity in a rotating frame of reference at the surface of the Earth's core. Geophys. J. Int., 126, 92-100.

Dziewonski, A.M., Anderson, D.L., 1981. Preliminary reference Earth model. Phys. Earth Planet. Inter., 25, 297-356.

Elsasser, W.M., 1946. Induction Effects in Terrestrial Magnetism. Phys. Rev., 69, 106-116.

Eubanks, T.M., Steppe, J.A., Dickey, J.O., Callahan, P.S., 1985. A spectral analysis of the Earth's angular momentum budget. J. Geophys. Res., 90, 5385-5404.

Forte, A.M., Mitrovica, J. X., 2001. Deep-mantle high-viscosity flow and thermochemical structure inferred from seismic and geodynamic data. Nature, 410, 1049-1056.

Gire, C., LeMouël, J.-L., 1990. Tangentially geostrophic flow at the core-mantle boundary compatible with the observed geomagnetic secular variation: The large-scale component of the flow. Phys. Earth Planet. Inter., 59, 259-287.

Gire, C., LeMouël, J.-L., Madden, T., 1984. The recent westward drift rate of the geomagnetic field and the body drift of external layers of the core. Annls. Geophys., 2, 37-45.

Gire, C., LeMouël, J.-L., Madden, T., 1986. Motions of the core surface derived by SV data. Geophys. J. R. Astron. Soc., 84, 1-29.

Gire, C., LeMouël, J.-L., 1990. Tangentially geostrophic flow at the core-mantle boundary compatible with the observed geomagnetic secular variation: The large-scale component of the flow. Phys. Earth Planet. Inter., 59, 259-287.

Glatzmaier, G.A., 2002. Geodynamo simulations - How realistic are they? Ann. Rev. Earth Planet. Sci., 30, 237-257.

Glatzmaier, G., Coe, R., Hongre, L. and Roberts, P., 1999. The role of the earth's mantle in controlling the frequency of geomagnetic reversals. Nature, 401, 885-890.

Glatzmaier, G.A., Roberts, P.H., 1995. A three-dimensional convective dynamo solution with rotating and finitely conducting inner core and mantle. Phys. Earth Planet. Inter., 91, 63-75.

Griffiths, D.J., 1999. Introduction to electrodynamics. Prentice Hall, New Jersey, 576 pp.

Gubbins, D., 1982. Finding core motions from magnetic observations. Phylos. Trans. R. Soc. London, Ser. A, 306, 249-256.

Gubbins, D., 1987. Mechanisms for geomagnetic polarity reversals. Nature, 326, 167-169.

Gubbins, D., 1996. A formlism for the inversion of geomagnetic data for core motions with diffusion. Phys. Earth Planet. Inter., 98, 193-206.

Gubbins, D., Richards, M., 1986. Coupling of the core dynamo and mantle: thermal or topographic? Geophys. Res. Lett., 13, 1521-1524.

Hide, R., 1967. Motions of the earth's core and mantle and variations of the main geomagnetic field. Science, 157, 55-56.

Hide, R., Boggs, D.H., Dickey, J.O., 2000. Angular momentum fluctuations within the Earth's liquid core and torsional oscillations of the core-mantle system. Geophys. J. Int., 143 777-786.

Hide, R., Roberts, P.H., 1961. The origin of the main geomagnetic field. Physics and Chemistry of the Earth, 4, 25-29. Pergamon Press, London.

Holme, R., 1998. Electromagnetic core-mantle coupling-I. Explaining decadal changes in the length of day. Geophys. J. Int., 132, 167-180.

Holme, R., Whaler, K.A., 2001. Steady core flow in an azimuthally drifting reference frame. Geophys. J. Int., 145, 560-569.

Holton, J.R., 1992. An introduction to dynamic meteorology. Academic Press, San Diego, US, 511 pp.

Hongre, L., Hulot, G., Khokhlov, A., 1998. An analysis of the geomagnetic field over the past 2000 years. Phys. Earth Planet. Inter., 106, 311-335.

Hulot, G., Chulliat, A., 2003. On the possibility of quantifying diffusion and horizontal Lorentz forces at the Earth's core surface. Phys. Earth Planet. Inter., 135, 47-54.

Hulot, G., Eymin, C., Langlais, B., Mandea, M., Olsen, N., 2002. Small-scale structure of the geodynamo inferred from Oersted and Magsat satellite data. Nature, 416, 620-623.

Hulot, G., LeMouël, J.-L., 1994. A statistical approach to the Earth's main magnetic field. Phys. Earth Planet. Inter., 82, 167-183.

Hulot, G., LeMouël, J.-L., Wahr, J., 1991. Taking into account truncation problems and geomagnetic model accuracy in assessing computed flows at the core-mantle boundary. Geophys. J. Int., 108, 224-246.

Jackson, A., 1997. Time-dependency of tangentially geostrophic core surface motions. Phys. Earth Planet. Inter., 103, 293-311.

Jackson, A., 2003. Intense equatorial flux spots on the surface of the Earth's core. Nature, 424, 760-763.

Jackson, A., Bloxham, J., 1991. Mapping the fluid flow and shear near the core surface using the radial and horizontal components of the magnetic field. Geophys. J. Int., 105, 199-212.

Jackson, A., Bloxham, J., Gubbins, D., 1993. Time-dependent flow at the core surface and conservation of angular momentum in the coupled core-mantle system. In: LeMouël, J.-L., Smylie, D.E., Herring, T. (Eds.), Dynamics of Earth's deep interior and Earth rotation, Geophysical Monograph 72 IUGG, Vol. 12. pp. 97-107.

Jault, D., Gire, C., LeMouël, J.-L., 1988. Westward drift, core motions and exchanges of angular momentum between core and mantle. Nature, 333, 353-356.

Jault, D., Hulot, G., LeMouël, J.-L., 1996. Mechanical core-mantle coupling and dynamo modeling. Phys. Earth Planet. Inter., 98, 187-191.

Jault, D., LeMouël, J.-L., 1989. The topographic torque associated with a tangentially geostrophic motion at the core surface and inferences on the flow inside the core. Geophys. Astrophys. Fluid Dynam., 48, 273-296.

Jault, D., LeMouël, J.-L., 1991. Exchange of angular momentum between the core and the mantle. J. Geomag. Geoelectr., 43, 111-129.

Kono, M., Roberts, P.H., 2002. Recent geodynamo simulations and observations of the geomagnetic field. Reviews of geophysics, 40, 4, 1013, doi:10.1029/2000RG000102.

Korte, M., Constable, C.G., 2003. Continuus global geomagentic field models for the past 3000 years. Phys. Earth Planet. Inter., 140, 73-89.

Korte, M., Constable, C.G., 2005. Continuus global geomagentic field models for the past 7 millenia: 2. CALS7K, Geochem. Geophys. Geosyst., 6, Q02H16, doi:10.1029/2004GC000801.

Kundu, P.K., 1990. Fluid mechanics. Academic press, San Diego, 638 pp.

Kutzner, C., Christensen, U., 2000. Effects of driving mechanisms in geodynamo models. Geophys. Res. Lett., 27, 29-32.

Langel, R.A., Estes, R.H., Mead, G.D., Fabiano, E.B., Lancaster, E.R., 1980. Initial geomagnetic field model from Masat vector data. Geophys. Res. Lett., 7, 793-796.

Larmor, J., 1919. How could a rotating body such as the Sun become a magnet? Rep. Brit. Assoc. Adv. Sci., 159-160.

LeMouël, J.-L., 1984. Outer core geostrophic flow and secular variation of Earth's magnetic field. Nature, 311, 734-735.

Li, X., Romanowicz, B., 1996. Global Mantle Shear-Velocity Model Developed Using Nonlinear Asymptotic Coupling Theory. J. Geophys. Res., 101, B10, 22,245-22,272.

Lilly, D.K., 1986. The structure, energetics and propagation of rotating convective storms. Part 2: helicity and storm stabilization. J. Atmos. Sci., 43, 126-140.

Lloyd, D., Gubbins, D., 1990. Toroidal fluid motion at the top of Earth's core. Geophys. J. Int., 93, 521-526.

Loper D.E., 1978. The gravitationally powered dynamo. Geophys. J. R. Astr. Soc., 54, 389-404.

Loper D.E., Lay, T., 1995. The Core-Mantle Boundary Region. J. Geophys. Res., 100, 6397-6420.

Masters, G., Johnson, S., Laske, G., Bolton H., 1996. A shear-velocity model of the mantle. Phil. Trans. R. Soc. Lond., A 354, 1385-1411.

Merrill, R.T., McElhinny, M.W., McFadden, P.L., 1998. The magnetic field of the Earth. Academic Press, San Diego, California, 523 pp.

Moffatt, H.K., 1978. Magnetic field generation in electrically conducting fluids. Cambridge University Press, Cambridge, 343 pp.

Munk, W.H., Macdonald, G.J.F., 1960. The rotation of the Earth. Cambridge University Press, Cambridge, UK, 323 pp.

Olsen, N., Holme, R., Hulot, G., Sabaka, T., Neubert, T., Toeffner-Clausen, L., Primdahl, F., Joergensen, J., Leger, J.-M., Barraclough, D., Bloxham, J., Cain, J., Constable, C., Golovkov, V., Jackson, A., Kotze, P., Langlais, B., Macmillan, S., Mandea, M., Merayo, J., Newitt, L., Purucker, M., Risbo, T., Stampe, M., Thomson, A., Voorhies, C., 2000. Oersted Initial Field Model. Geophys. Res. Lett., 27, 3607-3610.

Olson, P., Amit, H., 2005. Changes in Earth's dipole. Naturwissenschaften, submitted.

Olson, P., Aurnou, J., 1999. A polar vortex in the Earth's core. Nature, 402, 170-173.

Olson, P., Christensen, U.R., 2002. The time averaged magnetic field in numerical dynamos with nonuniform boundary heat flow, Geophys. J. Int., 151, 809-823.

Olson, P., Christensen, U., Glatzmaier, G.A., 1999. Numerical modeling of the geodynamo: mechanisms of field generation and equilibration. J. Geophys. Res., 104, 10383-10404.

Olson, P., Sumita, I., Aurnou, J., 2002. Diffusive magnetic images of upwelling patterns in the core. J. Geophys. Res., 107, doi:10.1029/2001jb000384.

Pais, A., Hulot, G., 2000. Length of day decade variations, torsional oscillations and inner core superrotation: evidence from recovered core surface zonal flows. Phys. Earth Planet. Inter., 118, 291-316.

Pais, A., Oliveira, O., Nogueira, F., 2004. Nonuniqueness of inverted CMB flows and deviations from tangential geostrophy. J. Geophys. Res., 109, doi:10.1029/2004JB003012.

Poirier, J.-P., 2000. Introduction to the physics of the Earth's interior. Cambridge University Press, Cambridge, 312 pp.

Protter, M.H., Weinberger, H.F., 1967. Maximum principles in differential equations. Prentice Hall, Englewood Cliffs, 261 pp.

Rau, S., Christensen, U., Jackson, A., Wicht, J., 2000. Core flow inversion tested with numerical dynamo models. Geophys. J. Int., 141, 485-497.

Roberts, G.O., 1972. Dynamo action of fluid motions with two-dimensional periodicity. Phil. Trans. R. Soc. Lond., 271, 411-454.

Roberts, P.H., Glatzmaier, G.A., 2000. Geodynamo theory and simulations. Rev. Mod. Phys., 72, 1081-1123.

Roberts, P.H., Scott, S., 1965. On analysis of the secular variation. J. Geomagn. Geoelectr., 17, 137-151.

Salmon, R., 1998. Geophysical fluid dynamics. Oxford University Press, New York, 378 pp.

Sardeshmukh, P.D., Hoskins, B.J., 1987. On the derivation of the divergent flow from the rotational flow: the χ problem. Q. J. R. Meteorol. Soc., 113, 339-360.

Sardeshmukh, P.D., Hoskins, B.J., 1988. The generation of global rotational flow by steady idealized tropical divergence. J. Atmos. Sci., 45, 1228-1251.

Schubert, G., Turcotte, D., Olson, P., 2001. Mantle Convection in the Earth and Planets. Cambridge University Press, Cambridge, UK, 940 pp.

Stacey, F., 1992. Physics of the Earth. Brookfield Press, Brisbane, Australia.

Stephenson, F.R., Morrison, L.V., 1995. Long-term fluctuation in the Earth's rotation-700 B.C. to A.D. 1990. Phil. Trans. R. Soc. Lond., A, 351, 165-202.

Sverdrup, H.U., 1947. Wind-driven currents in a baroclinic ocean, with application to the equatorial currents of the eastern Pacific. Proc. Nat. Acad. Sci. 33, 318-326.

Taylor, J.B., 1963. The magneto-hydrodynamics of a rotating fluid and the earth's dynamo problem. Proc. R. Soc., A, 274, 274-283.

Trampert, J., Deschamps, F., Resovsky, J., Yuen, D., 2004. Probabilistic Tomography Maps Chemical Heterogeneities Throughout the Lower Mantle. Science, 306, 853-856, doi: 10.1126/science.1101996.

Voorhies, C. V., 1986. Steady flows at the top of Earth's core derived from geomagnetic field models. J. Geophys. Res., 91, 12,444-12,466.

Voorhies, C. V., Backus, G.E., 1985. Steady flows at the top of the core from geomagnetic-filed models - the steady motions theorem. Geophys. Astrophys. Fluid Dyn., 32, 163-173.

Whaler, K. A., 1980. Does the whole of Earth's core convect? Nature, 287, 528-530.

Whaler, K. A., 1986. Geomagnetic evidence for fluid upwelling at the core-mantle boundary. Geophys. J. R. Astron. Soc., 86, 563-588.

Zatman, S., Bloxham, J., 1997. Torsional oscillations and the magnetic field within the Earth's core. Nature, 388, 760-763.

Zhang, K., Gubbins, D., 1992. On convection in the earth's core driven by lateral temperature variations in the lower mantle. Geophys. J. Int., 108, 247-255.